Theory of Superjunction Devices

Hyemin Kang

Department of Engineering

University of Cambridge

This dissertation is submitted for the degree of

Doctor of Philosophy

Hughes Hall 07.2019

Declaration

I hereby declare that except where specific reference is made to the work of others, the contents of this dissertation is original and have not been submitted in whole or in part for consideration for any other degree or qualification in this, or any other University. This dissertation is the result of my own work and includes nothing which is the outcome of work done in collaboration, except where specifically indicated in the text. This dissertation contains less than 65,000 words including appendices, bibliography, footnotes, tables and equations and has less than 150 figures.

Hyemin Kang

07.2019

Abstract

Theory of Superjunction Devices

Hyemin Kang

Since the first ideal specific resistance model by Fujihira in 1997 and the first commercial superjunction MOSFET by Infineon technology in 1998, the technology and the understanding of superjunction devices have been gradually progressed. Although Fujihira's ideal model was developed to estimate the specific on-state resistance at a given cell pitch as a function of the breakdown voltage, the model does not work for sub micro cell pitches because it does not consider the parasitic junction field effect transistor (JFET) presented in the superjunction. Fujihira's model assumes the limit of the minimum cell pitch, by saying that the specific resistance can be decreased indefinitely with decreasing the cell pitch.

In 2018, the first universal model for the specific on-state resistance of a superjunction MOSFET including the parasitic JFET effect was derived by H. Kang and F. Udrea. This model employs the classical JFET theory into the superjunction structure and clearly presents the true limit of the cell pitch of superjunction MOSFETs, as well as the specific resistance for different semiconductor materials. The classical JFET theory can be also applied to various superjunction structures and the detailed derivation process is described in Chapter 2. In Chapter 3, an advance device structure, three-dimensional (3-D) superjunction MOSFET, is introduced. To understand the superior performance of 3-D superjunction MOSFET, radial Poisson equation is employed. From theses mathematical calculation, it can be clearly seen that the 3-D superjunction is able to decrease the specific on-state resistance by half of the 2-D. In Chapter 4, based on the depletion process of superjunction during the switching, the inner circuit models for capacitance are provided. From the inner circuit models, typical capacitance curves with respect to the applied bias are drawn and they are expressed in terms of material parameters.

Acknowledgements

I would like to dedicate this thesis to Dr. Thomas Neyer, Prof. Florin Udrea, Sora Yoo, my laboratory colleagues and to my family. I am very lucky to have two life mentors. Thomas has guided me to finish my Ph. D. course successfully, since I was in Fairchild. When I was searching for a university for further study, his insight and advice changed my life indefinitely. Regardless of how little he knew me, he believed in my potential and provided invaluable guidance. When I was struggling with the English test to enter Cambridge, he was always supportive and patient. Whilst working together on SiC superjunction, he did not pressurise me and his advice allowed me to produce good results in my research. He has always given me enough time to think and understand what we are doing. Despite his busy schedule as a manager of On-Semiconductor, he has been approachable and able to provide critical advice on my progress. From this experience, I am highly inspired by his kind attention and philosophy toward our field and by the relationship he has with other engineers.

The second life mentor is Florin, who has shown me such a good example as a professor in academia. Despite his worldwide reputation and a unique position in power electronics, he makes much time for his students and his attitude toward his research has been always modest. He has been patient to supervise me, even though the result was not always satisfactory. Florin was very focussed right from the beginning and I realised his insight was correct after a few months. In the vortex of his busy life, he carefully reviewed every manuscript and adjusted the papers. Since my dream is to become a teacher in academia like him, I have tried to learn from him as much as possible. He has encouraged me in everything I do and been liberal with my praise. If I have the chance to be a professor in a university, as a supervisor, I will always be reminded of his teaching and philosophy.

Before I came to the UK, I was slightly worried about Sora's adaptation to a new environment. However, she was hired quickly and made many European friends. She has always been full of energy and enjoys every aspect of life. Her positive way of thinking helps immensely and has ensured much happiness. Now Sora prefers living in Cambridge more than me.

My lab colleagues are all great friends with no exception. They know how to keep a good relationship with each other which makes a good atmosphere in the lab. They are always polite and respect others. I have been inspired by my friends, received much help from them and have enjoyed talking with them about many subjects.

I will never forget any of you.

Contents

List of Figures

List of Tables

List of Symbols

q	Unit charge (C)
ρ	Charge density (cm^{-3})
n	Electron density or concentration (cm^{-3})
n_p	Electron concentration in a p-type semiconductor (cm^{-3})
n_{p0}	Initial electron concentration in a p-type semiconductor (cm^{-3})
p	Hole density or concentration (cm^{-3})
p_n	Hole concentration in an n-type semiconductor (cm^{-3})
p_{n0}	Initial hole concentration in an n-type semiconductor (cm^{-3})
Q_n	Sheet charge density of electron (cm^{-2})
N_D	n-type doping concentration (cm^{-3})
$N_{D.2D}$	n-type doping concentration in two-dimensional superjunction (cm^{-3})
$N_{D.core}$	n-type doping concentration in n-type (core) – p-type (shell) superjunction (cm^{-3})
$N_{D.shell}$	n-type doping concentration in p-type (core) – n-type (shell) superjunction (cm^{-3})
N_A	p-type doping concentration (cm^{-3})
E	Electric field (V/cm)
E_S	Electric field on a semiconductor's interface (V/cm)
E_{ox}	Electric field on an oxide's interface (V/cm)
E_M	Maximum electric field (V/cm)

E_C	Critical electric field (V/cm)
$E_{C.Si}$	Silicon's critical electric field (V/cm)
$E_{C.SiC}$	Silicon-Carbide's critical electric field (V/cm)
E_x	Lateral electric field (V/cm)
$E_{x.core}$	Lateral electric field on core (n-type) – shell (p-type) superjunction (V/cm)
$E_{x.shell}$	Lateral electric field on core (p-type) – shell (n-type) superjunction (V/cm)
E_y	Vertical electric field (V/cm)
ψ	Electrostatic potential (V)
ψ_{bi}	Built-in potential between a p-n junction (V)
ψ_p	Pinch-off potential of superjunction pillars (V)
ψ_D	Lateral potential sustained on the n-pillar of a superjunction (V)
ψ_A	Lateral potential sustained on the p-pillar of a superjunction (V)
ε	Permittivity of a material
ε_S	Permittivity of a semiconductor
ε_{ox}	Permittivity of an oxide
E_{Cm}	Conduction band minimum (eV)
E_{Vm}	Valence band maximum (eV)
$N(E), N_C$	Number of states for electrons density
N_V	Number of states for holes density
$F(E)$	Electron occupancy
E_F	Fermi energy level (eV)
E_g	Energy bandgap (eV)

T	Absolute temperature (k)
k	Boltzmann constant (eV/k)
J_n	Electron current density (A/cm^2)
J_p	Hole current density (A/cm^2)
I_D	Drain current (A)
J_T	Total current density (A/cm^2)
μ_n	Electron mobility ($cm^2/(Vs)$)
$\mu_{n.core}$	Electron mobility in n-type (core) – p-type (shell) superjunction ($cm^2/(Vs)$)
$\mu_{n.shell}$	Electron mobility in p-type (core) – n-type (shell) superjunction ($cm^2/(Vs)$)
μ_p	Hole mobility ($cm^2/(Vs)$)
v	Carrier velocity (cm/s)
D_n	Electron diffusivity or diffusion coefficient (cm^2/s)
D_p	Hole diffusivity or diffusion coefficient (cm^2/s)
L_n	Electron diffusion length (cm)
L_p	Hole diffusion length (cm)
τ_n	Electron life time (s)
τ_p	Hole life time (s)
G_n	Electron generation rate (cm^{-3}/s)
G_p	Hole generation rate (cm^{-3}/s)
U_n	Electron recombination rate (cm^{-3}/s)
U_p	Hole recombination rate (cm^{-3}/s)
σ_n	Electron conductivity of a material (S/cm)

σ_p	Hole conductivity of a material (Ωcm)
ρ_n	Electron resistivity of a material (Ωcm)
ρ_p	Hole resistivity of a material (Ωcm)
L	Length of a material or a given structure (cm)
d	Half cell pitch (or width) of a structure (cm)
Z	Depth of a structure (cm)
A	Area of a material or a given structure (cm)
t_{ox}	Oxide thickness (cm)
R_{sp}	Specific resistance (Ωcm^2)
$R_{sp.n}$	Specific resistance for electrons (Ωcm^2)
$R_{sp.p}$	Specific resistance for holes (Ωcm^2)
$R_{sp.parallel}$	Specific resistance for a conventional superjunction MOSFET (Ωcm^2)
$R_{sp.sloped}$	Specific resistance for a sloped superjunction MOSFET (Ωcm^2)
$R_{sp.2D}$	Specific resistance for a two-dimensional superjunction MOSFET (Ωcm^2)
$R_{sp.3D}$	Specific resistance for a three-dimensional superjunction MOSFET (Ωcm^2)
$R_{sp.core}$	Specific resistance for a core (n-type) – shell (p-type) superjunction MOSFET (Ωcm^2)
$R_{sp.shell}$	Specific resistance for a core (p-type) – shell (n-type) superjunction MOSFET (Ωcm^2)
α	Impact ionization coefficient
α_F	Impact ionization coefficient of Fulop
α_B	Impact ionization coefficient of Baliga
W_D , W_L	Depletion width toward n-pillar in a superjunction (cm)
W_A	Depletion width toward p-pillar in a superjunction (cm)

W_{Ds}	Depletion width toward n-pillar in a superjunction at Source side (cm)
W_{Dd}	Depletion width toward n-pillar in a superjunction at Drain side (cm)
W_V	Depletion width toward the accumulation region below the gate oxide (cm)
V_a	Applied voltage (V)
V_B	Breakdown voltage (V)
V_{DS}	Drain-to-Source voltage (V)
V_{GS}	Gate-to-Source voltage (V)
V_L	Lateral voltage sustained on a superjunction pillar (V)
V_V	Vertical voltage sustained on a superjunction pillar (V)
V_i	Lateral voltage sustained on the intrinsic region in a superjunction pillar (V)
V_{ox}	Lateral voltage sustained on the oxide region in a superjunction pillar (V)
D	Duty ratio
P_T	Total power loss during switching (W)
P_{SW}	Transient switching power loss (W)
P_{ON}	On-state power loss (W)
P_{OFF}	Off-state power loss (W)
P_{GS}	Power loss in the given gate driver (W)
C_{GS}	Gate-to-Source capacitance (F)
C_{GD}	Gate-to-Drain capacitance (F)
C_{DS}	Drain-to-Source capacitance (F)
C_{iss}	Input small signal capacitance (F)
C_{oss}	Output small signal capacitance (F)

C_{rss}	Gate-to-Drain small signal capacitance (F)
$C_{GD.sp}$	Specific Gate-to-Drain capacitance (F/cm^2)
$C_{DS.sp}$	Specific Drain-to-Source capacitance (F/cm^2)
$C_{oss.sp}$	Specific output capacitance (F/cm^2)
$C_{rss.sp}$	Specific small signal Gate-to-Drain capacitance (F/cm^2)
Q_{GD}	Amount of charge for charging Gate-to-Drain capacitance (C)
Q_{DS}	Amount of charge for charging Drain-to-Source capacitance (C)
Q_{oss}	Amount of charge for charging output capacitance (C)
$Q_{GD.sp}$	Specific amount of charge for charging Gate-to-Drain capacitance (C/cm^2)
$Q_{DS.sp}$	Specific amount of charge for charging Drain-to-Source capacitance (C/cm^2)
$Q_{\text{oss}.sp}$	Specific amount of charge for charging output capacitance (C/cm^2)
E_{DS}	Energy loss in Drain-to-Source capacitance (J)
E_{oss}	Energy loss in output capacitance (J)
$E_{DS.sp}$	Specific energy loss in Drain-to-Source capacitance (J/cm^2)
$E_{\text{oss}.sp}$	Specific energy loss in output capacitance (J/cm^2)

1. Introduction

1.1. History

The first power device goes back to the 1950's when thyristors were first developed. Thyristors do not require vacuum tubes for the operation, as they operate at high currents and high voltages, as well as at high frequencies. Bipolar junction Transistors (BJTs) are another type of bipolar power device invented during this period. The main disadvantage of these bipolar devices is the driving switching loss. The gate (or base) for the bipolar devices are sensitive to the external noise and consumes high energy. By the 1970's, Bipolar transistors evolved to over 5000 V blocking voltage in 4-inch wafers. At this time, metal oxide semiconductor field effect transistors (MOSFET) were developed for the power industries. MOSFETs are unipolar devices and as a result they can operate at higher frequencies. Also, since MOSFET's gate is insulated from the active layer by oxide layer, the switching loss on the gate is ideally zero. In 1978, a new type of varactor diode having a parallel arrangement of the n-pillar and p-pillar was introduced by Shirota and Kaneda as shown in figure 1.1 [1].

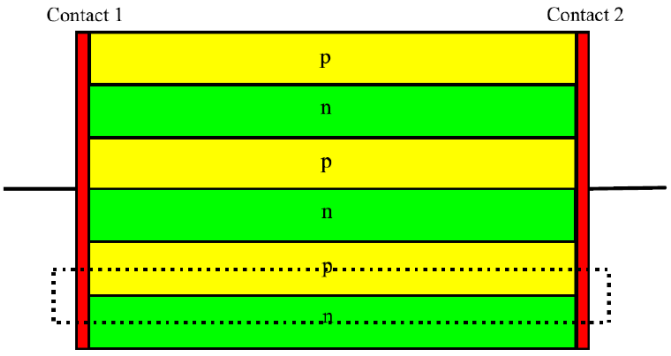

Figure 1.1 The first idea of a superjunction concept [2], [3].

The purpose of this idea was to achieve a more non-linear capacitance curve with respect to the applied reverse bias. Even though the study provided an analytic model to explain the behaviour of the parallel junction system, the concept was specifically conceived for capacitors.

A superjunction MOSFET with multiple stacks of alternative p-pillar/n-pillar stripes were first devised by Coe *et al.* [4], [5]. The gate oxide was formed by V-groove etching to connect all the n-pillars to the channel as shown in figure 1.2.

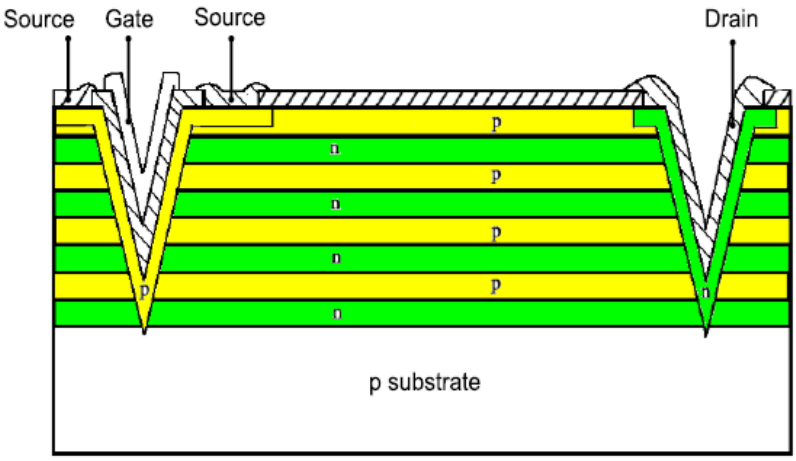

Figure 1.2 A schematic illustration of the first superjunction MOSFET [3].

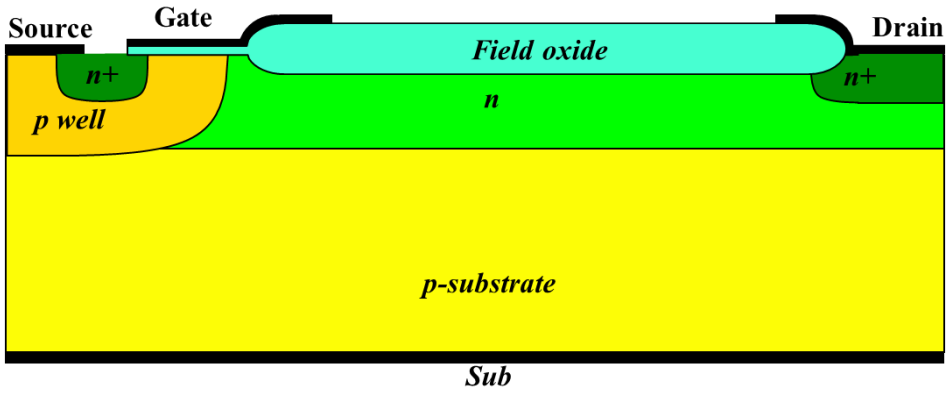

Figure 1.3 A schematic illustration of a lateral diffused MOSFET with a reduced surface field layer [3].

Another type of device is a lateral diffused metal oxide semiconductor field effect transistor with reduced surface field (RESURF) oxide layer as shown in figure 1.3 [6]. The oxide field plate drags the surface electric field to the drain side, facilitating even distribution of the electric field in the entire drift region. By inserting a p-type layer under the oxide plate, a double RESURF lateral MOSFET is realised and the concept resembles superjunction, as shown in figure 1.4 [7]. The p-type layer under the oxide field plate helps the depletion of the n-type drift region more effectively and therefore the concentration of the n-type drift region can be increased, while decreasing on-state resistance of the device.

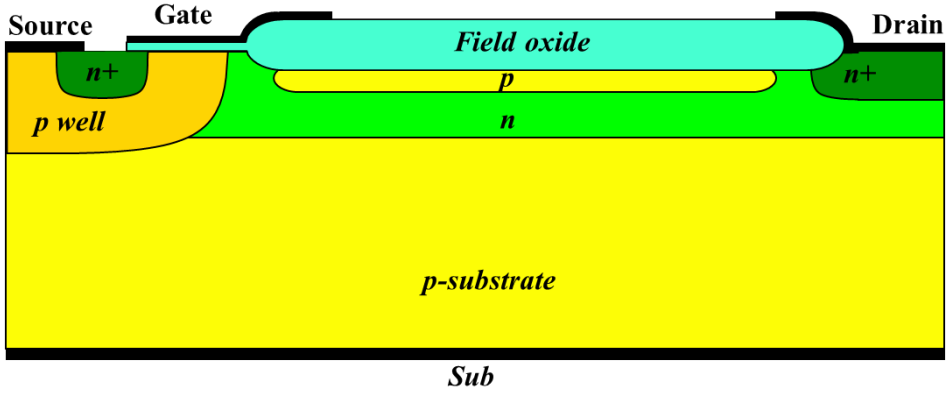

Figure 1.4 A schematic illustration of a lateral diffused MOSFET with a double reduced surface field layer [3].

In 1997, Fujihira tried to explain the superjunction system theoretically by deriving a relationship between the on-state resistance and the breakdown voltage [8]. In 1998, a

revolutionary concept, 3-D RESURF" was proposed by Udrea *et al*. [9], where multiple p-n stripe arrays are configured in the third dimension as shown in figure 1.5. The structure utilises a charge balance concept between the n-type and the p-type stripes to control the breakdown voltage [10].

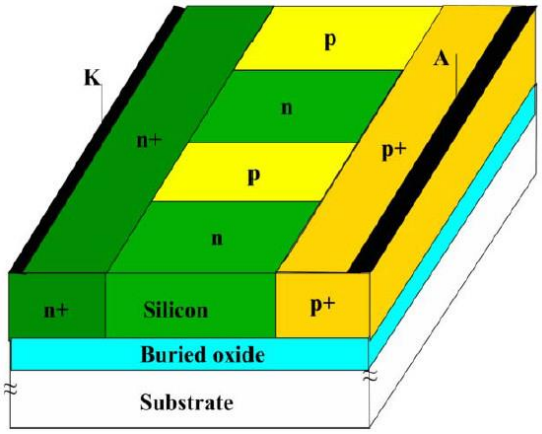

Figure 1.5 A schematic illustration of 3-D RESURF structure [3], [9].

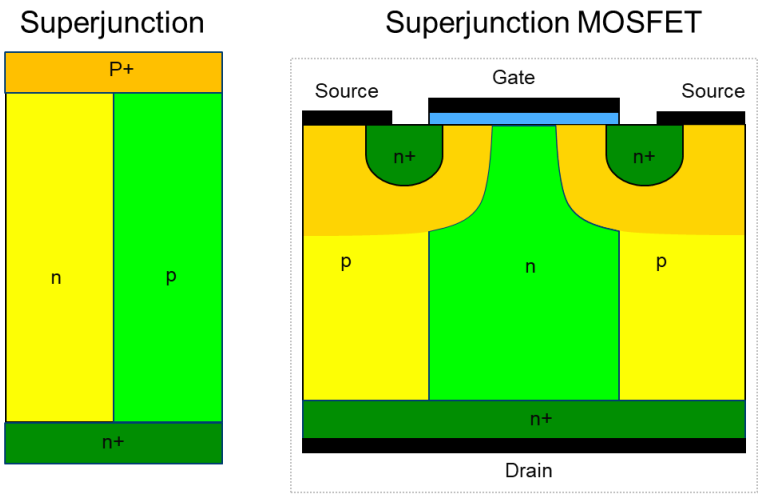

Figure 1.6 Schematic illustrations of superjunction structure and superjunction device [3].

In 1998, the first commercial product, CoolMOS^{TM}, was released by Infineon technology [11]. From the first mass production of 600 V rating superjunction power devices, industries and universities invested a huge effort to improve the performance of the device and to build the

theoretical backgrounds. For example, to understand the breakdown in a superjunction system, a complex two-dimensional Poisson equation should be solved. Napoli *et al*. provided the solution of the Poisson equation and firstly derived the electric field profiles in a superjunction system as shown in figure 1.7 [12]–[15].

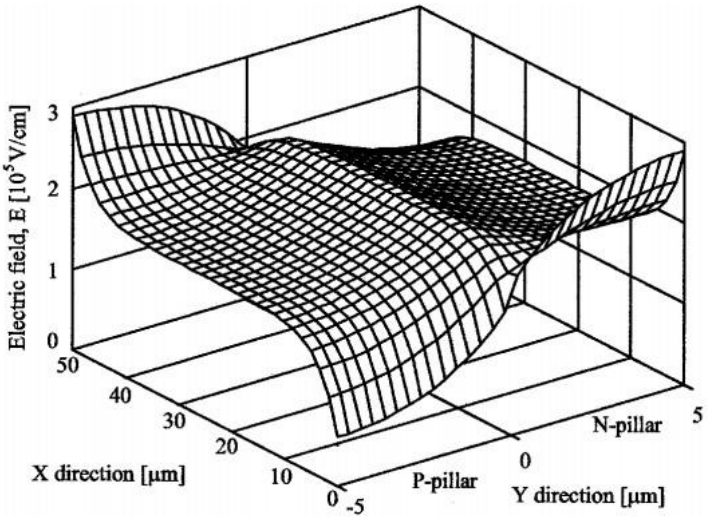

Figure 1.7 An electric field profile in a superjunction calculated from 2-D Poisson equation [13].

Saito also studied the process window of the superjunction system, with respect to the charge imbalance [16]. Disney and Dolny firstly simulated the limit of superjunction system but failed to develop an analytical model [17]. Kang and Udrea primarily derived the specific resistance of a superjunction system and provided the theoretical limit (true limit) of a superjunction devices [18], [19].

Besides these theoretical approaches for superjunction MOSFETs, superjunction insulated gate bipolar transistors (IGBTs) have been intensively investigated by Bauer and Antoniou [20]–[25] because of extremely low turn-off switching loss and high blocking capabilities. The low turn-off loss is facilitated by the deep collection of plasma, near the collector side of the drift region at a low reverse blocking voltage. In 2016, the first industrial superjunction IGBT had been reported by TRinno Technology [26]. Figure 1.8 shows a schematic illustration of a superjunction IGBT. Recently, Kang and Udrea provided an inner circuit model of a

superjunction IGBT and theoretically forecasted that the doping concentration in the pillars should be as high as possible, if one designs silicon-carbide superjunction IGBTs [27].

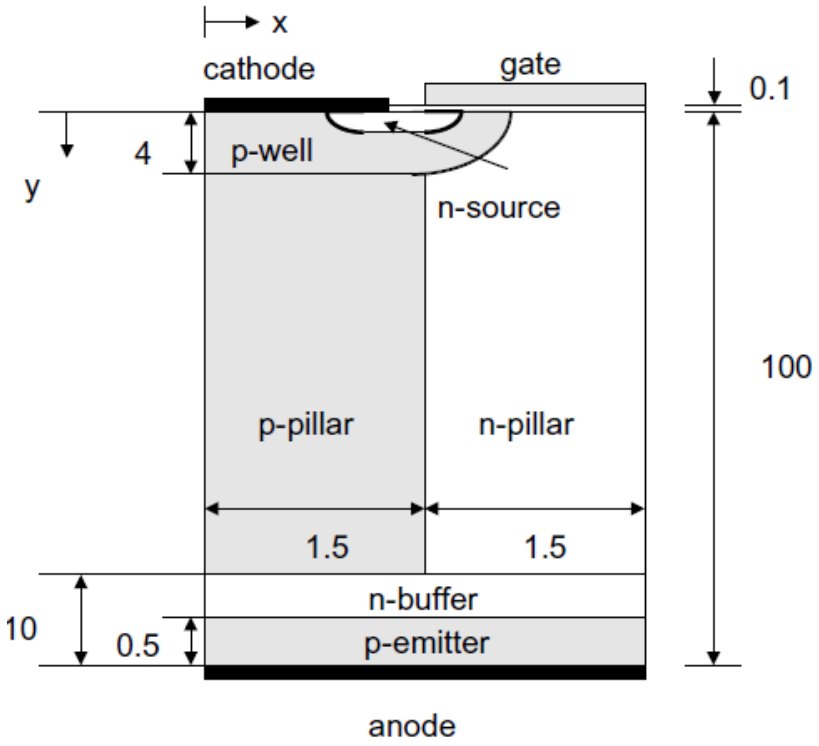

Figure 1.8 A schematic illustration of a superjunction IGBT [20].

However, as the silicon superjunction technology evolves to smaller and smaller cell pitches, the technological difficulty, such as the process window and the compensation of the doped ions, becomes prominent [28]. For this reason, silicon-carbide (SiC) device started to be studied for the next generation vertical power device because SiC can sustain 9 times higher breakdown voltage, with the help of the 9 times higher critical electric field [29], [30]. In 2011 and 2013, Cree and Rohm released 1200 V SiC MOSFET (standard type), opening a new era of power devices. In 2016, a superjunction SiC Schottky diode was experimentally demonstrated by Sheng *et al.* [31]. Even though the leakage of the device during the reverse bias was very high, due to the poor quality of the interface between the gap filling oxide and the SiC, the on-state performance showed the potential advantage of SiC device. Figure 1.9 shows the structure of the SiC Schottky diode.

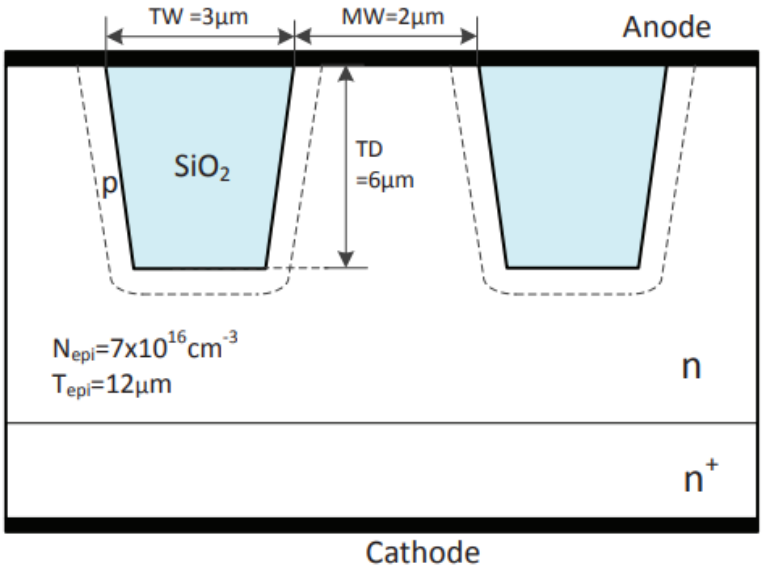

Figure 1.9 A schematic illustration of a 4H-SiC superjunction Schottky diode [31].

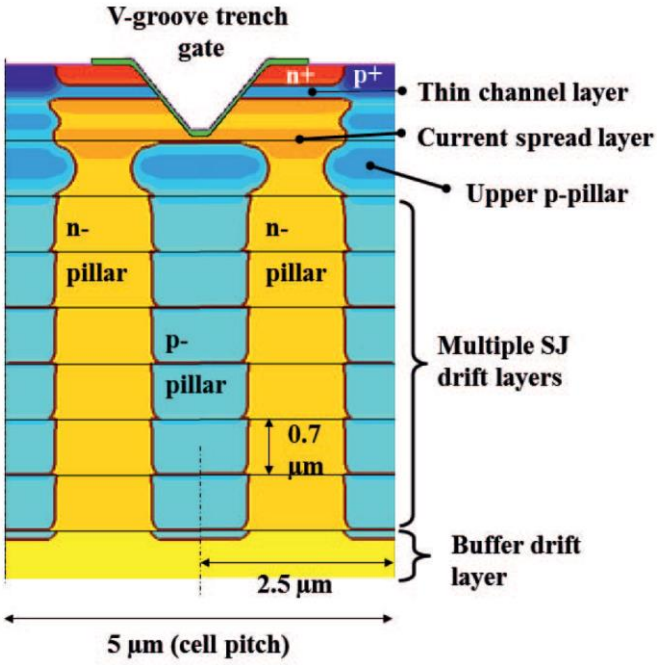

Figure 1.10 A schematic illustration of 4H-SiC Superjunction MOSFET, first demonstration [32]

After 20 years of the first demonstration of a silicon superjunction MOSFET in 1998, a SiC superjunction MOSFET featured 0.63 $m\Omega cm^2$ /1700 V with 5 μm cell pitch, which was experimentally realised by NIAIST in Japan [32], [33]. The device was fabricated by multiple

epitaxy/implantation method and the channel formed by V-groove type. The gate oxide is shielded by the heavy p-type doping below the gate oxide. Meanwhile Infineon reported 12 mohm·cm^2, 650 V Si superjunction MOSFET in 2015 [34], [35] still showing the possibility of the scaling down of a silicon superjunction structure. Figure 1.10 shows the trend of the 650 V class power devices by 2020 [36].

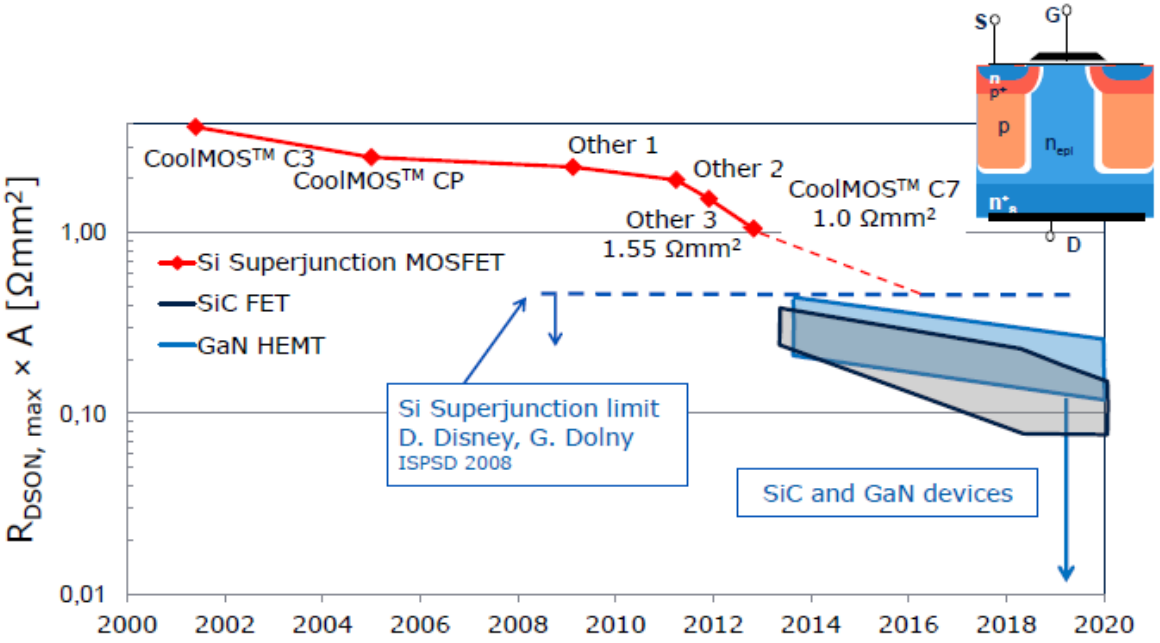

Figure 1.11 Future prospect of 650 V power MOSFET in silicon and wide bandgap devices [36].

1.2. Basic Concept of Power Devices

1.2.1. Carrier Transport and Resistance

Electrostatic Equations

The first Maxwell equation is well known as,

$$\nabla \cdot D = \rho(x, y, z), \tag{1.1}$$

where D is the electric flux density and ρ is the density of electric charges. The simplified version is known as Gauss law or Poisson equations [37], [38].

$$\frac{d^2\psi}{dx^2} = -\frac{dE}{dx} = -\frac{\rho}{\varepsilon_S} = \frac{q(n - p + N_A - N_D)}{\varepsilon_S} \tag{1.2}$$

Where ψ, E, ε_S, and q are electric potential, electric field, the permittivity of a material and unit charge. N, p, N_A, and, N_D are density of free electron, free hole, positive ion, and negative ion, respectively.

Carrier Concentration and Fermi Level

The number of free carriers, n, in an intrinsic semiconductor is the integration form of the multiplication of the total number of states for electrons density, $N(E)$, multiplied by the occupancy, $F(E)$

$$n = \int_{E_{Cm}}^{\infty} N(E) F(E) dE, \tag{1.3}$$

where E_{Cm} is the conduction band minimum. According to the Fermi-Dirac distribution, the occupancy, $F(E)$, follows the relationship

$$F(E) = \frac{1}{1 + \exp\left[(E - E_F)/kT\right]}, \tag{1.4}$$

where E_F is the Fermi level.

By applying Boltzmann statistics into equation (1.4) and solving equation (1.3), the free electron and hole density equations become:

$$n = N_C \exp\left(-\frac{E_{Cm} - E_F}{kT}\right), \text{ or } E_{Cm} - E_F = kT \ln\left(\frac{N_C}{n}\right), \tag{1.5}$$

$$p = N_V \exp\left(-\frac{E_F - E_{Vm}}{kT}\right), \text{ or } E_F - E_{Vm} = kT \ln\left(\frac{N_V}{p}\right) \tag{1.6}$$

where N_V and E_{Vm} are the total number of states density for holes and the valance band energy, respectively.

Current Density Equations

The electron and hole current densities, J_n and J_p are the sum of the diffusion current and the drift current [37]:

$$J_n = qn\mu_n E + qD_n \frac{dn}{dx}, \tag{1.7}$$

$$J_p = qp\mu_p E - qD_p \frac{dp}{dx}, \tag{1.8}$$

where, μ_n, μ_p, D_n, and D_p are the electron mobility and hole and the diffusivity of electrons and holes, respectively. The minus operator in front of the hole diffusion current means that the direction of the hole diffusion current is the opposite to the hole drift current. The total current density, J_T, is the sum of the electron and hole current densities,

$$J_T = J_n + J_p \tag{1.9}$$

Einstein Relationship

If we consider an n-type or a p-type semiconductor with non-uniform doping, the total current will be zero without an applied voltage. By rewriting equations (1.7) and (1.8),

$$J_n = qn\mu_n E + qD_n \frac{dn}{dx} = 0\,, \tag{1.10}$$

$$J_p = qp\mu_p E - qD_p \frac{dp}{dx} = 0\,, \tag{1.11}$$

and inserting equations (1.5) and (1.6) into equations (1.7) and (1.8), the diffusivity and the mobility have the following relationships,

$$D_n = \left(\frac{kT}{q}\right)\mu_n, \tag{1.12}$$

$$D_p = \left(\frac{kT}{q}\right)\mu_p \tag{1.13}$$

Equations (1.12) and (1.13) are well known as Einstein relationships, which are only valid for nondegenerate semiconductors [39]. The thermal voltage kT/q at room temperature, T= 300 K, is 0.0259 V, and the mobility of electron and hole are highly linked to that of diffusivities. i.e. if the carrier mobility is high, the diffusivity should be also high and therefore, a semiconductor having a high mobility is desirable for better conduction of the bipolar devices which require high diffusivities of electrons and holes. For this reason, Einstein relationships have been widely used to elaborate bipolar conduction. It should be noted that the diffusivity of the carriers is also linked to the carrier's life times, τ_n and τ_p, and diffusion lengths, L_n and L_P,

$$L_n = \sqrt{D_n \tau_n}\,, \tag{1.14}$$

$$L_p = \sqrt{D_p \tau_p} \tag{1.15}$$

Continuity Equations

The current density equations given by the equations (1.10) and (1.11) are only valid for steady state. Continuity equations deal with the time dependent carrier behaviour in a semiconductor when there is a low level injection, generation and recombination [37].

$$\frac{\partial n}{\partial t} = G_n - U_n + \frac{1}{q}\nabla \cdot J_n\,, \tag{1.16}$$

$$\frac{\partial p}{\partial t} = G_p - U_p + \frac{1}{q}\nabla \cdot J_p \tag{1.17}$$

Where G_n and G_P are the generation rate for electrons and holes, and U_n and U_P are the recombination rate for electrons and holes, respectively. By inserting equations (1.10) and (1.12) into (1.16) and (1.17) the equations become

$$\frac{\partial n_p}{\partial t} = G_n - \frac{n_p - n_{p0}}{\tau_n} + n_p \mu_n \frac{\partial E}{\partial x} + \mu_n E \frac{\partial n_p}{\partial x} + D_n \frac{\partial^2 n_p}{\partial x^2}\,, \tag{1.18}$$

$$\frac{\partial p_n}{\partial t} = G_n - \frac{p_n - p_{n0}}{\tau_p} + p_n \mu_p \frac{\partial E}{\partial x} - \mu_p E \frac{\partial p_n}{\partial x} + D_p \frac{\partial^2 p_n}{\partial x^2} \tag{1.19}$$

Where n_p, p_n, n_{p0}, and p_{n0} are the electron concentration in a p-type semiconductor, the hole concentration in a n-type semiconductor, initial electron concentration in a p-type semiconductor, and initial hole concentration in a n-type semiconductor, respectively

Conductivity and Resistivity

In a uniformly doped semiconductor of either n-type or p-type, the conduction is given by the drift current only. The drift current is proportional its material properties, $qn\mu_n$ and $qp\mu_p$, and the externally applied electric field, E as shown equations (1.10) and (1.11). Therefore, $qn\mu_n$ and $qp\mu_p$ become the electron and hole conductivities, σ_n and σ_p, of the material,

$$\sigma_n = qn\mu_n , \tag{1.20}$$

$$\sigma_p = qp\mu_p \tag{1.21}$$

The electron and hole resistivities, ρ_n and ρ_p, respectively, are the reciprocal form of the conductivities,

$$\rho_n = \frac{1}{qn\mu_n} , \tag{1.22}$$

$$\rho_p = \frac{1}{qp\mu_p} \tag{1.23}$$

The semiconductor resistances for n-type and p-type, R_n and R_p, respectively, are inversely proportional to the conduction area, A, and proportional to the length, L,

$$R_n = \frac{1}{qn\mu_n}\frac{L}{A} = \rho_n \frac{L}{A} , \tag{1.24}$$

$$R_p = \frac{1}{qp\mu_p}\frac{L}{A} = \rho_p \frac{L}{A} \tag{1.25}$$

Since the resistance decreases with increasing the conduction area, in power electronics, the resistance times the area is necessary to measure the performance of the device. The specific

on-state resistance, $R_{sp.n}$ and $R_{sp.p}$, respectively, are obtained by multiplying the area with the resistance,

$$R_{sp.n} = \frac{L}{qn\mu_n} = \rho_n L \,, \tag{1.26}$$

$$R_{sp.p} = \frac{L}{qp\mu_p} = \rho_p L \tag{1.27}$$

1.2.2. Critical Electric Field and Breakdown

Impact Ionization Coefficients

As free carriers are accelerated under an electric field and they repetitively collide with lattice atoms, provoking the lattice scattering. If the carriers obtain more energy under a high enough electric field, normally above that corresponding to the saturation velocity in the material, they will generate electron and hole pairs during the collision with the atoms due to the impact ionization. These generated carriers are also highly accelerated by the high electric field and this process finally causes an avalanche breakdown. The condition for avalanche breakdown depends on the impact ionization coefficients. The impact ionization coefficients of Si and 4H-SiC are given by Fulop (α_F) and Baliga's (α_B) approximations, respectively [40], [41],

$$\alpha_F\left(Si\right) = 1.8\times10^{-35}E^7 \,, \tag{1.28}$$

$$\alpha_B\left(4H-SiC\right) = 3.9\times10^{-42}E^7 \tag{1.29}$$

Poisson Equation

The value of the electric field where the avalanche breakdown takes place in a semiconductor is known as the critical electric field, E_C. The critical electric field can be calculated by using the impact ionization coefficient and simply solving one-dimensional P^+/N Poisson equation. Equation (1.30) is one-dimensional Poisson equation for the electric field profile in the uniformly doped N-type semiconductor

$$\frac{d^2V}{dx^2} = -\frac{dE}{dx} = -\frac{qN_D}{\varepsilon_S} \tag{1.30}$$

Where, V and N_D are the electrostatic potential sustained across the P^+/N junction and the doping concentration in the N-type semiconductor, respectively. By solving equation (1.13), the electric field and the potential as a function of distance can be written as

$$E(x) = -\frac{qN_D}{\varepsilon_S}(W_D - x), \tag{1.31}$$

$$V(x) = -\frac{qN_D}{\varepsilon_S}\left(W_D x - \frac{x^2}{2}\right) \tag{1.32}$$

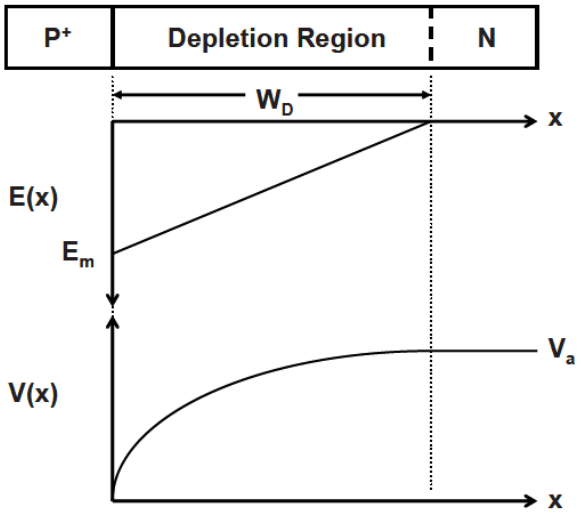

Figure 1.12 Schematic illustrations of electric field and electrostatic potential as a function of distance in P^+/N junction.

By applying the boundary condition, $V(W_D)=V_A$, the maximum electric field, $E(0)=E_M$, and the depletion width, W_D become

$$W_D = \sqrt{\frac{2\varepsilon_S V_a}{qN_D}}, \tag{1.33}$$

$$E_M = \sqrt{\frac{2qN_D V_a}{\varepsilon_S}} \tag{1.34}$$

The critical electric field is determined by the integral of impact ionization coefficient given by equations (1.28) and (1.29):

$$\int_0^{W_D} \alpha dx = 1 \tag{1.35}$$

According to SZE and Baliga the critical electric field for Si and SiC are proportional to the doping concentration, N_D, owing to the increased carrier scattering with the doped ions [39], [41],

$$E_C\left(Si\right) = 4010 N_D^{\ 1/8}, \tag{1.36}$$

$$E_C\left(4H-SiC\right) = 33000 N_D^{\ 1/8} \tag{1.37}$$

From equations (1.36) and (1.37) the breakdown voltage, V_B, for Si and SiC with respect to the doping concentration can be obtained [41]:

$$V_B\left(Si\right) = 5.34\times10^{13} N_D^{\ -3/4}, \tag{1.38}$$

$$V_B\left(4H-SiC\right) = 3.0\times10^{15} N_D^{\ -3/4} \tag{1.39}$$

1.2.3. Trade-Offs and Figures of Merit

Baliga's Static Figure of Merit

Combining the equations for on-state specific resistance, (1.26), depletion width, (1.33), and critical electric field, (1.34), the R_{sp} can be expressed in terms of material parameters [42],

$$R_{sp} = \frac{4V_B^{\ 2}}{\varepsilon_S \mu_n E_C^{\ 3}} \tag{1.40}$$

The denominator of equation (1.40) is known as Baliga's figure of merit (*BFOM*) which describes the ratio of the V_B^2 to R_{sp} [3], [43].

$$BFOM = \varepsilon_S \mu_n E_C^{\ 3} \tag{1.41}$$

It is important to note that *BFOM* is only applicable for standard (planar) type power MOSFETs and it cannot be used to advanced power devices such as, superjunction, as it will be shown later.

Fujihira's Static Figure of Merit

An ideal specific resistance of a superjunction power MOSFET with a pillar length, L, is

$$R_{sp} = \frac{2L}{q\mu_n N_D}. \tag{1.42}$$

The equation given by (1.42) is under the assumption that the width of the n-pillar and the width of the p-pillar are the same (a symmetrical super junction). According to Fujihira [3], [8], the ideal R_{sp} for a superjunction can be expressed as material parameters,

$$R_{sp} = \frac{4V_B}{\varepsilon_S \mu_n E_C^{\,2}} d, \tag{1.43}$$

where d is the cell pitch of the superjunction MOSFET. The derivation of equation (1.43) will be addressed in the next chapter. The problem of equation (1.43) is that the specific resistance of a superjunction MOSFET can be reduced indefinitely by scaling down the cell pitch. The denomination of equation (1.43) is defined as Fujihira's figure of merit, *FFOM* [8],

$$FFOM = \varepsilon_S \mu_n E_C^{\,2} \tag{1.44}$$

Total Power Loss in Switching Device

As shown in figure 1.14, in a hard switching application, the total power loss consumed by the device is the sum of the on-state, DP_{ON}, the off-state, $(1\text{-}D)P_{OFF}$, the power loss in the gate driver, P_{GS}, and the switching loss, P_{SW} [44], respectively, where D is duty ratio in a cycle:

$$P_T = DP_{ON} + (1-D)P_{OFF} + P_{GS} + P_{SW} \tag{1.45}$$

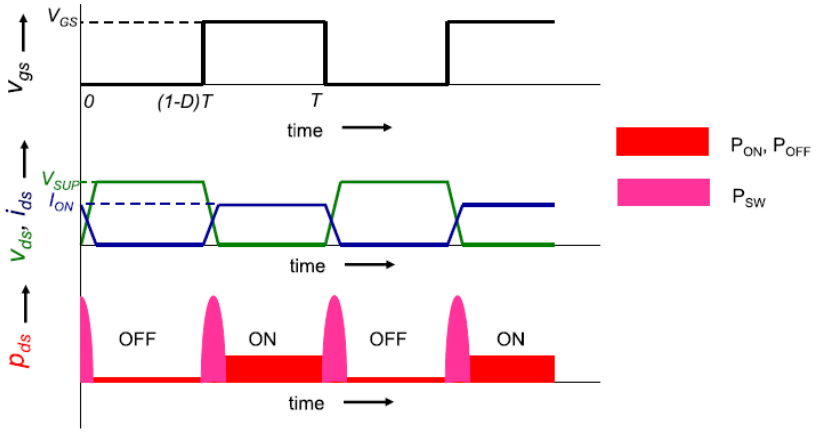

Figure 1.13 A power device's power loss in a hard switching [44].

Baliga's Dynamic Figure of Merit

In the power MOSFETs in switching applications, both the on-state resistance and the switching loss contribute to the total power loss. In 1989, Baliga proposed Baliga's high frequency figure of merit, BHFFOM [43],

$$BHFFOM = \frac{1}{R_{sp} \times C_{iss.sp}} = f_B \tag{1.46}$$

Where $C_{iss.sp}$ and f_B are input specific capacitance of the device and Baliga's frequency limit, respectively. However, *BHFFOM* defined in equation (1.46) does not consider output capacitance and the losses [44].

Kim's Dynamic Figure of Merit

To address the weakness of *BHFFOM*, Kim devised a figure of merit considering output capacitance, $C_{oss.sp}$, during the switching, *NHFFOM* [45],

$$BHFFOM = \frac{1}{R_{sp} \times C_{oss.sp}} \tag{1.47}$$

The limitation of equation (1.46) is that it does not take into account the input switching loss, P_{GS}.

Huang's Dynamic Figure of Merit

The power consumption for charging (turn-off) and discharging (turn-on) the gate to drain capacitance, C_{GD} or C_{rss}, can be indirectly regarded as the switching power consumption. Even though Huang's figure of merit, *HDFOM*, does consider other capacitance components, C_{GS} and C_{DS}, it shows a guidance how the power device can lower the power loss [46]:

$$HDFOM = \frac{1}{R_{sp} \times C_{rss.sp}} \tag{1.48}$$

However, as it is the case with Kim's figure of merit, Huang's figure of merit ignores P_{GS}. Still there has not been an all-inclusive figure of merit which describes the total power losses of a power device given by equation (1.45).

2. The 2-D Superjunction MOSFET

Summary

In the previous section, a brief history of the concepts of power MOSFETs was given. Though the evolvement in the structures, the materials, the on-state specific resistance and the breakdown voltage of power MOSFETs have been improved significantly. One of the most important turning points in power history, will be the introduction of superjunction MOSFETs. Since the first presentation of a superjunction MOSFET at IEDM 1998 [11] by Infineon Technology, the power MOSFET has broken the limit of the standard (planar) type MOSFET postulated by Baliga [42], [43]. The theoretical approach for a superjunction MOSFET was firstly suggested by Fujihira [8] and his figure of merit clearly presented the potential of superjunction devices. However, the idea was based on the ideal specific on-state resistance of a superjunction MOSFET, not considering the parasitic JFET width presented in the n-pillar. Therefore, according to his figure of merit, there is no theoretic limitation on the specific resistance of a superjunction MOSFET. i.e. the specific resistance can be decreased indefinitely as the cell pitch is scaling down. In this section, to derive the true limit of a superjunction MOSFET, a classical JFET theory will be applied to the superjunction structure and a new figure of merit for a superjunction MOSFET will be suggested. The JFET theory is applied to several other possible superjunction structures to quantitatively show the decrease in specific resistance.

2.1. Conventional Pillar Model

2.1.1. Ideal Approach

Before considering the parasitic JFET region toward n-pillar, Fujihira's ideal specific resistance and the figure of merit need to be examined first. The charge balance condition of superjunction give by figure 2.1 can be written as

$$N_D \beta d = N_A (1-\beta) d \,, \; (0 < \beta < 1). \tag{2.1.1}$$

Where N_D, N_A, and d are the doping concentration, in the n-pillar, in the p-pillar, and the half-cell pitch of the device, respectively. β is a ratio factor which determines the width of the n-pillar and the p-pillar as shown in figure 2.1.

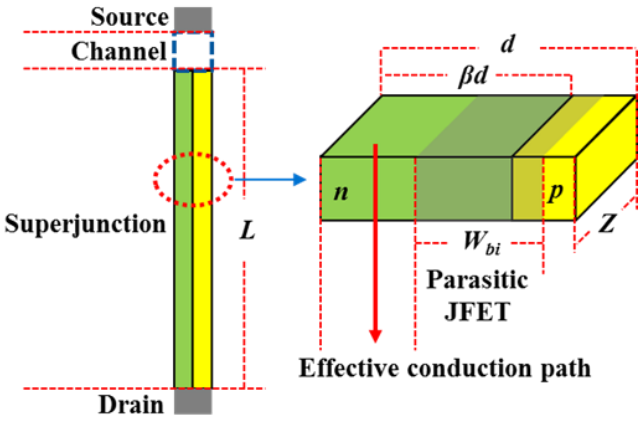

Figure 2.1 A Schematic illustration of a 2-D conventional superjunction MOSFET with the parasitic JFET depletion in the pillars [19].

Superjunction's depletion process during the off-state starts from the lateral depletion and the pillar should be fully depleted (pinch-off) before the breakdown. For this reason, the lateral field should not exceed the critical electric field, E_C:

$$E_x = \alpha E_C = \frac{qN_D}{\varepsilon_S}\beta d \ , \ (0 < \alpha < 1), \tag{2.1.2}$$

Where is α the ratio between the lateral electric field and the critical electric field. Since the square of the critical electric field is the sum of the square of the lateral electric field, E_x, and the square of the vertical electric field, E_y, the vertical electric field is

$$E_y = E_C\sqrt{1-\alpha^2} \tag{2.1.3}$$

The depletion process of a superjunction structure starts from the lateral depletion. After completing the lateral depletion, since there are no available ions in the pillars, vertical depletion occurs between the p+ region (p-body well) and the n+ region (drain). Therefore, the breakdown voltage of the superjunction device is the sum of the area under the lateral field and the vertical field. Considering the length of the pillar, L, is long enough compared to the cellpitch, the lateral component can be ignored.

$$V_B = \frac{1}{2}\alpha d E_C + E_C L\sqrt{1-\alpha^2} \approx E_C L\sqrt{1-\alpha^2} \tag{2.1.4}$$

The ideal specific resistance of the superjunction MOSFET is

$$R_{sp} = \frac{1}{qN_D\mu_n}\frac{L}{\beta dZ}dZ = \frac{L}{qN_D\mu_n}\frac{1}{\beta} \tag{2.1.5}$$

Where Z is the third dimension (depth of the pillar). By inserting equations (2.1.2) and (2.1.4) into equation (2.1.5), the specific resistance can be described in terms of the material parameters:

$$R_{sp} = \frac{V_B}{\alpha\sqrt{1-\alpha^2}\mu_n\varepsilon_S {E_C}^2}d = \frac{2V_B}{\mu_n\varepsilon_S {E_C}^2}d \ , \ \alpha = \frac{1}{\sqrt{2}} \tag{2.1.6}$$

Equation (2.1.6) has the minimum value when the α is $1/\sqrt{2}$. The calculation procedure given by equations (2.1.1) ~ (2.1.6) are firstly devised by Fujihira [8]. However, the equation given by (2.1.5) or (2.1.6) has a critical limitation. i.e. the specific resistance can be decreased indefinitely with scaling down the cell pitch, *d*. As shown in figure 2.1.1, there must be a R_{sp} limit of a superjunction because the parasitic JFET toward the n-pillar will narrow the conducting path at a very small cell pitch even if the concentrations in the pillars are high enough.

2.1.2. JFET Approach

Since Fujihira's model does not take into account the parasitic JFET effect, a simulation study had been carried out by Disney and Dolny [17] to estimate the limit of superjunctions. From their simulations, the study roughly found that the cell pitch limit of a superjunction device will be around 400 *nm* and, below the minimum cell pitch, the R_{sp} increased rapidly. To provide a quantitative solution for the true limit, the exact model for a superjunction including parasitic JFET effect must be established first. However, owing to the irregular JFET shape from source to the drain shown in figure 2.2 at a given drain bias, the exact on-state model for a superjunction MOSFET has not been established yet.

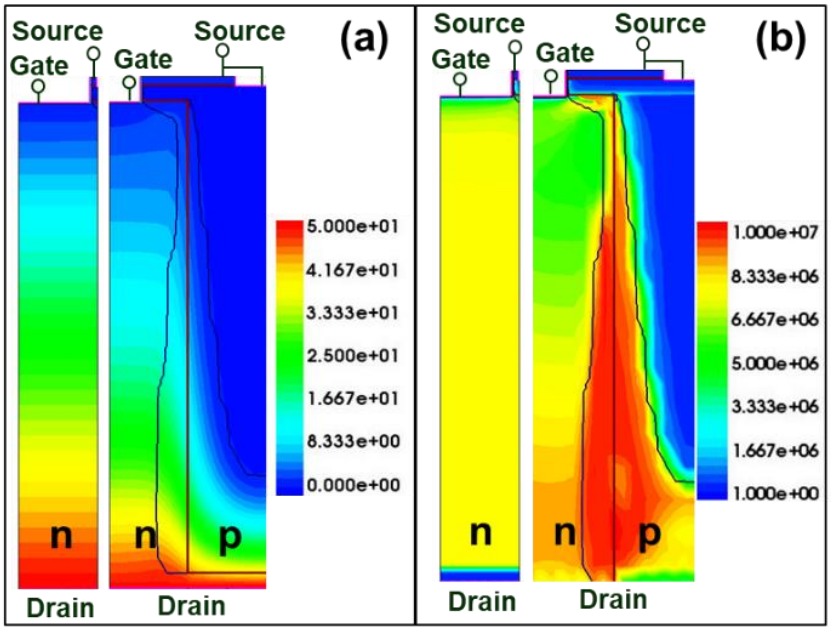

Figure 2.2 the profile of depletion width (JFET) during on-state;
(a) electrostatic potential, (b) electric field.

Previous researchers in this field have customarily called the parasitic depletion width toward the conducting path as a "JFET", but no JFET model has been derived. i.e. the superjunction structure can be viewed as a vertical JFET where the n-pillar is the channel of the JFET and the p-pillar is the gate of the JFET. The only difference between a real JFET and a superjunction

is that the p-type gate (p-pillar) is grounded to the source of the MOSFET and therefore, the JFET channel (n-pillar) is normally on as shown in figure 2.3 [18], [19].

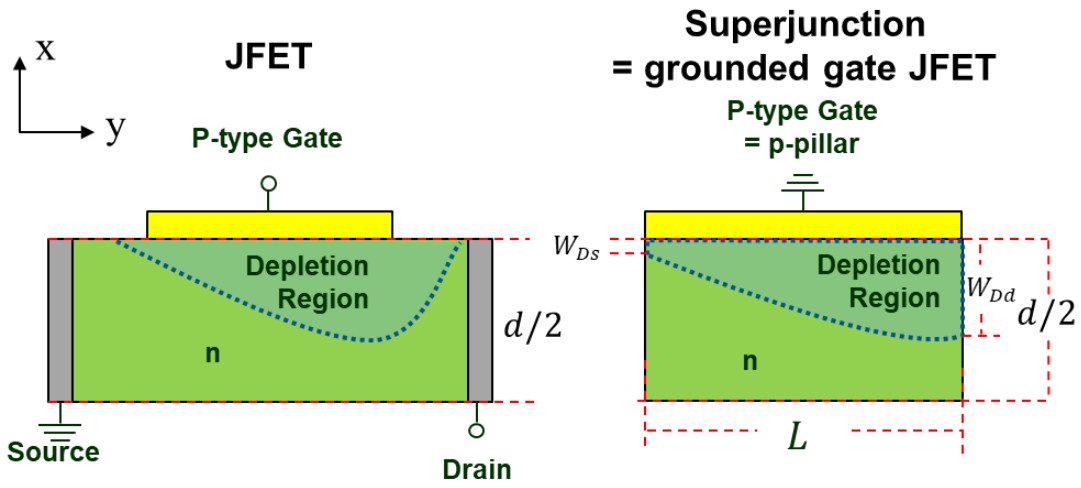

Figure 2.3 Superjunction MOSFET is a grounded gate JFET [18].

From the grounded gate JFET shown in figure 2.3, a new inner circuit configuration is also suggested. As the drift region (n-pillar) of a superjunction MOSFET has been regarded as a simple resistor, the resistor is replaced with a grounded gate JFET as shown in figure. 2.4.

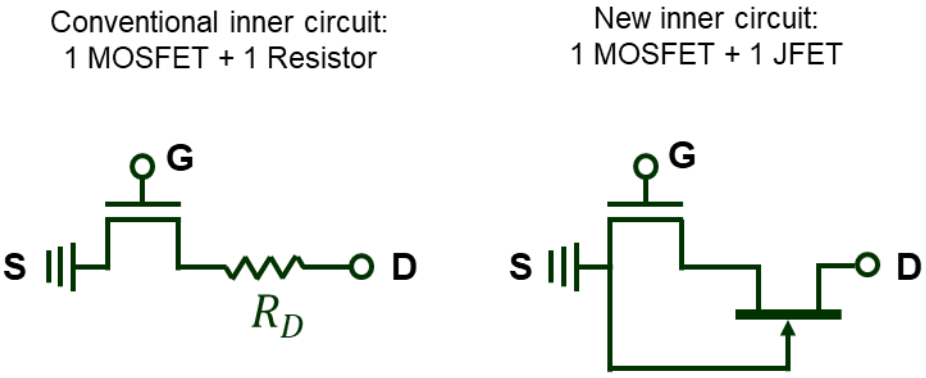

Figure 2.4 A new inner circuit model for a superjunction MOSFET [18].

The depletion width and the sheet charge density as a function of distance along the pillar need to be defined first. From the depletion width as a function of the applied bias developed from

1D Poisson equation given by (1.33), he depletion widths, $W_D(y)$, W_{Ds}, and W_{Dd} shown in figure 2.3 are as follows:

$$W_D(y) = \sqrt{\frac{2\varepsilon_S N_A \psi(y)}{qN_D(N_A + N_D)}} = \sqrt{\frac{2\varepsilon_S \beta \psi(y)}{qN_D}}, \tag{2.1.7}$$

$$W_{Ds} = \sqrt{\frac{2\varepsilon_S \beta \psi_{bi}}{qN_D}}, \tag{2.1.8}$$

$$W_{Dd} = \sqrt{\frac{2\varepsilon_S \beta (\psi_{bi} + V_{DS})}{qN_D}} \tag{2.1.9}$$

Where ψ_{bi} and $\psi(y)$ are the built-in potential between the n-pillar and the p-pillar and the potential in the n-pillar, respectively. The differential form of equation (2.1.7) is required for the integral of the total current,

$$\frac{dW_D}{d\psi} = \frac{\varepsilon_S \beta}{qN_D W_D} \tag{2.1.10}$$

The sheet charge density, $Q_n(y)$ in the n-pillar along the y-axis is written as

$$Q_n(y) = qN_D(\beta d - W_D(y)) \tag{2.1.11}$$

The velocity of electron in the n-pillar, $v(y)$, is

$$v(y) = \mu_n \frac{d\psi(y)}{dy} \tag{2.1.12}$$

The total drain current, I_D, can be obtained from the integral of the multiplication of the sheet charge density and the velocity:

$$I_D = \frac{Z}{L}\int_0^L Q_n(y)v(y)dy \tag{2.1.13}$$

By inserting equations given by (2.1.7) ~ (2.1.12) into (2.1.13), the drain current yields the following form:

$$I_D = \frac{Z\mu_n q^2 {N_D}^2}{\varepsilon_S L\beta}\int_{W_{Ds}}^{W_{Dd}} (\beta d - W_D)W_D dW_D \tag{2.1.14}$$

Solving equation (2.1.14) leads to

$$I_D = \frac{Z\mu_n q^2 {N_D}^2 \beta^2 d^3}{6\varepsilon_S L}\cdot\left(3\left(\left(\frac{W_{Dd}}{\beta d}\right)^2 - \left(\frac{W_{Ds}}{\beta d}\right)^2\right) - 2\left(\left(\frac{W_{Dd}}{\beta d}\right)^3 - \left(\frac{W_{Ds}}{\beta d}\right)^3\right)\right) \tag{2.1.15}$$

Equation (2.1.15) is a generalized superjunction's drain current relationship at a given V_{DS}. From the drain current form, the specific resistance as a function of V_{DS} can be obtained:

$$R_{sp} = \frac{V_{DS}}{I_D}\times dZ = \frac{6\varepsilon_S L}{\mu_n q^2 {N_D}^2 \beta^2 d^2}\cdot\frac{V_{DS}}{\left(3\left(\left(\frac{W_{Dd}}{\beta d}\right)^2 - \left(\frac{W_{Ds}}{\beta d}\right)^2\right) - 2\left(\left(\frac{W_{Dd}}{\beta d}\right)^3 - \left(\frac{W_{Ds}}{\beta d}\right)^3\right)\right)} \tag{2.1.16}$$

The minimum specific resistance is obtained when the applied bias is zero and by applying the well-known *L'Hospital*'s rule [47] for the second term of equation (2.1.16), the final form of the R_{sp} becomes

$$\lim_{V_{DS}\to 0}\frac{V_{DS}}{\left(3\left(\left(\frac{W_{Dd}}{\beta d}\right)^2-\left(\frac{W_{Ds}}{\beta d}\right)^2\right)-2\left(\left(\frac{W_{Dd}}{\beta d}\right)^3-\left(\frac{W_{Ds}}{\beta d}\right)^3\right)\right)}$$

$$=\lim_{V_{DS}\to 0}\frac{V_{DS}}{\left(3\left(\frac{1}{\beta^2 d^2}\frac{2\varepsilon_S\beta V_{DS}}{qN_D}\right)-2\left(\frac{1}{\beta^3 d^3}\left(\frac{2\varepsilon_S\beta\left(\psi_{bi}+V_{DS}\right)^{3/2}}{qN_D}-\frac{2\varepsilon_S\psi_{bi}^{3/2}}{qN_D}\right)\right)\right)}, \tag{2.1.17}$$

$$=\lim_{V_{DS}\to 0}\frac{1}{\left(3\left(\frac{1}{\beta^2 d^2}\frac{2\varepsilon_S\beta}{qN_D}\right)-2\left(\frac{1}{\beta^3 d^3}\frac{3\varepsilon_S\beta}{qN_D}\sqrt{\frac{2\varepsilon_S\beta\psi_{bi}}{qN_D}}\right)\right)}$$

$$=\frac{1}{6}\frac{\beta^2 d^3}{\left(\left(\frac{\varepsilon_S\beta d}{qN_D}\right)-\left(\frac{\varepsilon_S}{qN_D}W_{DS}\right)\right)}=\frac{1}{6}\frac{qN_D\beta^2 d^3}{\varepsilon_S\left(\beta d-W_{Ds}\right)}$$

$$R_{sp}=\frac{L}{q\mu_n N_D\beta}\left(\frac{\beta d}{\beta d-W_{Ds}}\right) \tag{2.1.18}$$

The difference of equation (2.1.18) from Fujihira's ideal R_{sp} is the second term which describes the increase in the R_{sp} owing to the parasitic depletion width, W_{Ds}, toward the n-pillar. In a practical device, the width of the n-pillar and the p-pillar are the same, β= 0.5:

$$R_{sp}=\frac{2L}{q\mu_n N_D}\left(\frac{d}{d-2\sqrt{\frac{\varepsilon_S\psi_{bi}}{qN_D}}}\right). \tag{2.1.19}$$

It should be noted that the JFET approach for real superjunction's drain current and specific resistance does not consider Kirk effect [48]. At a high drain voltage, the depletion width near the drain side cannot be exactly calculated by using equations (2.1.7) because the bottom region of the p-pillar is depleted, by the drain contact layer and a substantial reverse potential is formed on the p-pillar. Therefore, the potential difference between the n-pillar and the p-pillar on the drain side is less than drain voltage.

2.1.3. Figure of Merit

From equation (2.18), the superjunction's R_{sp} cannot decrease indefinitely with decreasing the cell pitch and to find the minimum cellpitch, parameters should be expressed as a function of the cell pitch. According to Baliga, the critical electric field of Si and 4H-SiC vary with the doping concentration [41]:

$$E_C(Si) = 4.0\times10^3 \cdot \left(N_D\right)^{1/8}, \tag{2.1.20}$$

$$E_C(SiC) = 3.3\times10^4 \cdot \left(N_D\right)^{1/8} \tag{2.1.21}$$

From equation (2.1.2) the doping concentration and the critical electric field have the following relationship

$$\frac{1}{\sqrt{2}} E_C = \frac{qN_D}{\varepsilon_S}\beta d \tag{2.1.22}$$

Inserting equations (2.1.20) and (2.1.21) into (2.1.22) the optimum doping concentrations at a given cell pitch become

$$N_D(Si) = \frac{1}{\sqrt{2}}\frac{\varepsilon_{Si}E_{C.Si}}{q\beta d} = 5.30\times10^{11} \cdot \left(\beta d\right)^{-8/7}, \tag{2.1.23}$$

$$N_D(SiC) = \frac{1}{\sqrt{2}}\frac{\varepsilon_{SiC}E_{C.SiC}}{q\beta d} = 4.80\times10^{12} \cdot \left(\beta d\right)^{-8/7} \tag{2.1.24}$$

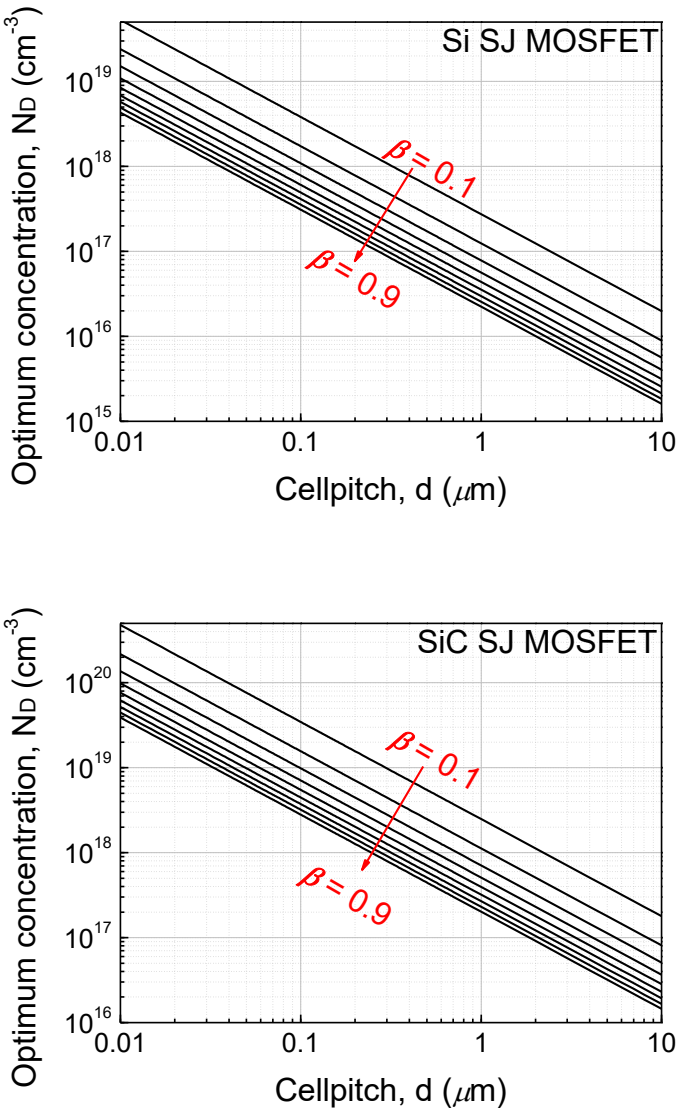

Figure 2.5 Optimum doping concentration at a given cellpitch for Si and 4H-SiC [19].

The optimum doping concentration given by equations (2.1.23) and (2.1.24) are plotted in figure 2.5. It should be noted that the higher the β, the lower the optimum concentration. However, the very small or very large values of β have technological challenges, as the width of the p-pillar or the n-pillar should be very small. In addition to this, when the pillar doping concentration exceeds 1×10^{18} cm^{-3} (degenerate doping level), the material will experience a

bandgap narrowing [49], [50] presenting a relatively lowered critical electric field. However, the following approaches ignore those physical phenomena. To establish the doping concentration dependent mobility model, Baliga's mobility models are employed [41],

$$\mu_n(Si) = \frac{5.10\times10^{18} + 92N_D^{0.91}}{3.75\times10^{15} + N_D^{0.91}}, \tag{2.1.25}$$

$$\mu_n(SiC) = \frac{4.05\times10^{13} + 20N_D^{0.61}}{3.55\times10^{10} + N_D^{0.61}} \tag{2.1.26}$$

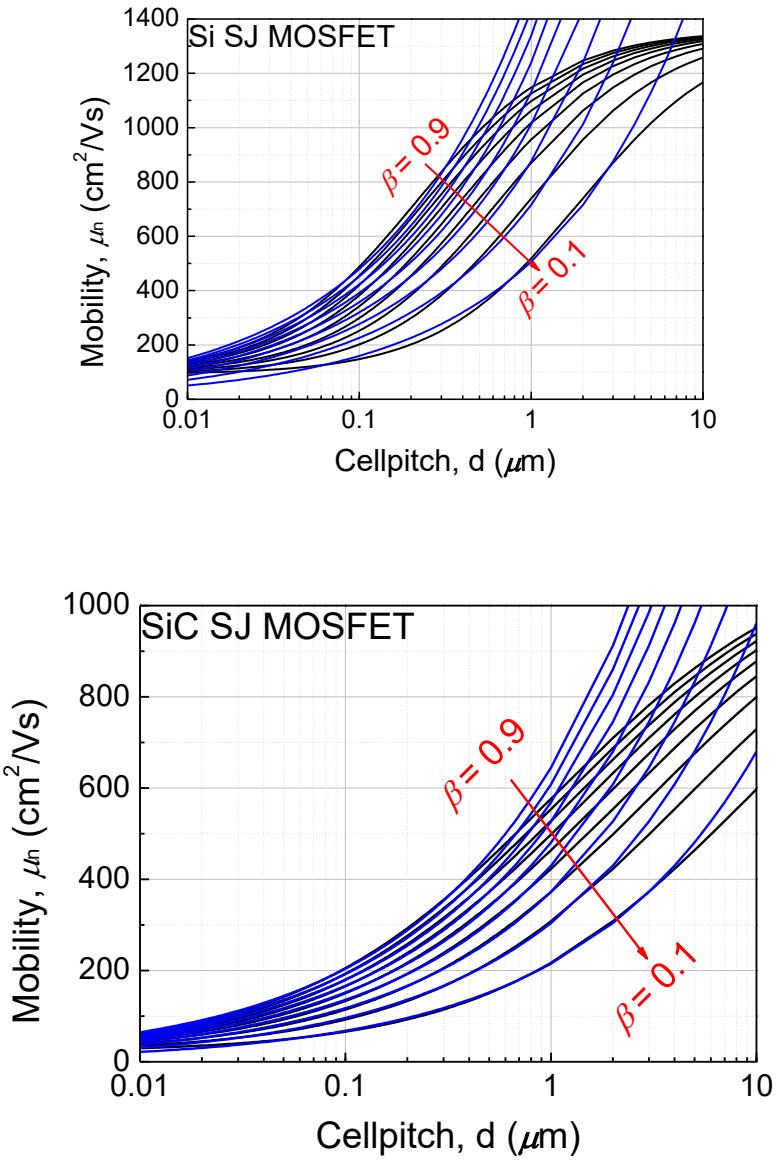

Figure 2.6 Black lines: doping concentration dependent mobility at a given cell pitch for Si and 4H-SiC, blue lines: approximated mobility curves [19].

The mobilities for Si and SiC as a function of cellpitch are shown in black lines of figure 2.6. From the blue lines in figure 2.6, the mobilities at a low cell pitch can be approximated as exponential functions:

$$\mu_n(Si) \approx 1600 \times (\beta d)^{1/2}, \tag{2.1.27}$$

$$\mu_n(SiC) \approx 680 \times (\beta d)^{1/2} \tag{2.1.28}$$

By inserting equations (2.1.23), (2.1.24), (2.1.27) and (2.1.28) into (2.1.18) the specific resistance becomes a function of the cell pitch,

$$R_{sp} = \frac{L}{q\beta} \cdot \frac{1}{\mu_n N_D} \left(\frac{\beta d}{\beta d - \sqrt{\frac{\varepsilon_S \psi_{bi}}{qN_D}}} \right) = \frac{L}{q\beta} \cdot \frac{1}{\mu_n N_D} \left(\frac{\beta d}{\beta d - \frac{1}{q}\sqrt{\frac{\varepsilon_S E_g}{N_D}}} \right) = \frac{L}{q\beta} \cdot \Psi(\beta d) \tag{2.1.29}$$

Where the built-in potential is assumed as E_g/q, E_g is the bandgap of the material, because the cell pitch having a minimum R_{sp} should have very high doping concentration. The minimum cell pitch can be obtained when the derivative of equation (2.1.29) is zero,

$$\frac{W_{Ds}}{\beta d} = \frac{3}{5} = \frac{1}{\beta d}\sqrt{\frac{\varepsilon_S}{qN_D}\frac{E_g}{q}}, \because \left(\frac{\partial \Psi(\beta d)}{\partial d} = 0 \right) \tag{2.1.30}$$

The minimum cell pitch is located when the built-in depletion width possesses 60% of the conducting path (n-pillar). By inserting equation (2.1.22) into equation (2.1.30), the minimum cell pitch is

$$d_{OP} = \frac{50\sqrt{2}}{9}\frac{E_g}{qE_C} \tag{2.1.31}$$

From equations (2.1.20), (2.1.21) and (2.1.22) the critical electric field can be expressed in terms of the cell pitch,

$$E_C(Si) = 1.26\times10^5 \cdot (\beta d)^{-1/7}, \tag{2.1.32}$$

$$E_C(Si) = 1.27\times10^6 \cdot (\beta d)^{-1/7} \tag{2.1.33}$$

By inserting the energy band gap of Si (1.12 *eV*) and 4H-SiC (3.25 *eV*) and equations (2.1.32), (2.1.33) into equation (2.1.31), the minimum cell pitch cam be also expressed in terms of β,

$$d_{OP}(Si) = \frac{50\sqrt{2}}{9}\frac{E_g}{qE_C} = 0.14\times\beta^{1/6}, \tag{2.1.34}$$

$$d_{OP}(Si) = \frac{50\sqrt{2}}{9}\frac{E_g}{qE_C} = 0.032\times\beta^{1/6} \tag{2.1.35}$$

Figures 2.7 and 2.8 show the specific resistance curves of Si and 4H-SiC superjunction MOSFETs as a function of cell pitch at a given drain voltage. It should be noted that, for a V_{DS} dependent electron mobility, a new mobility degradation model is devised, where μ_{n0} is Baliga's doping dependent mobility given by equations (2.1.25) and (2.1.26).

$$\mu_n(V_{DS}, N_D) = \frac{\mu_{n0}}{\left(1+\left(\frac{V_{DS}}{E_C L}\right)^{\frac{1}{m}}\right)^{3m}},\ m=1.73. \tag{2.1.36}$$

The mobility given by equation (2.1.36) is the averaged value in the n-pillar form source to drain.

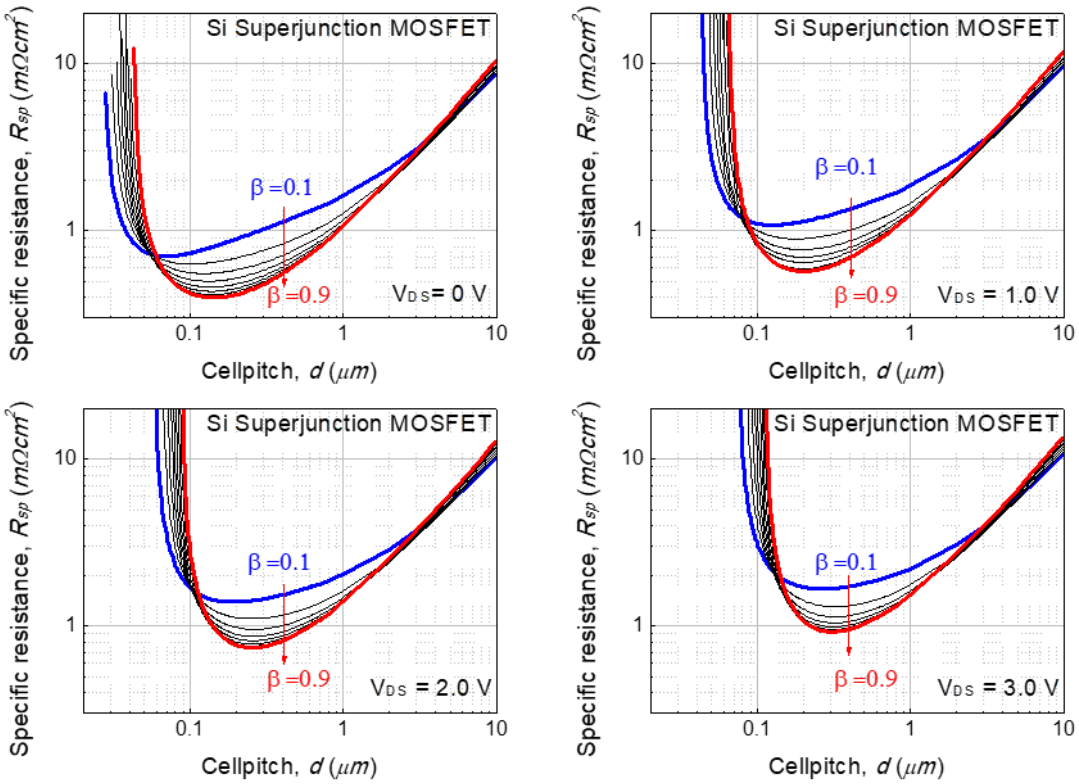

Figure 2.7 Analytic model for the specific resistance of a Si Superjunction MOSFET at a given bias. Length of pillar, L= 30 μm.

As the applied drain voltage increases, the JFET region towards the n-pillar will be wider by narrowing the conducting path. This is why the minimum cell pitch is shifted toward a larger cell pitch at a higher drain voltage. Below 1 μm cell pitch of silicon superjunction, a higher β shows a lower specific resistance and the lower specific resistance should be attributed to the higher mobility values shown in figure 2.6. In the case of 4H-SiC superjunction, owing to very high concentration values even at larger cell pitches (1 ~ 10 μm), the mobility values are in the range of rapid decrease. Therefore, a larger β superjunction has a lower specific resistance in overall cell pitch ranges. By inserting the minimum cell pitch given by (2.1.31) into (2.1.18) the R_{sp} in a superjunction MOSFET can be expressed in terms of material parameters,

$$R_{sp} = \frac{125\sqrt{2}}{9} \frac{E_g}{q\mu_n \varepsilon_S E_C^{\ 3}} V_B \approx 16 \frac{E_g}{q\mu_n \varepsilon_S E_C^{\ 3}} V_B \tag{2.1.37}$$

From, Hudgins' relationship [51], the square of the bandgap of the indirect semiconductor is proportional to the material's critical electric field, $E_g^{\ 2} \propto E_C$,

$$R_{sp} \propto \frac{V_B}{\mu_n \varepsilon_S E_g^{\ 5}}, \tag{2.1.38}$$

$$R_{sp} \propto \frac{V_B}{\mu_n \varepsilon_S E_c^{\ 2.5}} \tag{2.1.39}$$

Finally, a new figure of merit for a static superjunction MOSFET can be defined as

$$FOM = \mu_n \varepsilon_S E_c^{\ 2.5} \propto \varepsilon_S \beta^{1/6} \tag{2.1.40}$$

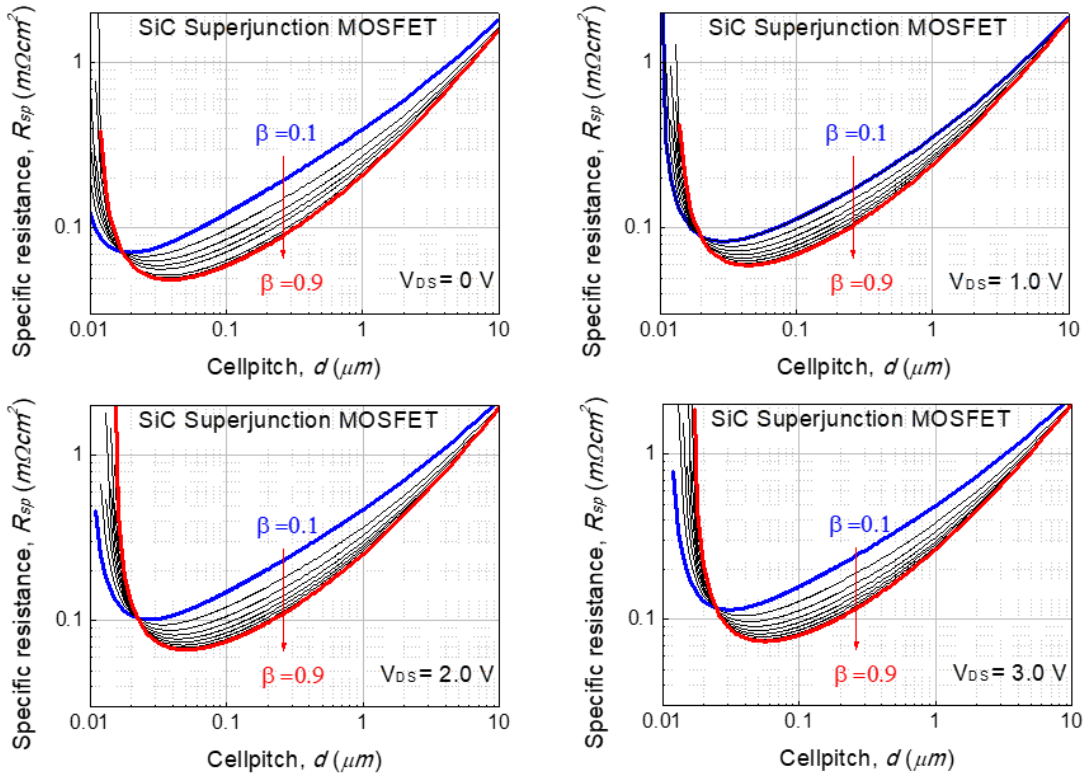

Figure 2.8 Analytic model for the specific resistance of a 4H-SiC Superjunction MOSFET at a given bias. Length of pillar, L= 30 μm.

The specific resistance as a function of breakdown voltage at the minimum cell pitch (V_{DS}= 0) is summarised in table 2.1. The R_{sp} is compared at a given cell pitch for d(Si)= 0.1 μm, and d(4H-SiC) = 0.2 μm. Breakdown voltage is linear function of the pillar length given by equation (2.1.4) and the critical electric field is the function of doping concentration given by equations (2.1.22 ~ 2.1.24).

Table 2.1 Specific resistance as a function of breakdown voltage at a given β (V_{DS} =0) for d(Si) = 0.2 μm and d(4H-SiC) = 0.1 μm.

	Silicon	4H-Silicon-Carbide
β= 0.1	$R_{sp} = 5.50\times10^{-4}\cdot V_B$	$R_{sp} = 6.29\times10^{-6}\cdot V_B$
β= 0.2	$R_{sp} = 4.69\times10^{-4}\cdot V_B$	$R_{sp} = 5.60\times10^{-6}\cdot V_B$
β= 0.3	$R_{sp} = 4.21\times10^{-4}\cdot V_B$	$R_{sp} = 5.17\times10^{-6}\cdot V_B$
β= 0.4	$R_{sp} = 3.91\times10^{-4}\cdot V_B$	$R_{sp} = 4.88\times10^{-6}\cdot V_B$
β= 0.5	$R_{sp} = 3.73\times10^{-4}\cdot V_B$	$R_{sp} = 4.65\times10^{-6}\cdot V_B$
β= 0.6	$R_{sp} = 3.60\times10^{-4}\cdot V_B$	$R_{sp} = 4.49\times10^{-6}\cdot V_B$
β= 0.7	$R_{sp} = 3.53\times10^{-4}\cdot V_B$	$R_{sp} = 4.36\times10^{-6}\cdot V_B$
β= 0.8	$R_{sp} = 3.49\times10^{-4}\cdot V_B$	$R_{sp} = 4.25\times10^{-6}\cdot V_B$
β= 0.9	$R_{sp} = 3.49\times10^{-4}\cdot V_B$	$R_{sp} = 4.16\times10^{-6}\cdot V_B$

Figure 2.9 shows the figure of merit (V_B/R_{sp}) at a given cell pitch.

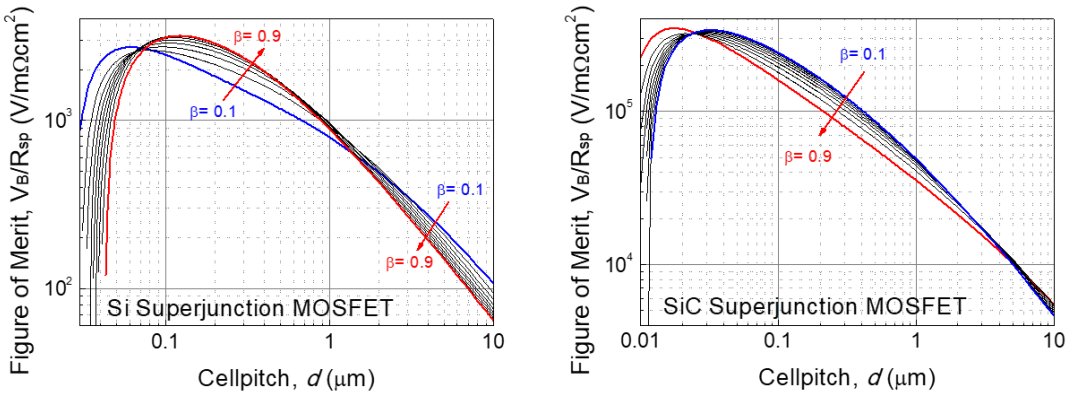

Figure 2.9 Figure of merits (V_B/R_{sp}) for Si and 4H-SiC superjunction MOSFET at a given cell pitch.

The comparisons of previously reported figure of merits are summarised in table 2.2. The true figure of merit of a superjunction is located between Baliga and Fujihira's figure of merits. In other words, Baliga underestimates the limit of the power MOSFET because he did not consider the superjunction system while Fujihira overestimates it, since he did not take into account the JFET effect in the superjunction. It is also noteworthy that Baliga overestimates the advantage of the wide bandgap materials because of E_C^3 while Fujihira underestimates it because of the presence of E_C^2.

Table 2.2 – Summary of static figure of merits for power MOSFETs with different materials [18].

Material	μ_n $\left(cm^2/V\cdot s\right)$	ε	E_C $\left(MV/cm\right)$	***Baliga*** $\mu_n\cdot\varepsilon_S\cdot E_C^3$	***Fujihira*** $\mu_n\cdot\varepsilon_S\cdot E_C^2$	***Kang* and *Udrea*** $\mu_n\cdot\varepsilon_S\cdot E_C^{2.5}$
Si	1350	11.8	0.3	1	1	1
4H-SiC	720	10	2	134	20	52
h-GaN	900	9	3.3	677	62	204
β-Ga_2O_3	300	10	8	3571	134	692
AlN	1100	8.7	11.7	35636	914	5706
Diamond	1900	5.5	5.6	4267	229	988

2.2. Sloped Pillar Model

2.2.1. Ideal Approach

As shown in figure 2.10, some commercial superjunction MOSFET devices have a geometrical slope to make an arch-shape vertical electric field [28], [52]. The sloped pillar structure can be fabricated by etching the grown n-type epitaxial layer and filling the p-type epitaxial layer. As the cellpitch of a device is scaling down, the difficulty in fabricating a sloped pillar superjunction becomes higher, owing to the precise control of the trench angle [28].

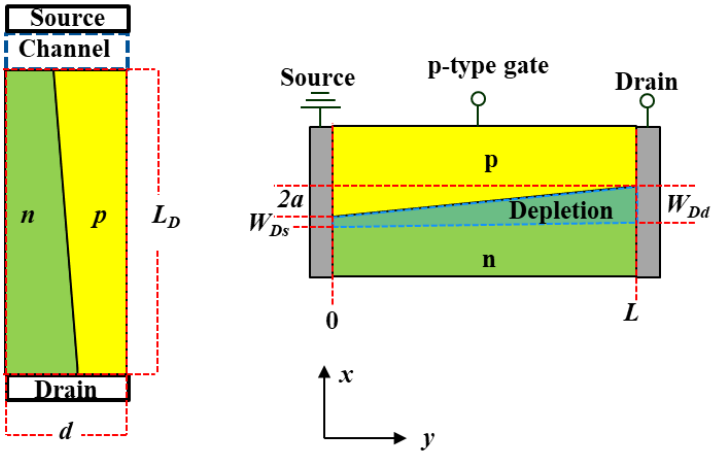

Figure 2.10 Schematic illustrations of a sloped pillar superjunction and the grounded JFET model.

In an ideal approach, the parasitic depletion width toward the n-pillar is ignored. The derivative of the resistance, *dR*, in the n-pillar as a function of "*y*" should be taken first,

$$dR = \frac{1}{qN_D\mu_n}\frac{dy}{\left(\frac{d}{2}-a\right)+\frac{2a}{L}y}\frac{1}{Z} \tag{2.2.1}$$

Where a is a slope factor described in figure 2.10. The width of the n-pillar and the p-pillar is the same in the middle of the pillar ($y = L/2$) and the doping concentration of the pillars are the same for the charge balance. By integrating equation (2.2.1), the resistance of the sloped superjunction becomes

$$R = \int_0^L dR = \frac{1}{qN_D\mu_n}\frac{L}{2aZ}\cdot\ln\left(\frac{d+2a}{d-2a}\right). \tag{2.2.2}$$

By multiplying the area, the ideal specific resistance of a sloped pillar superjunction is

$$R_{sp} = \frac{1}{qN_D\mu_n}\frac{dL}{2a}\cdot\ln\left(\frac{d+2a}{d-2a}\right) \tag{2.2.3}$$

Sending the slope factor, a, to zero, equation 2.2.3 becomes a conventional superjunction's ideal specific resistance.

$$\lim_{a\to 0}\frac{1}{qN_D\mu_n}\frac{dL}{2a}\cdot\ln\left(\frac{d+2a}{d-2a}\right) = \frac{2L}{qN_D\mu_n} \tag{2.2.4}$$

The R_{sp} ratio of the sloped superjunction to the parallel (conventional) superjunction is

$$\frac{R_{sp.sloped}}{R_{sp.parallel}} = \frac{d}{4a}\cdot\ln\left(\frac{d+2a}{d-2a}\right) \tag{2.2.5}$$

Equation (2.2.5) is plotted in figure 2.11 as a function of the slope, a/d. When a approaches $0.5d$, the conducting path on the top of the n-pillar is blocked by p-pillar with increasing the R_{sp} rapidly. Therefore, for a moderate specific resistance, the slope, a/d, should be less than 0.3.

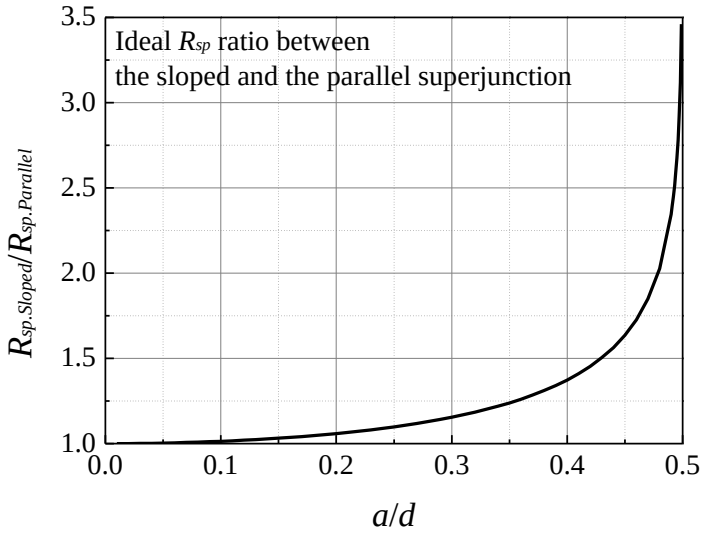

Figure 2.11 The specific resistance ratio of sloped pillar superjunction to the parallel superjunction

2.2.2. JFET Approach

As shown in figure 2.10 and section 2.1, the superjunction structure can be regarded as a p-type gate (p-pillar) JFET with n-type channel (n-pillar). The depletion widths along the distance, $W_D(y)$, the source side, W_{Ds}, and the drain side, W_{Dd}, are, respectively:

$$W_D(y) = \sqrt{\frac{\varepsilon_S \psi(y)}{qN_D}}, \tag{2.2.6}$$

$$W_{Ds} = \sqrt{\frac{\varepsilon_S \psi_{bi}}{qN_D}}, \tag{2.2.7}$$

$$W_{Dd} = \sqrt{\frac{\varepsilon_S (\psi_{bi} + V_{DS})}{qN_D}} \tag{2.2.8}$$

The sheet charge density of electrons in the n-pillar is:

$$Q_n(y) = qN_D\left(\left(\frac{d}{2} - W_D(y)\right) + \frac{2a}{L}y - a\right) \tag{2.2.9}$$

By using equations (2.2.9), (2.1.10), and (2.1.12), equation (2.1.13) should be solved

$$\frac{dW_D}{d\psi} = \frac{\varepsilon_S \beta}{qN_D W_D}, \tag{2.1.10}$$

$$v(y) = \mu_n \frac{d\psi(y)}{dy}, \tag{2.1.12}$$

$$I_D = \frac{Z}{L}\int_0^L Q_n(y)v(y)dy\,. \tag{2.1.13}$$

The integral form of equation (2.1.13) can be expanded as:

$$I_D = \frac{2qN_D Z}{\varepsilon_S L}\mu_n qN_D \int_{W_{Ds}}^{W_{Dd}}\left(\frac{d}{2} - W_D\right)W_D dW_D + \frac{Z}{L}\mu_n qN_D\int_0^L\left(\frac{2a}{L_D}y - a\right)E(y)dy \tag{2.2.10}$$

For the integral of the second term of equation (2.2.10), derivative of the resistance given by equation (2.2.1) and the relationship between the potential and the electric field should be employed,

$$d\psi = I_D dR = \frac{I_D}{qN_D\mu_n}\frac{dy}{\left(\frac{d}{2} - a\right) + \frac{2a}{L}y}\frac{1}{Z}, \tag{2.2.11}$$

$$\psi(y) = \frac{I_D}{qN_D\mu_n}\frac{L}{2aZ}\ln\left(\frac{4a}{L(d-2a)}y + 1\right), \tag{2.2.12}$$

$$\frac{d\left(y\psi\left(y\right)\right)}{dy}=\psi\left(y\right)+yE\left(y\right) \tag{2.2.13}$$

Combining equations (2.2.12). (2.2.13) and (2.2.10) the drain current as a function of V_{DS} can be obtained as:

$$I_D\left(V_{DS}\right)=q\mu_n N_D\frac{Z}{L}\left\{\frac{2aV_{DS}}{\ln\left(\frac{d+2a}{d-2a}\right)}-\frac{2}{3}\frac{qN_D}{d\varepsilon_S}\left(W_{Dd}{}^3-W_{Ds}{}^3\right)\right\}, \tag{2.2.14}$$

From equation (2.2.14), the specific resistance of a sloped pillar superjunction becomes

$$R_{sp}=\frac{1}{qN_D\mu_n}\frac{dL}{2a}\cdot\ln\left(\frac{d+2a}{d-2a}\right)\frac{V_{DS}}{V_{DS}-\frac{1}{3a}\ln\left(\frac{d+2a}{d-2a}\right)\frac{qN_D}{\varepsilon_S}\left(W_{Dd}{}^3-W_{Ds}{}^3\right)} \tag{2.2.15}$$

By sending the V_{DS} to zero, the minimum specific resistance is

$$\lim_{V_{DS}\to 0}R_{sp}=\frac{1}{qN_D\mu_n}\frac{dL}{2a}\cdot\ln\left(\frac{d+2a}{d-2a}\right)\frac{1}{1-\frac{W_{Ds}}{2a}\ln\left(\frac{d+2a}{d-2a}\right)} \tag{2.2.16}$$

Equation (2.2.16) is linked with the conventional (parallel) superjunction MOSFET given by equations (2.1.18) and (2.1.19), by sending the slope factor, a, to zero,

$$\lim_{a\to 0}\frac{1}{qN_D\mu_n}\frac{dL}{2a}\cdot\ln\left(\frac{d+2a}{d-2a}\right)\frac{1}{1-\frac{W_{Ds}}{2a}\ln\left(\frac{d+2a}{d-2a}\right)}=\frac{2L_D}{qN_D\mu_n}\left(\frac{d}{d-2W_{Ds}}\right) \tag{2.2.17}$$

The V_{DS} dependent R_{sp} of a sloped pillar superjunction given by equation (2.2.15) can be proved by comparing the analytical model with the simulation results as shown in figure 2.2.3.

The average mobility in the sloped pillar superjunction should be dependent on both the doping concentration and V_{DS} as given by equation (2.1.36).

$$\mu_{n0}(Si) = \frac{5.10\times10^{18} + 92N_D^{\,0.91}}{3.75\times10^{15} + N_D^{\,0.91}}, \tag{2.1.36}$$

$$\mu_n(V_{DS}, N_D) = \frac{\mu_{n0}}{\left(1+\left(\frac{V_{DS}}{E_C L}\right)^{\frac{1}{m}}\right)^{3m}}, \; m=1.73 \tag{2.1.25}$$

The analytical R_{sp} (black lines) in Figure 2.12 shows very good agreement with the simulation results (red lines) in the range of 0.05 ~ 0.35 (a/d). The concentration of the pillars at a given cell pitch is determined by equation (2.1.23) at β= 0.5.

$$N_D(Si) = \frac{1}{\sqrt{2}}\frac{\varepsilon_{Si}E_{C.Si}}{q\beta d} = 5.30\times10^{11}\cdot(\beta d)^{-8/7}, \tag{2.1.23}$$

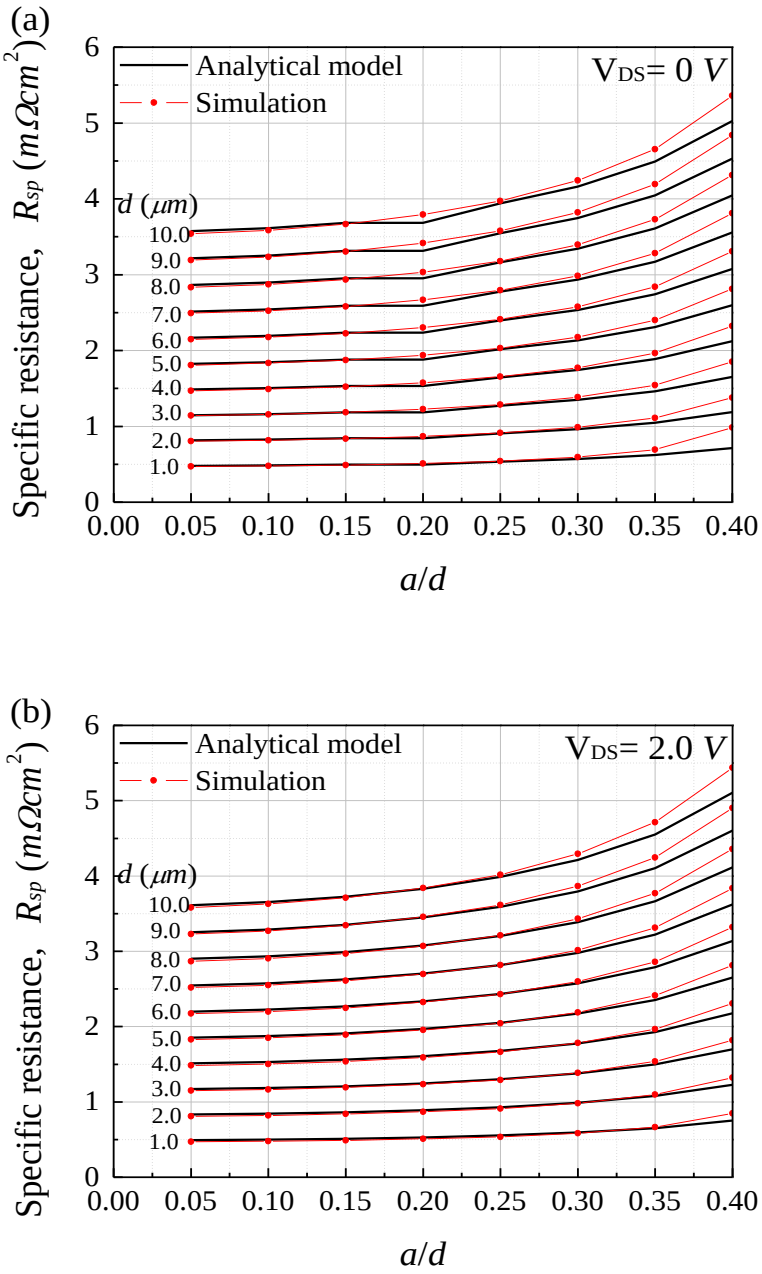

Figure 2.12 Simulation results (red dot lines) and the analytic model (black lines) given by equation (3.43) at (a) V_{DS}= 0, and (b) V_{DS}= 2.0 V. The length of pillar, L=30 μm.

2.3. Compensated Pillar Model

Another possible structure of a superjunction device is based on a compensated pillar structure, shown in figure 2.13. In the case of Si device, owing to the high diffusivity of doped ions in the pillars, the boundary between the n-pillar and p-pillar experiences high rate of compensation (at least 70 %) during the thermal process [28]. As a result, the junction region of the pillars presents very low concentration. The low doping concentration region near the pillar junction can sustain more drain voltage according to Poisson equation as shown in figure 2.14 and hence the parasitic depletion width toward the n-pillar can be decreased.

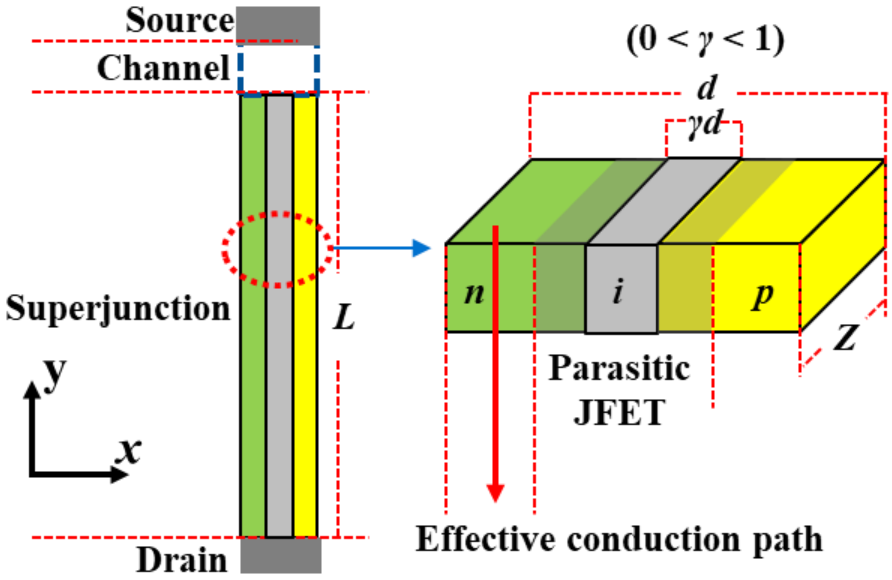

Figure 2.13 A schematic illustration of a compensated pillar superjunction device [53].

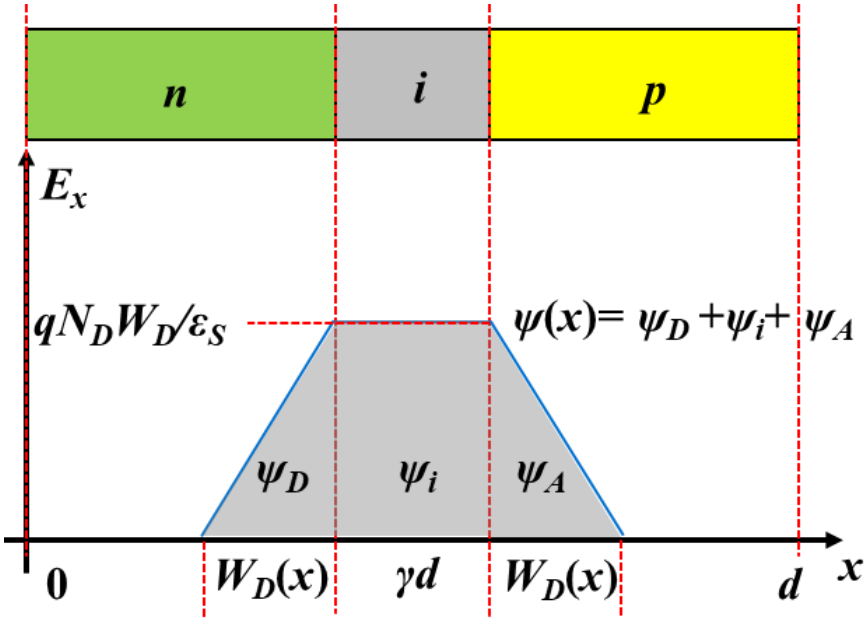

Figure 2.14 A schematic illustration of a lateral electric field at a given drain voltage [53].

2.3.1. Ideal Approach

The width of the n-pillar and the p-pillar are the same in this approach. To develop the model for the compensated pillar, the ideal approach (without parasitic JFET in the pillars) is carried out first. The ideal specific resistance for the compensated pillar superjunction is

$$R_{sp.ideal} = \frac{1}{qN_D\mu_n}\frac{L}{Z\left(d-\gamma d\right)/2}dZ = \frac{2L}{qN_D\mu_n}\frac{1}{\left(1-\gamma\right)} \tag{2.3.1}$$

Where γ is the width factor for the compensated region. As the same way given by section 2.1, the lateral electric field should be less than the critical electric field,

$$E_x = \alpha E_C = \frac{qN_D}{\varepsilon_S}\left(\frac{d-\gamma d}{2}\right), (0<\alpha<1) \tag{2.3.2}$$

With the equation given by 2.1.3, the breakdown voltage is the sum of the areas under the lateral electric field, $V_L + V_i$, and the vertical electric field, V_V,

$$E_y = E_C\sqrt{1-\alpha^2}\ ,\ \because E_x + E_y = {E_C}^2\ , \tag{2.1.3}$$

$$V_B = V_L + V_i + V_V = \alpha E_C \frac{(1+\gamma)}{2} d + E_C L\sqrt{1-\alpha^2} \approx E_C L\sqrt{1-\alpha^2} \tag{2.3.3}$$

Where V_L is lateral voltage formed across the p-pillar, the compensated pillar, and the n-pillar. Considering the superjunction structure has a relatively long length of the pillar, L, to the cell pitch, d, the breakdown voltage can be assumed to be only by the vertical voltage. Combining equations (2.3.1), (2.3.2) and (2.3.3), the material form of the ideal specific resistance of a compensated pillar superjunction becomes the same relationship of the conventional superjunction given by equation (2.1.6),

$$R_{sp} = \frac{V_B}{\alpha\sqrt{1-\alpha^2}\,\mu_n \varepsilon_S {E_C}^2} d = \frac{2V_B}{\mu_n \varepsilon_S {E_C}^2} d\ ,\ \alpha = \frac{1}{\sqrt{2}} \tag{2.1.6}$$

2.3.2. JFET Approach

The newly developed parasitic JFET model, in section 2.1 can be also applied to the compensated pillar structure, where p-type pillar is the grounded gate of the JFET and n-type pillar is the channel of the JFET. The compensated (intrinsic) region is always depleted, even without an applied bias, owing to the built-in potential between the p-pillar and the n-pillar.

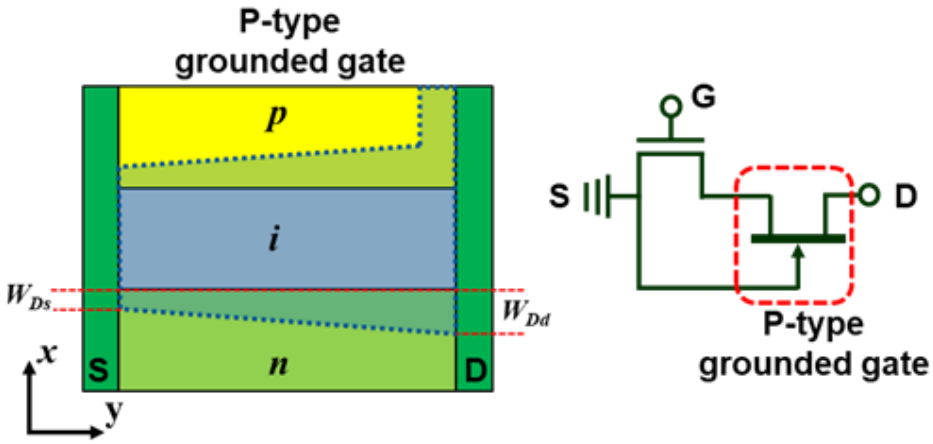

Figure 2.15 A schematic illustration of parasitic depletion width across the compensated pillar and the suggested inner circuit model [53].

The depletion widths shown in figure 2.14 can be obtained from the relationship with the applied potential, $\psi(y)$,

$$\psi(y) = \psi_D + \psi_A + \psi_i = \frac{qN_D}{\varepsilon_S} W_D{}^2 + \frac{qN_D}{\varepsilon_S} W_D \gamma d \tag{2.3.4}$$

Where ψ_D, ψ_A, and ψ_i are the potential sustained on the n-pillar, p-pillar, and the compensated pillar, respectively. Since the pillar structure is symmetric (the same width and doping concentration of the n-pillar and the p-pillar) the sustained potential on the n-pillar and the p-pillar is the same ($\psi_D = \psi_A$).

$$\partial\psi = \left(2\frac{qN_D}{\varepsilon_S} W_D + \frac{qN_D}{\varepsilon_S}\gamma d \right) \partial W_D , \tag{2.3.5}$$

$$\sqrt{\frac{\varepsilon_S \psi(y)}{qN_D} + \frac{\gamma^2 d^2}{4}} - \frac{\gamma d}{2} = W_D(y) , \tag{2.3.6}$$

$$\sqrt{\frac{\varepsilon_S \psi_{bi}}{qN_D} + \frac{\gamma^2 d^2}{4}} - \frac{\gamma d}{2} = W_{Ds} , \tag{2.3.7}$$

$$\sqrt{\frac{\varepsilon_S (\psi_{bi} + V_{DS})}{qN_D} + \frac{\gamma^2 d^2}{4}} - \frac{\gamma d}{2} = W_{Dd} \tag{2.3.8}$$

The sheet charge density in the n-pillar is:

$$Q_n(y) = qN_D \left(\frac{d - \gamma d}{2} - W_D(y) \right) \tag{2.3.9}$$

By the same way given by section 2.1 and 2.2, the drain current as a function of V_{DS} can be obtained with the following equations,

$$v(y) = \mu_n \frac{d\psi(y)}{dy} , \tag{2.1.12}$$

$$I_D = \frac{Z}{L} \int_0^L Q_n(y) v(y) dy , \tag{2.1.13}$$

$$I_D = \frac{Z\mu_n q^2 {N_D}^2}{\varepsilon_S L} \times \left\{ -\frac{2}{3} \left[\left(W_{Dd} + \frac{\gamma d}{2} \right)^3 - \left(W_{Ds} + \frac{\gamma d}{2} \right)^3 \right] + \frac{d}{2} \frac{\varepsilon_S V_{DS}}{qN_D} \right\} \tag{2.3.10}$$

From equation (2.3.10), specific resistance of a compensated superjunction becomes

$$R_{sp} = \frac{V_{DS}}{I_D} dZ =$$
$$\frac{\varepsilon_S dL}{\mu_n q^2 {N_D}^2} \times \frac{V_{DS}}{-\frac{2}{3}\left[\left(W_{Dd} + \frac{\gamma d}{2}\right)^3 - \left(W_{Ds} + \frac{\gamma d}{2}\right)^3\right] + \frac{d}{2}\frac{\varepsilon_S V_{DS}}{qN_D}} \tag{2.3.11}$$

As V_{DS} approaches zero, the specific resistance given by equation (2.3.11) has a minimum value,

$$\lim_{V_{DS}\to 0} \frac{\varepsilon_S dL}{\mu_n q^2 {N_D}^2} \times \frac{V_{DS}}{-\frac{2}{3}\left[\left(W_{Dd} + \frac{\gamma d}{2}\right)^3 - \left(W_{Ds} + \frac{\gamma d}{2}\right)^3\right] + \frac{d}{2}\frac{\varepsilon_S V_{DS}}{qN_D}} \tag{2.3.12}$$
$$= \frac{2L}{qN_D\mu_n}\left(\frac{d - \gamma d}{d - \gamma d - 2W_{Ds}}\right)$$

When the width of compensated pillar region is zero, $\gamma = 0$, the specific resistance given by (2.3.12) becomes the specific resistance of a conventional superjunction given by equation (2.1.19),

$$\lim_{\gamma\to 0} \frac{2L}{qN_D\mu_n} \frac{d - \gamma d}{d - \gamma d - 2\left(\sqrt{\frac{\varepsilon_S \psi_{bi}}{qN_D} + \frac{\gamma^2 d^2}{4}} - \frac{\gamma d}{2}\right)} = \frac{2L}{qN_D\mu_n} \frac{d}{d - 2\sqrt{\frac{\varepsilon_S \psi_{bi}}{qN_D}}} \tag{2.3.13}$$

The optimum concentration at a given cell pitch is derived from equation (2.3.2), and the concentration in the superjunction should be increased with increasing the width of the compensated region, γd,

$$N_D = \frac{1}{\sqrt{2}} \frac{E_C \varepsilon_S}{q}\left(\frac{2}{d - \gamma d}\right) \tag{2.3.14}$$

To find the improvement of the compensated pillar superjunction compared to the conventional superjunction shown in section 2.1, the ratios of the specific resistance are plotted in figure 2.16 for Si and 4H-SiC. The doping concentration was close to the half of the optimum concentration, at a given cell pitch for a practical implementation. The mobility degradation model with respect to the applied V_{DS} is as follows:

$$\mu_n(V_{DS}) = \mu_{n0} / \left(1+\left(\frac{V_{DS}}{E_C L}\right)^{\frac{1}{m}}\right)^{3m}, \quad m = 1.32 + 4\gamma \tag{2.3.15}$$

$$\mu_{n0}(Si) = \frac{5.10\times10^{18} + 92N_D{}^{0.91}}{3.75\times10^{15} + N_D{}^{0.91}} \tag{2.1.25}$$

$$\mu_{n0}(SiC) = \frac{4.05\times10^{13} + 20N_D{}^{0.61}}{3.55\times10^{10} + N_D{}^{0.61}} \tag{2.1.26}$$

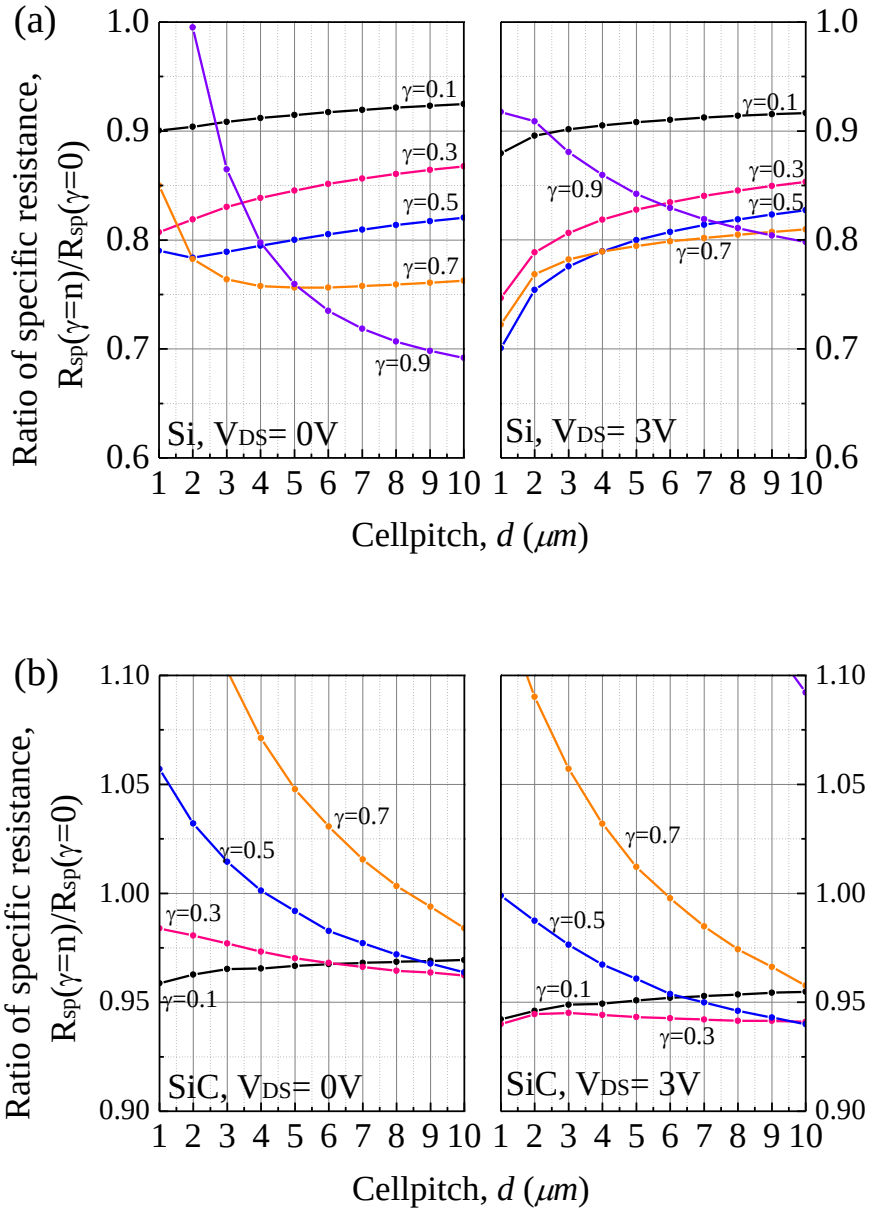

Figure 2.16 Ratio of R_{sp} of the compensated pillar superjunction to the conventional superjunction for (a) Si and (b) SiC at a given cell pitch [53]. Length of pillar, L= 40 μm.

Overall, the compensated pillar has the potential for decreased resistance compared to the conventional pillar. Higher γ (0.7 ~ 0.9) causes a very narrow conducting path (the n-pillar width) at small cell pitches, showing significant increase in the resistance. In the case of SiC

superjunction, the R_{sp} reduction is relatively small compared to the Si because of the rapidly lowered mobility with high doping concentration, $N_D > 1\times10^{16}\ cm^{-3}$. Figure 2.17 shows the output drain current as a function of V_{DS} for Si Superjunction. As the drain voltage increases, the improvement of the drain current becomes prominent, owing to the smaller parasitic JFET effect in the compensated pillar superjunction than the conventional superjunction. The larger JFET region in the n-pillar significantly decreases the saturation current level of the device [54], [55]. More specifically, with an expansion of the depletion width toward the n-pillar with respect to the increased bias, the electrons reach a saturation velocity level presenting a pillar's saturation current. This phenomenon is referred to "quasi-saturation" in a superjunction device [55].

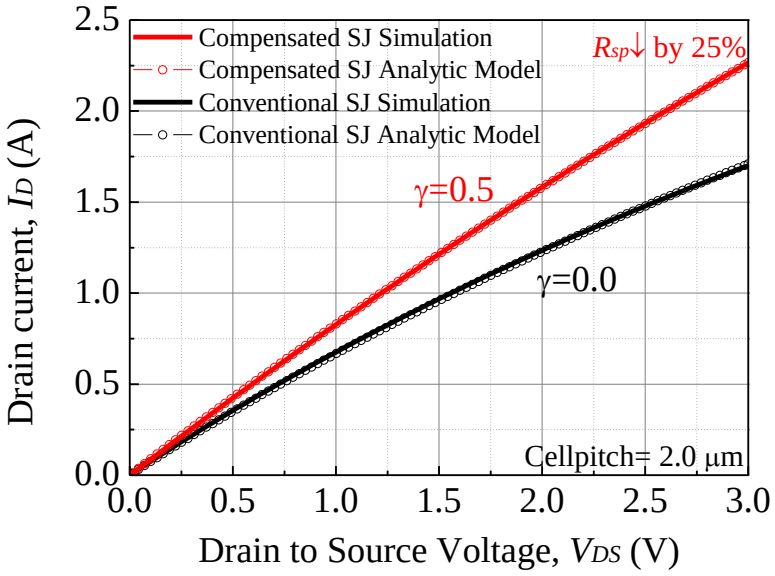

Figure 2.17 Drain current of the compensated pillar superjunction and the conventional pillar superjunction and as a function of drain voltage [53]. Length of pillar, $L = 40\ \mu m$.

In the breakdown voltage simulation, the compensated pillar superjunction showed a similar breakdown voltage to the conventional pillar superjunction, with improved lateral electric field strength in the compensated region, even with a high concentration in the pillars. Also, as

expected in figure 2.1.4, the electric field profile is flat in the compensated region sustaining substantial amount of potential.

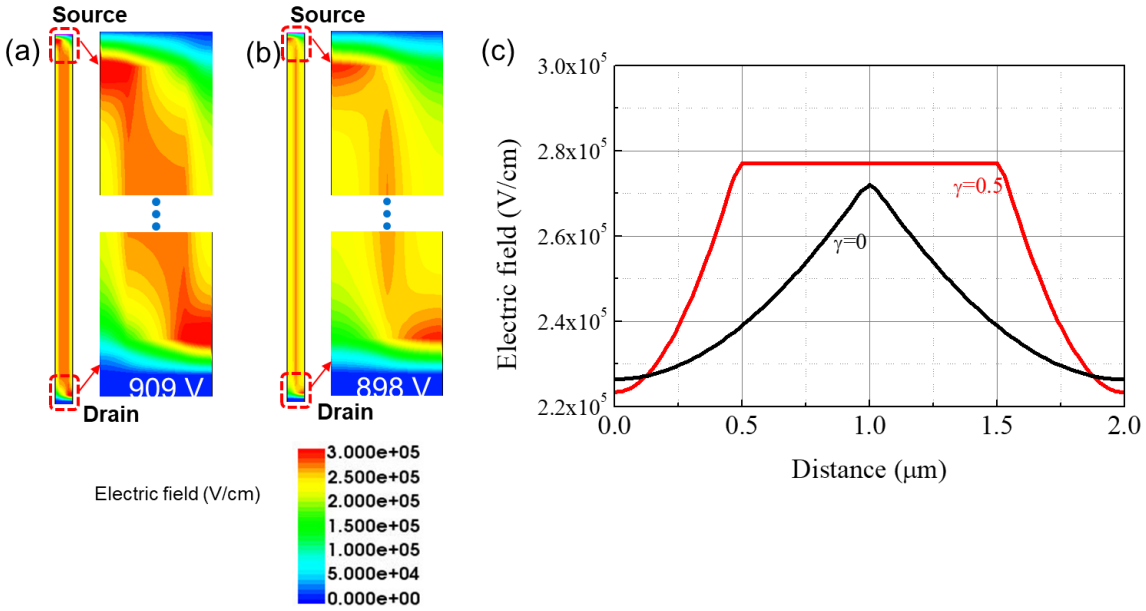

Figure 2.18 Simulated electric field profiles of (a) compensated pillar superjunction, (b) conventional pillar superjunction, and (c) lateral electric field profiles; d= 2 μm. The length of pillar, L= 40 μm, the number of cells: 2.0 $\times 10^5$, N_D (γ = 0.5) = 2.19 $\times 10^{16}$ cm^{-3}, and N_D (γ = 0) = 9.91 $\times 10^{15}$ cm^{-3} [53].

2.4. Oxide Pillar Model

An oxide pillar inserted between the p-pillar and the n-pillar, could be an alternative solution to superjunction devices because of possible reduction in specific resistance. In section 2.3, a compensated pillar superjunction was able to reduce the specific resistance significantly, by increasing the pillar doping concentration. The increased pillar doping concentration was facilitated, when the compensated region sustains substantial amount of the applied bias, including the built-in potential between the pillars. Even though the oxide pillar superjunction could potentially lead to reliability issues such as, time dependent dielectric breakdown owing to the hot carrier injections and interface leakage, the parasitic JFET effect can be effectively reduced during the on-state. As shown in figures 2.19 and 2.20, to understand the electric field profile in a oxide pillar superjunction, Gauss law should be studied first [38].

$$\varepsilon_S E_S = \varepsilon_{ox} E_{ox} \tag{2.4.1}$$

Where, ε_S, ε_{ox}, E_S, and E_{ox} are permittivity of the semiconductor, permittivity of the oxide, electric field of the semiconductor at the interface of the semiconductor and the oxide and electric field in the oxide, respectively. When an electric field transfers from a medium to another medium, the electric field in each medium follows the rule given by equation (2.4.1). The oxide's permittivity, ε_{ox}= 3.9, is 2.5~3 times smaller than that of Si and 4H-SiC and therefore, the lateral electric field profile at a given drain voltage can be schematically drawn as figures 2.19 and 2.20.

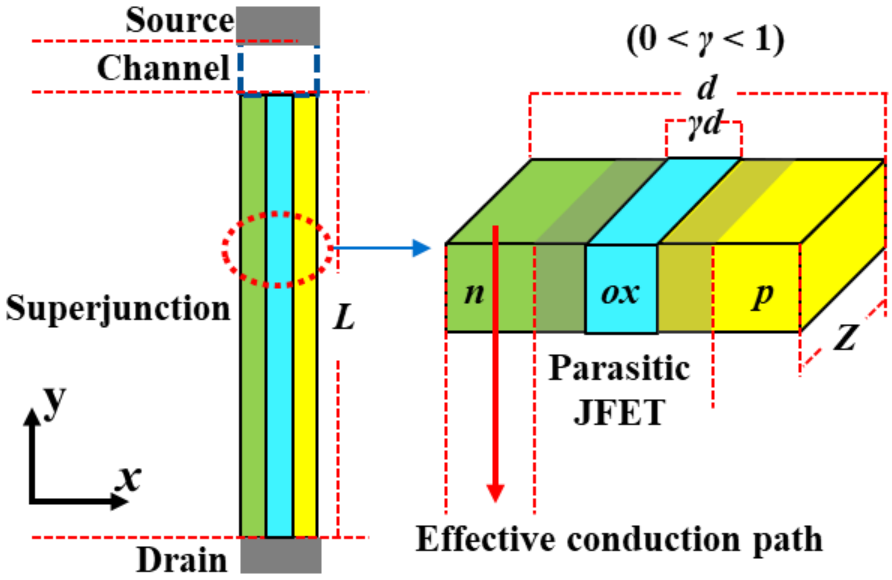

Figure 2.19 A schematic illustration of an oxide pillar superjunction [56].

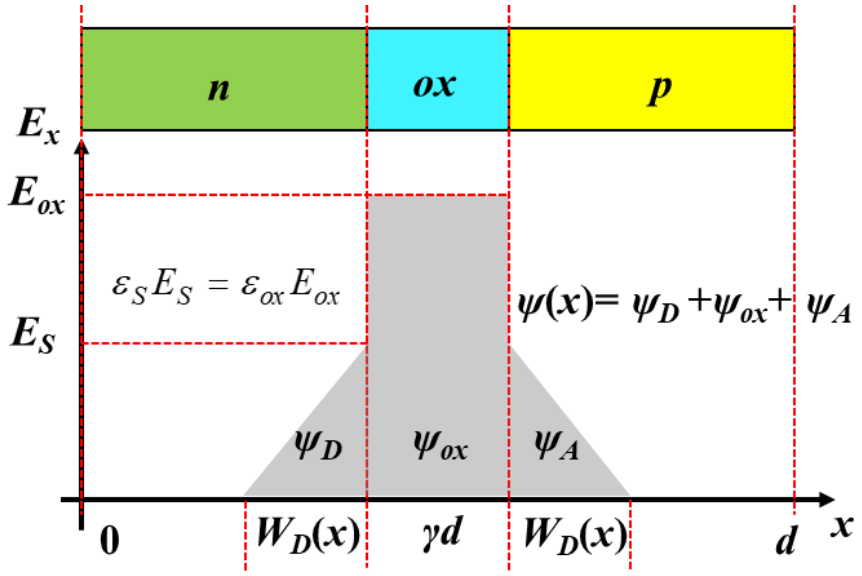

Figure 2.20 A schematic illustration of the lateral electric field profile in an oxide pillar superjunction [56].

2.4.1. Ideal Approach

In an ideal approach, the parasitic JFET toward the n-pillar does not take into account and therefore, the ideal specific resistance of an oxide pillar superjunction is identical as a compensated superjunction:

$$R_{sp.ideal} = \frac{1}{qN_D\mu_n}\frac{L}{Z\left(d-\gamma d\right)/2}dZ = \frac{2L}{qN_D\mu_n}\frac{d}{\left(d-\gamma d\right)} \tag{2.4.2}$$

The calculation procedure for expressing the ideal R_{sp} in terms of material parameters are the same as the compensated pillar superjunction, by rewriting the equations,

$$E_x = \alpha E_C = \frac{qN_D}{\varepsilon_S}\left(\frac{d-\gamma d}{2}\right), (0 < \alpha < 1), \tag{2.3.2}$$

$$E_y = E_C\sqrt{1-\alpha^2}, \because E_x + E_y = {E_C}^2, \tag{2.1.3}$$

$$V_B = V_L + V_{ox} + V_V = \alpha E_C\frac{(1+\gamma)}{2}d + E_C L\sqrt{1-\alpha^2} \approx E_C L\sqrt{1-\alpha^2} \tag{2.3.3}$$

Where V_{ox} is the lateral potential sustained on the oxide pillar region. Even though the oxide pillar region will sustain more lateral electric field than the compensated region, owing to the different dielectric constant, for a simpler calculation, V_{ox} is ignored in total breakdown voltage.

$$R_{sp} = \frac{V_B}{\alpha\sqrt{1-\alpha^2}\mu_n\varepsilon_S{E_C}^2}d = \frac{2V_B}{\mu_n\varepsilon_S{E_C}^2}d\ ,\ \alpha = \frac{1}{\sqrt{2}} \tag{2.1.6}$$

2.4.2. JFET Approach

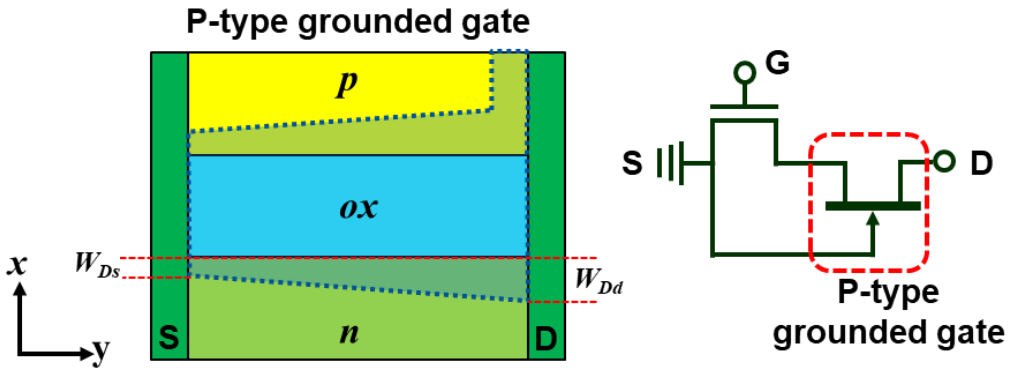

Figure 2.21 A schematic illustration of parasitic depletion in an oxide superjunction and the p-type grounded gate model [56].

To obtain the V_{DS} dependent depletion width toward the conducting path (n-pillar), the relationship between the potential along the conducting path, $\psi(y)$, and the corresponding depletion width, $W_D(y)$ should be established,

$$\psi(y) = \psi_{ox} + 2\psi_D = E_{ox}\gamma d + \frac{qN_D}{\varepsilon_S} W_D(y)^2, \tag{2.4.3}$$

$$\partial\psi = qN_D\left(\frac{2W_D}{\varepsilon_S} + \frac{\gamma d}{\varepsilon_{ox}}\right)\partial W_D, \tag{2.4.4}$$

$$W_D(y) = \sqrt{\frac{\varepsilon_S}{qN_D}\psi(y) + \left(\frac{\varepsilon_S\gamma d}{2\varepsilon_{ox}}\right)^2} - \frac{\varepsilon_S\gamma d}{2\varepsilon_{ox}}, \tag{2.4.5}$$

$$W_{Ds} = \sqrt{\frac{\varepsilon_S\psi_{bi}}{qN_D} + \left(\frac{\varepsilon_S\gamma d}{2\varepsilon_{ox}}\right)^2} - \frac{\varepsilon_S\gamma d}{2\varepsilon_{ox}}, \tag{2.4.6}$$

$$W_{Dd} = \sqrt{\frac{\varepsilon_S \left(\psi_{bi} + V_{DS}\right)}{qN_D} + \left(\frac{\varepsilon_S \gamma d}{2\varepsilon_{ox}}\right)^2} - \frac{\varepsilon_S \gamma d}{2\varepsilon_{ox}} \tag{2.4.7}$$

The sheet charge density at a given distance is

$$Q_n(y) = qN_D\left(\frac{d - \gamma d}{2} - W_D\right), \tag{2.4.8}$$

$$v(y) = \mu_n \frac{d\psi\left(y\right)}{dy}, \tag{2.1.12}$$

$$I_D = \frac{Z}{L}\int_0^L Q_n(y)v(y)dy \tag{2.1.13}$$

By combining the equations given by (2.4.3) ~ (2.4.8), the integral form of equation (2.1.13) leads to

$$I_D = \frac{Z\mu_n q^2 {N_D}^2}{\varepsilon_S L}\int_{W_{Ds}}^{W_{Dd}}\left(\frac{d - \gamma d}{2} - W_D\right)\left(2W_D + \frac{\varepsilon_S \gamma d}{\varepsilon_{ox}}\right)\partial W_D \tag{2.4.9}$$

Solving the integral given by equation (2.4.9) leads to the following relationship,

$$I_D = \frac{Z\mu_n q^2 {N_D}^2}{\varepsilon_S L}\left\{-\frac{2}{3}\left(\left(W_{Dd} + \frac{\varepsilon_S \gamma d}{2\varepsilon_{ox}}\right)^3 - \left(W_{Ds} + \frac{\varepsilon_S \gamma d}{2\varepsilon_{ox}}\right)^3\right) + \frac{1}{2}\left(d - \gamma d + \frac{\varepsilon_S \gamma d}{\varepsilon_{ox}}\right)\frac{\varepsilon_S V_{DS}}{qN_D}\right\} \tag{2.4.10}$$

The specific resistance of an oxide pillar superjunction as a function of V_{DS} can be obtained from equation (2.4.10),

$$R_{sp} = \frac{\varepsilon_S dL}{\mu_n q^2 {N_D}^2} \frac{V_{DS}}{\left\{ -\frac{2}{3}\left(\left(W_{Dd} + \frac{\varepsilon_S \gamma d}{2\varepsilon_{ox}} \right)^3 - \left(W_{Ds} + \frac{\varepsilon_S \gamma d}{2\varepsilon_{ox}} \right)^3 \right) + \frac{1}{2}\left(d - \gamma d + \frac{\varepsilon_S \gamma d}{\varepsilon_{ox}} \right) \frac{\varepsilon_S V_{DS}}{qN_D} \right\}} \tag{2.4.11}$$

The minimum specific resistance at V_{DS}= 0 V is

$$\begin{aligned} \lim_{V_{DS}\to 0} R_{sp}\left(V_{DS}\right) &= \frac{2L}{qN_D\mu_n} \frac{d}{d - \gamma d - 2W_{Ds}} \\ &= \frac{2L}{qN_D\mu_n} \frac{d}{d - \gamma d - 2\left(\sqrt{\frac{\varepsilon_S \psi_{bi}}{qN_D} + \left(\frac{\varepsilon_S \gamma d}{2\varepsilon_{ox}} \right)^2} - \frac{\varepsilon_S \gamma d}{2\varepsilon_{ox}} \right)} \end{aligned} \tag{2.4.12}$$

The R_{sp} given by equation (2.4.12) is highly linked to the compensated pillar superjunction in section 2.3 and the conventional pillar superjunction in section 2.1. By replacing ε_{ox} in equation (2.4.12) to ε_S, the equation leads to the R_{sp} of a compensated pillar superjunction:

$$\begin{aligned} &\lim_{\varepsilon_{ox}\to\varepsilon_S} \frac{2L}{qN_D\mu_n} \frac{d}{d - \gamma d - 2\left(\sqrt{\frac{\varepsilon_S \psi_{bi}}{qN_D} + \left(\frac{\varepsilon_S \gamma d}{2\varepsilon_{ox}} \right)^2} - \frac{\varepsilon_S \gamma d}{2\varepsilon_{ox}} \right)} \\ &= \frac{2L}{qN_D\mu_n} \frac{d}{d - \gamma d - 2\left(\sqrt{\frac{\varepsilon_S \psi_{bi}}{qN_D} + \frac{\gamma^2 d^2}{4}} - \frac{\gamma d}{2} \right)} \end{aligned} \tag{2.4.13}$$

To measure the reduction in the R_{sp} of an oxide pillar superjunction compared to a conventional superjunction, the R_{sp} of ratios of an oxide pillar superjunction to a conventional pillar

superjunction are plotted in figure 2.22. The optimum doping concentration at a given cell pitch is the same as compensated pillar superjunction given by section 2.3.

$$N_D = \frac{1}{\sqrt{2}} \frac{E_C \varepsilon_S}{q} \left(\frac{2}{d - \gamma d} \right) \tag{2.3.14}$$

The doping concentration dependent mobility model is borrowed from Baliga, and the drain voltage dependent mobility is empirically driven,

$$\mu_n \left(V_{DS} \right) = \mu_{n0} / \left(1 + \left(\frac{V_{DS}}{E_C L} \right)^{\frac{1}{m}} \right)^{3m}, \quad m = 1.32 \times e^{\left(\frac{1}{3} \gamma \right)}, \tag{2.4.14}$$

$$\mu_{n0} \left(Si \right) = \frac{5.10 \times 10^{18} + 92 N_D{}^{0.91}}{3.75 \times 10^{15} + N_D{}^{0.91}} \tag{2.1.25}$$

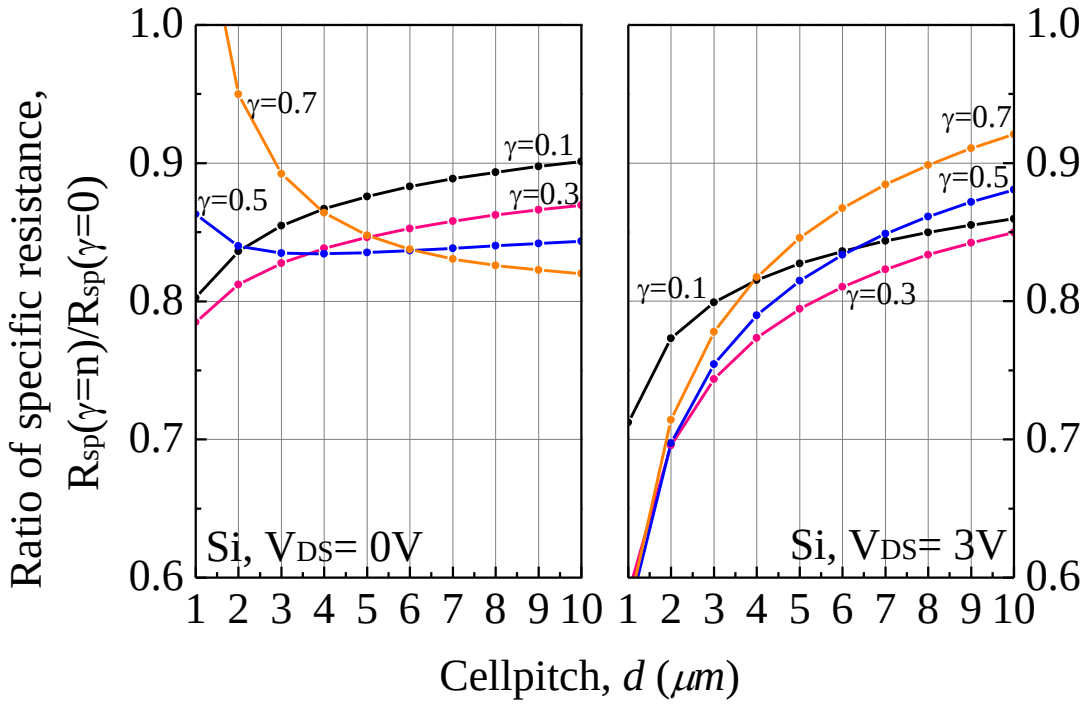

Figure 2.22 Ratio of R_{sp} of an oxide pillar superjunction to a conventional superjunction for Si with respect to the cell pitches. The length of pillar, L= 40 μm [56].

The doping concentration at a given cell pitch, is close to be half of the optimum concentration given by equation (2.3.14) for practical implantation. As the cell pitch decreases, from 10 to 1 μm, the reduction in the R_{sp} of the oxide pillar superjunction becomes prominent owing to the reduced parasitic JFET effect toward the n-pillar. However, a thicker oxide, $\gamma > 0.7$, rather increases the resistance at 0 V due to the narrow conducting path (narrow n-pillar). The output drain current with respect to the drain voltage is shown in figure 2.23. As the drain voltage increases, the drain current of the oxide pillar superjunction shows around 30 % higher value than that of the conventional superjunction.

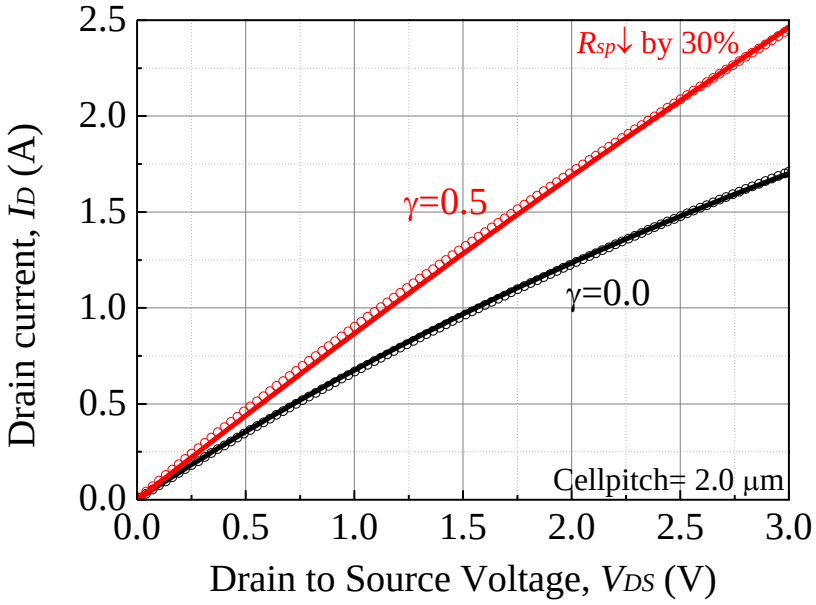

Figure 2.23 Drain current simulation result (lines) and analytic model (circled lines) for the oxide pillar SJ (red) and the conventional SJ (black) when the cellpitch is d= 2 μm. The length of pillar, L= 40 μm, the number of cells: 2.0 $\times 10^5$, N_D (γ = 0.5) = 2.19 $\times 10^{16}$ cm^{-3}, and N_D (γ = 0) = 9.91 $\times 10^{15}$ cm^{-3} [56].

Figures 2.24 shows the electric filed profiles of oxide pillar superjunctions with different oxide pillar thickness. As the oxide pillar thickness increases, the superjunction effect becomes weak having a lower breakdown voltage. The p-pillar interacts with the n+ substrate rather than the n-pillar to be depleted and the n-pillar tends to be depleted with p-body well owing to the thick oxide barrier. Therefore, a narrow oxide pillar (γ= 0.1 or 0.3) is desirable for a best trade-off between the breakdown voltage and the specific resistance. Fig. 2.25 shows the accumulated carrier densities at the interface between the oxide pillar and semiconductor pillars at a reverse bias condition (600 V). When a positive bias, V_{DS}, toward the n-pillar/oxide pillar/p-pillar structure is applied, the positive V_{DS} attracts electrons from the p-pillar and the same amounts of holes are accumulated near the interface between the n-pillar and the oxide pillar. The accumulation phenomenon is much similar to the metal-oxide-semiconductor's depletion and accumulation behavior.

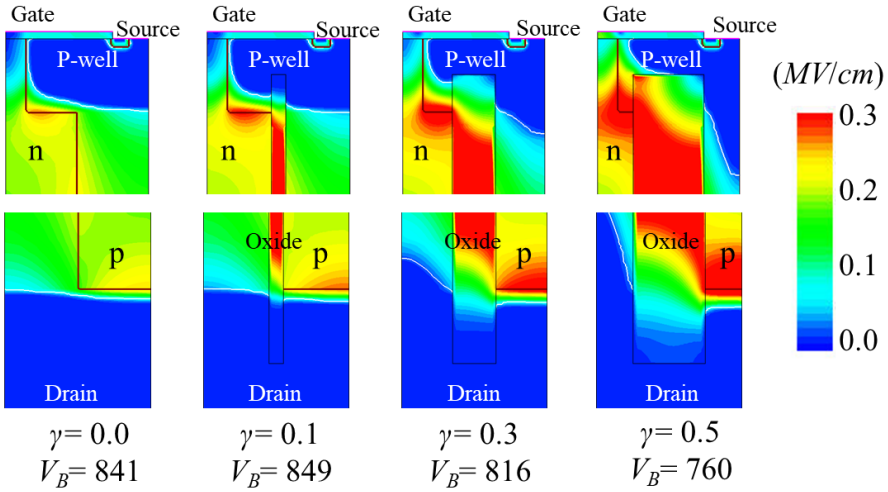

Figure 2.24 Breakdown simulation and the electric field profiles of the oxide pillar superjunctions; d= 2 μm. The length of pillar, L= 40 μm, N_D (γ = 0) = 9.91 ×10^{15} cm^{-3}, N_D (γ= 0.1) = 1.12 ×10^{16} cm^{-3}, N_D (γ = 0.3) = 1.49 ×10^{16} cm^{-3}, and N_D (γ = 0.5) =2.19 ×10^{16} cm^{-3}.

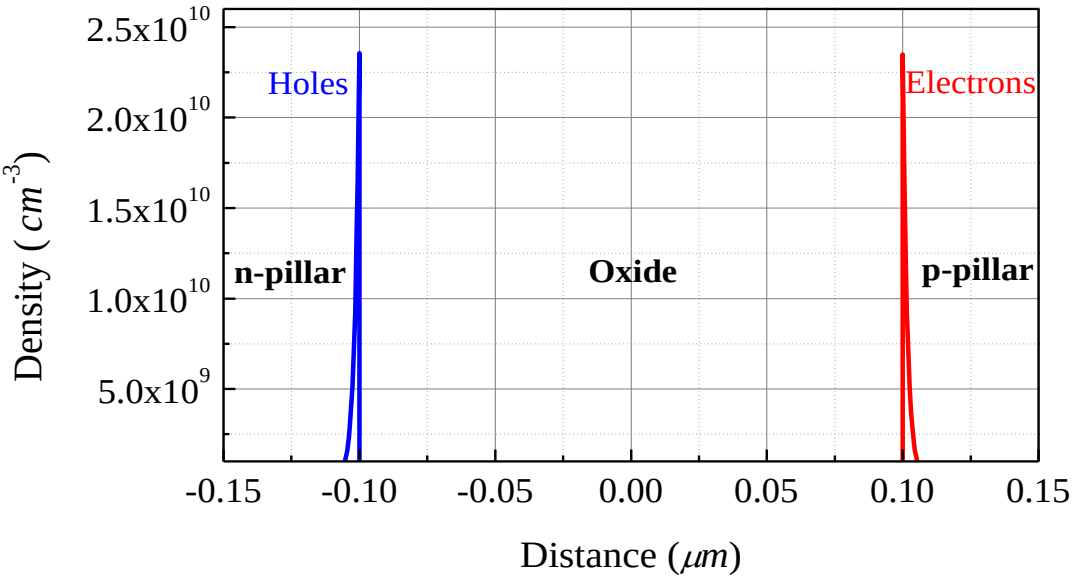

Figure 2.25 Accumulated charge densities near the interface between the oxide pillar and the semiconductor pillars at V_{DS}= 600 V; d= 2 μm. The length of pillar, L= 40 μm, N_D (γ= 0.1) = 1.12 ×10^{16} cm^{-3},

Table 2.3 shows the summary of the specific resistance for each superjunction structure.

Table 2.3 – Summary of specific resistance for each superjunction structure [18], [19], [53], [56].

Pillar type	Specific resistance, R_{sp} ($m\Omega cm^2$)
Conventional	$\frac{L}{q\mu_n N_D \beta}\left(\frac{\beta d}{\beta d - \sqrt{\frac{\varepsilon_S \psi_{bi}}{qN_D}}}\right)$
Sloped	$\frac{L}{q\mu_n N_D}\frac{d}{2a}\cdot\ln\left(\frac{d+2a}{d-2a}\right)\frac{1}{1-\frac{\sqrt{\frac{\varepsilon_S \psi_{bi}}{qN_D}}}{2a}\ln\left(\frac{d+2a}{d-2a}\right)}$
Compensated	$\frac{2L}{qN_D\mu_n}\frac{d-\gamma d}{d-\gamma d-2\left(\sqrt{\frac{\varepsilon_S \psi_{bi}}{qN_D}+\frac{\gamma^2 d^2}{4}}-\frac{\gamma d}{2}\right)}$
Oxide	$\frac{2L}{qN_D\mu_n}\frac{d}{d-\gamma d-2\left(\sqrt{\frac{\varepsilon_S \psi_{bi}}{qN_D}+\left(\frac{\varepsilon_S \gamma d}{2\varepsilon_{ox}}\right)^2}-\frac{\varepsilon_S \gamma d}{2\varepsilon_{ox}}\right)}$

3. 3-D Superjunction MOSFET

Summary

In chapter 2, most of 2-dimensional (2-D) superjunction structures have been discussed where all pillars are parallel stripes. From a newly developed parasitic JFET model, the true limit of 2-D superjunction was able to be derived theoretically. However, the 2-D geometry only utilises lateral and vertical electric field to sustain a given potential and therefore, one would be able to come up with 3-dimensional (3-D) superjunction system, which utilises the third-dimensional electric field. Figure 3.1 shows schematic illustrations of electric field in each dimension system. The peak lateral electric field in 3-D system is half of 2-D at the same doping concentration and therefore, the doping concentration in 3-D could be increased more with sustaining the same breakdown voltage. In the following section, it is shown that for the first time the minimum cell pitch and the specific resistance of 3-D superjunction MOSFET could be lowered compared to that of 2-D shown in section 2. By using the JFET theory, the model of specific resistance will be established and the comparative study with 2-D system carried out.

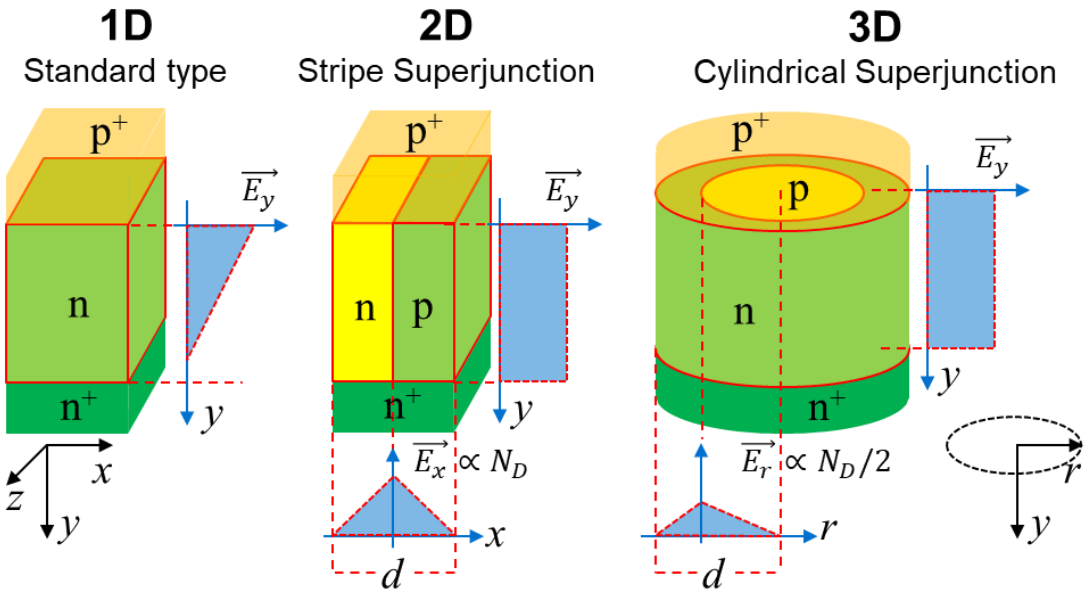

Figure 3.1 Schematic illustration of electric field profile in each dimensional system.

3.1. Core (n-type) – Shell (p-type) Model

3.1.1. Ideal Approach

In radial p-n junctions, the peak electric field can be lowered to that of 2-D for the same pillar concentration. As shown in figure 3.2 the doping concentration in each region is constant, but as the depletion width expands, the slope of the electric field becomes softer resulting in a low peak electric field across the junction. In a real three-dimensional superjunction structure, the unit cell should be arranged in a honeycomb configuration, where one type of a semiconductor is surrounded by another type of a semiconductor. However, for more simple approach, this study assumes that the unit cell is a cylinder where n-type cylinder pillar is surrounded by the p-type cylinder pillar.

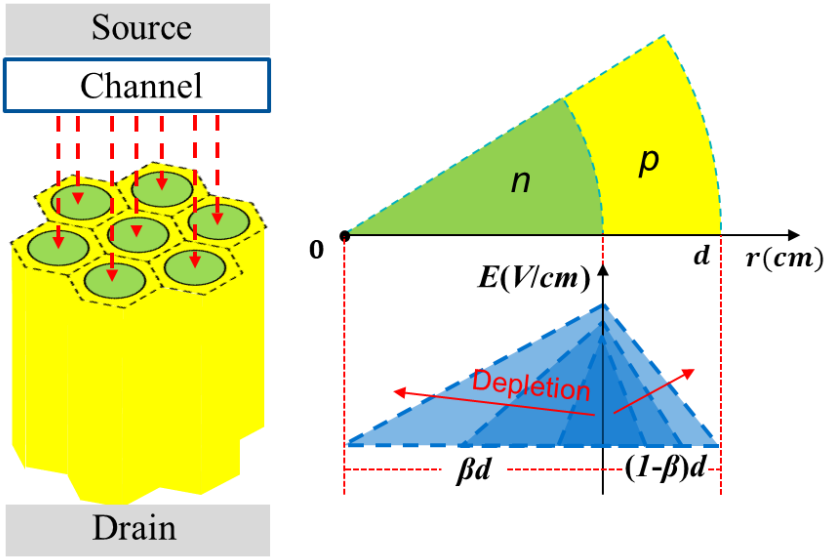

Figure 3.2 Schematic illustrations of a 3D core (n-type) – shell (p-type) superjunction structure and the electric field profile

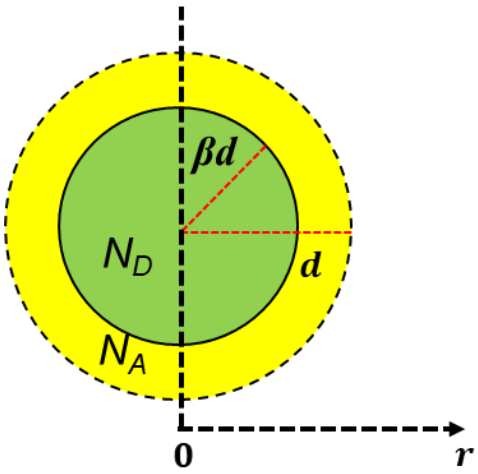

Figure 3.3 Core (n-type) – shell (p-type) radial p-n junction.

For the analytic approach, Poisson equation in a cylindrical coordination system should be employed,

$$\frac{d^2\psi}{dr^2}+\frac{1}{r}\frac{d\psi}{dr}=-\frac{dE}{dr}-\frac{E}{r}=-\frac{\rho}{\varepsilon}r \tag{3.1.1}$$

It should be noted that cylindrical coordination system consists of the radius (r) and the angle (θ). Owing to the perfectly symmetrical radial junction, the angle (θ) effect can be ignored. The charge balance condition of a 3-D superjunction shown in figure 3.3 can be specified as

$$N_D(\beta d)^2 = N_A\left(d^2 - \beta^2 d^2\right) \tag{3.1.2}$$

By solving Poisson equation given by (3.1.1), the electric field as a function of the distance, r, becomes

$$|E(r)| = \begin{cases} \dfrac{qN_D}{2\varepsilon_S}\left(r - \dfrac{C_1}{r}\right) = \dfrac{qN_D}{2\varepsilon_S} r, (0 \le r \le \beta d) \\ -\dfrac{qN_A}{2\varepsilon_S}\left(r - \dfrac{C_2}{r}\right) = \dfrac{qN_A}{2\varepsilon_S}\left(\dfrac{(d)^2}{r} - r\right), (\beta d \le r \le d) \end{cases} \tag{3.1.3}$$

By integrating the electric field, the potential sustained on each pillar can be obtained

$$|\psi| = \begin{cases} \int_0^{\beta d} \dfrac{qN_D}{2\varepsilon_S} r dr = \dfrac{qN_D}{2\varepsilon_S}\left(\dfrac{1}{2}\beta^2 d^2\right), (0 \le r \le \beta d) \\ \int_{\beta d}^{d} \dfrac{qN_A}{2\varepsilon_S}\left(\dfrac{d^2}{r} - r\right) dr = \dfrac{qN_A}{2\varepsilon_S} d^2\left(-\dfrac{1}{2}\left(1-\beta^2\right) - \ln(\beta)\right), (\beta d \le r \le d) \end{cases} \tag{3.1.4}$$

On the boundary of the radial junction, the maximum lateral electric field, when the n-pillar and the p-pillar are fully depleted, should not exceed the critical electric field,

$$E_x = \frac{qN_D}{2\varepsilon_S}\beta d = \alpha E_C, (0 < \alpha \le 1) \tag{3.1.5}$$

$$E_x = \frac{qN_D}{\varepsilon_S}\beta d = \alpha E_C, (0 < \alpha \le 1) \tag{2.1.2}$$

It should be noted that the maximum lateral electric field of a 3-D superjunction given by equation (3.1.5), is the half of the conventional 2-D superjunction given by equation (2.1.2) for

the same pillar concentration. As provided in chapter 2, the square of the critical electric field, E_C, is the sum of the square of the lateral electric field, E_x, and the square of the vertical electric field, E_y,

$$E_y = E_C\sqrt{1-\alpha^2}\ , \tag{2.1.3}$$

From equation given by (2.1.3) and assuming the length of the pillar is long enough compared to the cell pitch, the lateral potential formed by the lateral electric field can be ignored [8]. the breakdown voltage of a 3-D superjunction can be expressed as

$$V_B = \frac{1}{2}\alpha d E_C + E_C L\sqrt{1-\alpha^2} \approx E_C L\sqrt{1-\alpha^2} \tag{2.1.4}$$

The ideal specific resistance of a 3-D superjunction based on figure 3.1.2 is as follows

$$R_{sp} = \frac{1}{q\mu_n N_D}\frac{L}{\pi\beta^2 d^2}\times\pi d^2 = \frac{L}{q\mu_n N_D}\frac{1}{\beta^2} \tag{3.1.6}$$

By combining equations (3.1.5), (2.1.4), and (3.1.6), the specific resistance of a 3-D superjunction can be expressed in terms of material parameters,

$$R_{sp.3D} = \frac{V_B}{\alpha\sqrt{1-\alpha^2}\mu_n\varepsilon_S {E_C}^2}d = \frac{V_B}{\mu_n\varepsilon_S {E_C}^2}\frac{d}{\beta}, \left(\alpha = \frac{1}{\sqrt{2}}\right) \tag{3.1.7}$$

$$R_{sp.2D} = \frac{2V_B}{\mu_n\varepsilon_S {E_C}^2}d \tag{2.1.6}$$

Comparing the R_{sp} relationships given by equations (3.1.7) to (2.1.6), the R_{sp} of a 3-D superjunction could be lowered than that of the 2-D as the β increases more than 0.5.

3.1.2. JFET Approach

As shown in figure 3.4, the parasitic depletion width across toward the n-pillar is formed by the built-in potential and the applied drain voltage. To develop the analytical model for the 3-D superjunction device including the parasitic depletion width, the JFET theory should be employed as described in chapter 2 [18], [19], where the p-pillar is the gate of the JFET and the n-pillar is the channel of the JFET. The p-pillar is normally grounded by the source contact.

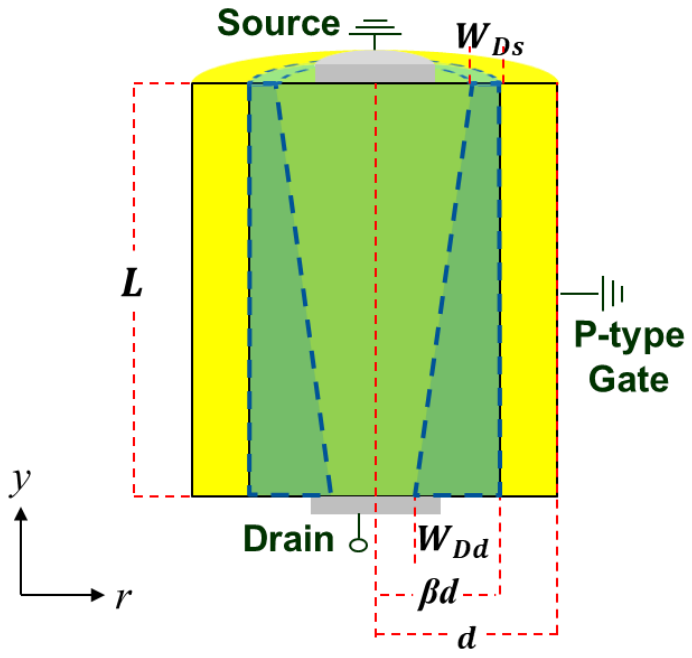

Figure 3.4 A schematic illustration of a 3-D core (n-type) – shell (p-type) superjunction with parasitic depletion widths toward the n-pillar.

By solving Poisson equation given by (3.1.1), the depletion widths in the n-pillar, W_D, and the p-pillar, W_A, have the following relationship,

$$\left|E(r)\right| = \begin{cases} \dfrac{qN_D}{2\varepsilon_S}\left(r - \dfrac{\left(\beta d - W_D\right)^2}{r} \right), (0 \le r \le \beta d) \\ \dfrac{qN_A}{2\varepsilon_S}\left(\dfrac{\left(\beta d + W_A\right)^2}{r} - r \right), (\beta d \le r \le d) \end{cases}, \tag{3.1.8}$$

The potential sustained across the pillars can be obtained by integrating the electric field given by equation (3.1.8),

$$\left|\psi\right| = \begin{cases} \displaystyle\int_{\beta d - W_D}^{\beta d} \frac{qN_D}{2\varepsilon_S}\left(r - \frac{\left(\beta d - W_D\right)^2}{r} \right) dr \\ = \dfrac{qN_D}{2\varepsilon_S}\left(\dfrac{1}{2}\left(\left(\beta d\right)^2 - \left(\beta d - W_D\right)^2 \right) - \left(\beta d - W_D\right)^2 \ln\left(\dfrac{\beta d}{\beta d - W_D} \right) \right) \\ \displaystyle\int_{\beta d}^{\beta d + W_A} \frac{qN_A}{2\varepsilon_S}\left(\frac{\left(\beta d + W_A\right)^2}{r} - r \right) dr \\ = \dfrac{qN_A}{2\varepsilon_S}\left(\left(\beta d + W_A\right)^2 \ln\left(\dfrac{W_A + \beta d}{\beta d} \right) - \dfrac{1}{2}\left(\left(\beta d + W_A\right)^2 - \left(\beta d\right)^2 \right) \right) \end{cases}, \tag{3.1.9}$$

However, the relationship between the depletion width and the applied potential given by equation (3.1.9) is non-linear owing to the log terms and for a simple calculation, the relationship should be linearized by using Taylor series [57]. From equation 3.1.2, the doping concentration in the pillars have the following relationship under the charge balance condition,

$$N_D = N_A \frac{1-\beta^2}{\beta^2} \tag{3.1.10}$$

The depletion width in the n-pillar and the p-pillar should consume the same amounts of ions,

$$N_D\left(\left(\beta d\right)^2 - \left(\beta d - W_D\right)^2 \right) = N_A\left(\left(W_A + \beta d\right)^2 - \left(\beta d\right)^2 \right) \tag{3.1.11}$$

By inserting equation (3.1.10) into (3.1.11) and applying Taylor expansions, the depletion width in the pillars lead to the following relationship,

$$W_D \approx \left(\frac{\beta^2}{1-\beta^2} \right) W_A \tag{3.1.12}$$

From equation (3.1.9) the sum of the potential in the n-pillar and the p-pillar is,

$$\begin{aligned} \psi = & \frac{qN_D}{2\varepsilon_S} \left(\frac{1}{2} \left((\beta d)^2 - (\beta d - W_D)^2 \right) - (\beta d - W_D)^2 \ln \left(\frac{\beta d}{\beta d - W_D} \right) \right) \\ & + \frac{qN_A}{2\varepsilon_S} \left((\beta d + W_A)^2 \ln \left(\frac{W_A + \beta d}{\beta d} \right) - \frac{1}{2} \left((\beta d + W_A)^2 - (\beta d)^2 \right) \right) \end{aligned} \tag{3.1.13}$$

By applying Taylor expansion to the log terms given by equation (3.1.13), the potential becomes a linear function,

$$\psi = \frac{q}{4\varepsilon_S} \beta^2 d^2 \left(N_D \left(-2\frac{W_D}{\beta d} + 3\frac{{W_D}^2}{\beta^2 d^2} \right) + N_A \left(2\frac{W_A}{\beta d} + 3\frac{{W_A}^2}{\beta^2 d^2} \right) \right) \tag{3.1.14}$$

By inserting the charge balance condition given by equation (3.1.10) and the depletion width relationship given by equation (3.1.12) into (3.1.14), the potential and depletion width relationship in a 3-D superjunction becomes

$$\psi(y) = \frac{3qN_D}{4\varepsilon_S} \frac{W_D(y)^2}{\beta^2} \tag{3.1.15}$$

From equation (3.1.15), the depletion width along the pillar can be specified,

$$W_D(y) = \beta \sqrt{\frac{4\varepsilon_S \psi(y)}{3qN_D}}, \tag{3.1.16}$$

$$W_{Ds} = \beta\sqrt{\frac{4\varepsilon_S\psi_{bi}}{3qN_D}}\,, \tag{3.1.17}$$

$$W_{Dd} = \beta\sqrt{\frac{4\varepsilon_S\left(\psi_{bi}+V_{DS}\right)}{3qN_D}}\,, \tag{3.1.18}$$

$$\partial\psi = \frac{3qN_D}{2\varepsilon_S}\frac{W_D}{\beta^2}\partial W_D \tag{3.1.19}$$

The calculation of the drain current follows equation (2.1.13),

$$I_D = \frac{Z}{L}\int_0^L Q_n(y)v(y)dy \tag{2.1.13}$$

Where $Q_n(y)$ and $v(y)$ are

$$Q_n(x) = qN_D\pi(\beta d - W_D)^2\,, \tag{3.1.20}$$

$$v(y) = \mu_n\frac{d\psi\left(y\right)}{dy} \tag{2.1.12}$$

By inserting equations (3.1.19), (3.1.20), and (2.1.12) into (2.1.13), the integral has the following form,

$$I_D = \frac{3\pi q^2\mu_n {N_D}^2}{2\varepsilon_S L}\frac{1}{\beta^2}\int_{W_{Ds}}^{W_{Dd}}(\beta d - W_D)^2 W_D dW_D \tag{3.1.21}$$

By solving the integral given by equation (3.1.21), the total drain current leads to

$$I_D = \frac{\pi q^2\mu_n {N_D}^2}{8\varepsilon_S L}\frac{1}{\beta^2}\left(6\beta^2 d^2\left({W_{Dd}}^2 - {W_{Ds}}^2\right) - 8\left({W_{Dd}}^3 - {W_{Ds}}^3\right)\beta d + 3\left({W_{Dd}}^4 - {W_{Ds}}^4\right)\right) \tag{3.1.22}$$

From the drain current given by equation (3.1.22) the specific resistance of a 3-D superjunction becomes

$$R_{sp} = \frac{V_{DS}}{I_D}\pi d^2 = \frac{8\varepsilon_S L\beta^2 d^2}{q^2\mu_n {N_D}^2}\frac{V_{DS}}{6\beta^2 d^2\left({W_{Dd}}^2 - {W_{Ds}}^2\right) - 8\left({W_{Dd}}^3 - {W_{Ds}}^3\right)\beta d + 3\left({W_{Dd}}^4 - {W_{Ds}}^4\right)} \quad (3.1.23)$$

The specific resistance has the minimum value when V_{DS} approaches zero,

$$\lim_{V_{DS}\to 0} R_{sp} = \frac{L}{q\mu_n N_D}\frac{1}{\beta^2}\left(\frac{\beta d}{\beta d - W_{Ds}}\right)^2 \quad (3.1.24)$$

The pre factor of equation (3.1.22) is the ideal R_{sp} without the parasitic depletion width, and the term in bracket is the JFET factor. By comparing the 3-D superjunction R_{sp} with the conventional 2-D R_{sp}, the second term of 3-D is area ratio because the circle area conducts the current.

$$R_{sp.2D} = \frac{L}{q\mu_n N_D}\frac{1}{\beta}\left(\frac{\beta d}{\beta d - W_{Ds}}\right) \quad (2.1.18)$$

From equations (3.1.24) and (2.1.18) the specific resistance ratio of 3D to 2D can be obtained,

$$R_{sp.3D} = R_{sp.2D}\times\frac{1}{\beta}\left(\frac{\beta d}{\beta d - W_{Ds}}\right) = R_{sp.2D}\times\left(\frac{d}{\beta d - W_{Ds}}\right) \quad (3.1.25)$$

Equation (3.1.25) provides a clear insight that the $R_{sp.3D}$ can be decreased continuously with increasing the β compared to the conventional 2D superjunction.

3.2. Core (p-type) – Shell (n-type) Model

The core-shell superjunction structure given in section 3.1 is less realistic because, in general, n-type epitaxial layer is grown first, and p-type ion implantation process is carried out by forming core (p-type) – shell (n-type) superjunction. As introduced in section 3.1, by solving the radial Poisson equation, this section will aim to establish core (p-type) -shell (n-type) model.

3.2.1. Ideal Approach

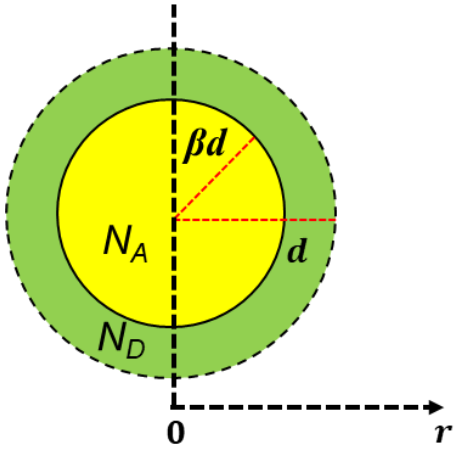

Figure 3.5 Core (p-type) – shell (n-type) radial p-n junction.

As shown in figure 3.5, the inverse core-shell superjunction structure is based on the p-type pillar is surrounded by the n-type pillar. The charge balance condition of the core (p-type) – shell (n-type) is

$$N_A(\beta d)^2 = N_D\left(d^2 - \beta^2 d^2\right) \tag{3.2.1}$$

By applying the radial Poisson equation, the electric field as a function of the radius becomes

$$\left|E(r)\right| = \begin{cases} \dfrac{qN_A}{2\varepsilon_S}\left(r - \dfrac{C_1}{r}\right) = \dfrac{qN_A}{2\varepsilon_S} r, (0 \le r \le \beta d) \\ -\dfrac{qN_D}{2\varepsilon_S}\left(r - \dfrac{C_2}{r}\right) = \dfrac{qN_D}{2\varepsilon_S}\left(\dfrac{(d)^2}{r} - r\right), (\beta d \le r \le d), \end{cases} \tag{3.2.2}$$

By integrating the electric field given by equation (3.2.2), the lateral potential sustained in each pillar is

$$\left|\psi\right| = \begin{cases} \int_0^{\beta d} \dfrac{qN_A}{2\varepsilon_S} r dr = \dfrac{qN_A}{2\varepsilon_S}\left(\dfrac{1}{2}\beta^2 d^2\right), (0 \le r \le \beta d) \\ \int_{\beta d}^{d} \dfrac{qN_D}{2\varepsilon_S}\left(\dfrac{d^2}{r} - r\right) dr = \dfrac{qN_D}{2\varepsilon_S}\left(-\dfrac{1}{2}\left(1-\beta^2\right) - \ln\left(\beta\right)\right) d^2, (\beta d \le r \le d) \end{cases} \tag{3.2.3}$$

From equation (3.2.2), the maximum lateral electric field on the junction should not exceed the critical electric field.

$$E_x = \frac{qN_D}{2\varepsilon_S}\frac{1-\beta^2}{\beta} d = \alpha E_C, \left(0 < \alpha \le 1\right) \tag{3.2.4}$$

The ideal specific resistance of the 3-D core (p-type) – shell (n-type) superjunction is

$$R_{sp} = \frac{L}{qN_D\mu_n}\frac{\pi d^2}{\pi\left(d^2 - \beta^2 d^2\right)} = \frac{L}{qN_D\mu_n}\frac{1}{1-\beta^2} \tag{3.2.5}$$

As shown in chapter 2, only the vertical electric field is assumed to be the breakdown voltage because the length of the pillar is long enough compared to the cell pitch,

$$E_y = E_C\sqrt{1-\alpha^2}\ , \tag{2.1.3}$$

$$V_B = \frac{1}{2}\alpha d E_C + E_C L\sqrt{1-\alpha^2} \approx E_C L\sqrt{1-\alpha^2} \tag{2.1.4}$$

By inserting equations (3.2.4) and (2.1.4) into (3.2.5), the specific resistance can be expressed as the material parameters

$$R_{sp.3D} = \frac{V_B}{\alpha\sqrt{1-\alpha^2}\mu_n \varepsilon_S E_C{}^2} d = \frac{V_B}{\mu_n \varepsilon_S E_C{}^2}\frac{d}{\beta}, \left(\alpha = \frac{1}{\sqrt{2}}\right) \tag{3.1.7}$$

3.2.2. JFET Approach

As introduced previous sections, building an analytic model for a superjunction structure with a parasitic depletion width at a given drain voltage and built-in potential, the JFET model should be employed [37]. The p-type pillar (core) is the grounded gate of the JFET and the n-type pillar (shell) is the channel of the JFET in this case as shown in figure 3.6.

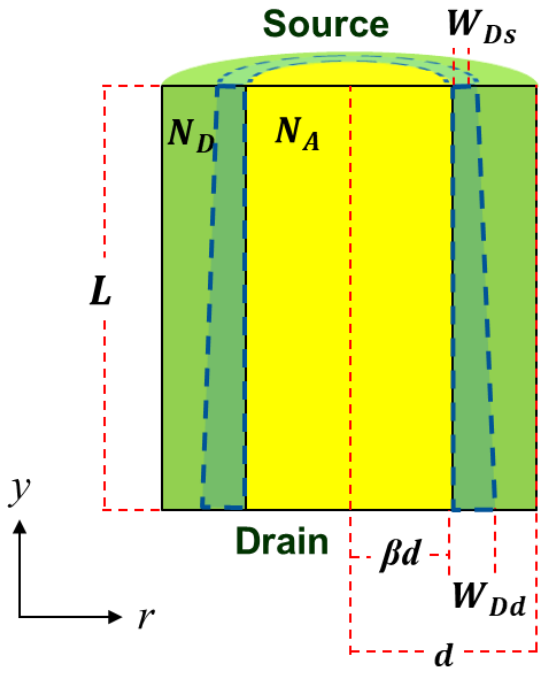

Figure 3.6 A schematic illustration of a 3-D core (p-type) – shell (n-type) superjunction with parasitic depletion widths toward the n-pillar.

From the radial Poisson equation, the electric field and the potential across the junction can be specified in terms of the depletion width in the n-pillar, W_D, and the p-pillar, W_A,

$$|E(r)| = \begin{cases} \dfrac{qN_A}{2\varepsilon_S}\left(r - \dfrac{(\beta d - W_A)^2}{r}\right), (0 \le r \le \beta d) \\ \dfrac{qN_D}{2\varepsilon_S}\left(\dfrac{(\beta d + W_D)^2}{r} - r\right), (\beta d \le r \le d) \end{cases} \tag{3.2.6}$$

By integrating equation (3.2.6), the potential is

$$|\psi| = \begin{cases} \int_{\beta d - W_A}^{\beta d} \frac{qN_A}{2\varepsilon_S}\left(r - \frac{(\beta d - W_A)^2}{r}\right)dr \\ = \frac{qN_A}{2\varepsilon_S}\left(\frac{1}{2}\left((\beta d)^2 - (\beta d - W_A)^2\right) - (\beta d - W_A)^2 \ln\left(\frac{\beta d}{\beta d - W_A}\right)\right), (0 \le r \le \beta d) \\ \int_{\beta d}^{\beta d + W_D} \frac{qN_A}{2\varepsilon_S}\left(\frac{(\beta d + W_D)^2}{r} - r\right)dr \\ = \frac{qN_D}{2\varepsilon_S}\left((\beta d + W_D)^2 \ln\left(\frac{W_D + \beta d}{\beta d}\right) - \frac{1}{2}\left((\beta d + W_D)^2 - (\beta d)^2\right)\right), (\beta d \le r \le d) \end{cases} \quad (3.2.7)$$

As pointed out in section 3.1, the potential given by equation (3.2.7) has a non-linear log function and, for a simple development of the analytic model, the log term should be linearized by using Taylor expansion. During the depletion, the same amounts of the ions in each pillar are consumed,

$$N_A\left((\beta d)^2 - (\beta d - W_A)^2\right) = N_D\left((\beta d + W_D)^2 - (\beta d)^2\right) \quad (3.2.8)$$

By inserting the charge balance condition given by equation (3.2.1) and applying Taylor series, the depletion width has the following relationship

$$N_A(\beta d)^2 = N_D\left(d^2 - \beta^2 d^2\right), \quad (3.2.1)$$

$$\left(\frac{1-\beta^2}{\beta^2}\right) W_A \approx W_D \quad (3.2.9)$$

The total potential sustained on the radial junction is

$$\psi = \frac{qN_A}{4\varepsilon_S}\left(\left((\beta d)^2 - (\beta d - W_A)^2\right) - (\beta d - W_A)^2 \ln\left(\frac{\beta d}{\beta d - W_A}\right)^2\right), \\ + \frac{qN_D}{4\varepsilon_S}\left((\beta d + W_D)^2 \ln\left(\frac{W_D + \beta d}{\beta d}\right)^2 - \left((\beta d + W_D)^2 - (\beta d)^2\right)\right) \tag{3.2.10}$$

By applying Taylor series to the log terms given by equation (3.2.10), the potential leads to

$$\psi = \frac{q}{4\varepsilon_S}\beta^2 d^2\left(N_A\left(-2\frac{W_A}{\beta d} + 3\frac{W_A^{\,2}}{\beta^2 d^2}\right) + N_D\left(2\frac{W_D}{\beta d} + 3\frac{W_D^{\,2}}{\beta^2 d^2}\right)\right) \tag{3.2.11}$$

By inserting equation (3.2.9) into (3.2.11) the potential as a function of depletion width can be simplified as

$$\psi(y) = \frac{3qN_D}{4\varepsilon_S}\frac{W_D(y)^2}{1-\beta^2}, \tag{3.2.12}$$

$$W_{Ds} = \sqrt{1-\beta^2}\sqrt{\frac{4\varepsilon_S\psi_{bi}}{3qN_D}}, \tag{3.2.13}$$

$$W_{Dd} = \sqrt{1-\beta^2}\sqrt{\frac{4\varepsilon_S(\psi_{bi} + V_{DS})}{3qN_D}}, \tag{3.2.14}$$

$$\partial\psi = \frac{3qN_D}{2\varepsilon_S}\frac{W_D}{1-\beta^2}\partial W_D \tag{3.2.15}$$

The drain current as a function of the applied bias can be obtained by solving the integral,

$$I_D = \frac{Z}{L}\int_0^L Q_n(y)v(y)dy \tag{2.1.13}$$

Where $Q_n(y)$ and $v(y)$ are

$$Q_n(y) = qN_D\pi\left(d^2 - \left(\beta d + W_D\right)^2\right), \tag{3.2.16}$$

$$v(y) = \mu_n \frac{d\psi(y)}{dy} \tag{2.1.12}$$

By inserting equations (3.2.12), (3.2.16) and (2.1.12) into (2.1.13) the integral leads to

$$I_D = \frac{3\pi q^2 \mu_n {N_D}^2}{2\varepsilon_S L} \frac{1}{1-\beta^2} \int_{W_{Ds}}^{W_{Dd}} \left(d^2 - \left(\beta d + W_D\right)^2\right) W_D dW_D \tag{3.2.17}$$

Solving the integral given by equation (3.2.17) produces the following drain current

$$\begin{aligned} I_D = & \frac{\pi q^2 \mu_n {N_D}^2}{8\varepsilon_S L} \frac{1}{1-\beta^2} \times \\ & \left(-3\left({W_{Dd}}^4 - {W_{Ds}}^4\right) - 8\beta d\left({W_{Dd}}^3 - {W_{Ds}}^3\right) + 6\left(1-\beta^2\right) d^2 \left({W_{Dd}}^2 - {W_{Ds}}^2\right)\right) \end{aligned} \tag{3.2.18}$$

From equation (3.2.18), the specific resistance for a core (p-type) – shell (n-type) 3-D superjunction becomes

$$\begin{aligned} R_{sp} = \frac{V_{DS}}{I_D}\pi d^2 = & \frac{8\varepsilon_S L d^2\left(1-\beta^2\right)}{q^2 \mu_n {N_D}^2} \times \\ & \frac{V_{DS}}{\left(-3\left({W_{Dd}}^4 - {W_{Ds}}^4\right) - 8\beta d\left({W_{Dd}}^3 - {W_{Ds}}^3\right) + 6\left(1-\beta^2\right) d^2 \left({W_{Dd}}^2 - {W_{Ds}}^2\right)\right)} \end{aligned} \tag{3.2.19}$$

The specific resistance given by equation (3.2.19) has the minimum value when V_{DS} approaches zero,

$$\lim_{V_{DS}\to 0} R_{sp} = \frac{L}{q\mu_n N_D}\frac{1}{1-\beta^2}\left(\frac{d^2-\beta^2 d^2}{d^2-\left(\beta d+W_{Ds}\right)^2}\right)=\frac{L}{q\mu_n N_D}\left(\frac{d^2}{d^2-\left(\beta d+W_{Ds}\right)^2}\right) \tag{3.2.20}$$

$$R_{sp.core} = \frac{L}{q\mu_n N_D}\frac{1}{\beta^2}\left(\frac{\beta d}{\beta d-W_{Ds}}\right)^2 \tag{3.1.22}$$

The pre term of R_{sp} given by equation (3.2.20) is the ideal specific resistance and the term in the bracket is the increment of the R_{sp} owing to the parasitic depletion width. Equation (3.2.20) can be intuitively derived considering the effective conducting area to the total area. In the next chapter, both analytic models given by equations (3.1.22) and (3.2.20) will be proven by simulation and the comparisons will be carried out.

3.2.3. Proofs and Comparisons of 3-D Superjunctions

In the last two sections, two specific resistance models for 3-D superjunctions were established. In this section, the advantage of 3-D superjunction over 2-D superjunction will be discussed. To draw the specific resistance of the 3-D superjunction with respect to the cell pitches given by equations (3.1.22) and (3.2.20), the optimum pillar doping concentration should be defined first.

$$R_{sp.core} = \frac{L}{q\mu_n N_D}\frac{1}{\beta^2}\left(\frac{\beta d}{\beta d - W_{Ds}}\right)^2, \tag{3.1.22}$$

$$R_{sp.shell}\frac{L}{q\mu_n N_D}\left(\frac{d^2}{d^2-\left(\beta d + W_{Ds}\right)^2}\right) \tag{3.2.20}$$

Where $R_{sp.core}$ is the minimum specific resistance of core (n-type) -shell (p-type) and $R_{sp.shell}$ is the minimum specific resistance of core (p-type) -shell (n-type).

$$E_{x.core} = \frac{qN_D}{2\varepsilon_S}\beta d = \alpha E_C, \left(0 < \alpha \le 1\right) \tag{3.1.5}$$

$$E_{x.shell} = \frac{qN_D}{2\varepsilon_S}\frac{1-\beta^2}{\beta} d = \alpha E_C, \left(0 < \alpha \le 1\right) \tag{3.2.4}$$

From the maximum lateral electric field relationship given by equation (3.1.5) and (3.2.4), the optimum doping concentration for each 3-D superjunction can be defined,

$$N_{D.core} = \sqrt{2}\frac{\varepsilon_S E_C}{q\beta d}, \tag{3.3.1}$$

$$N_{D.shell} = \sqrt{2}\frac{\varepsilon_S \beta E_C}{q\left(1-\beta^2\right)d} \tag{3.3.2}$$

Comparing the optimum concentration of the 2-D conventional superjunction given by equation (2.1.22), the 3-D superjunction's doping concentration is two times higher than that of 2-D.

$$N_{D.2D} = \frac{\sqrt{2}}{2}\frac{\varepsilon_S E_C}{q\beta d} \tag{2.1.22}$$

The optimum doping concentrations for 3-D superjunction given by equation (3.3.1) and (3.3.2) are plotted in figure 3.7 as a function of cell pitch.

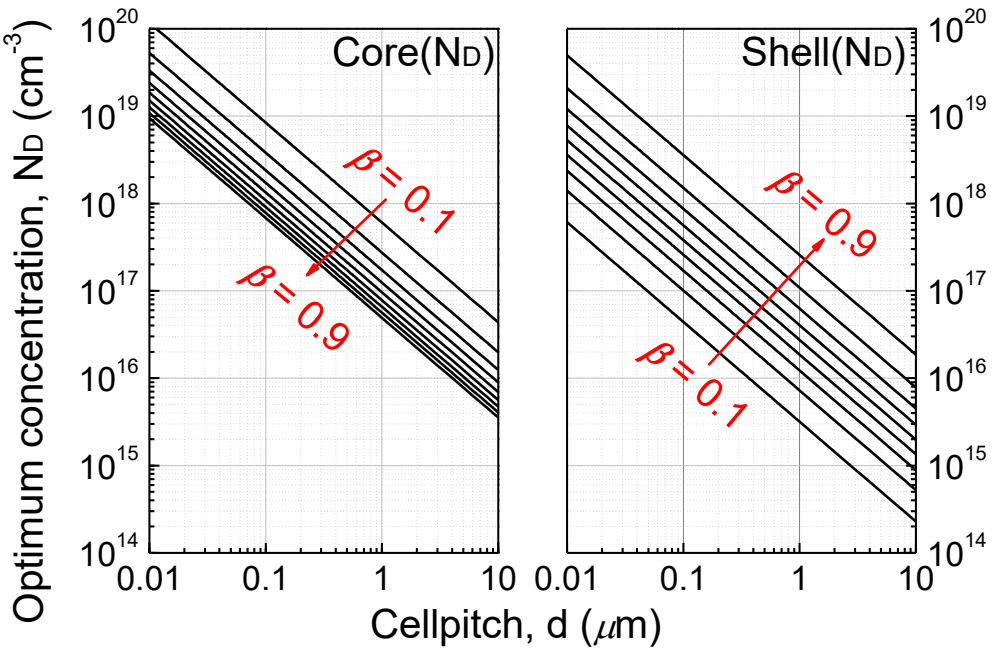

Figure 3.7 um doping concentrations of 3-D superjunction,
(left): core (n-type) – shell (p-type), (right): (left): core (p-type) – shell (n-type).

The doping dependent mobility is borrowed from Baliga [41],

$$\mu_n(Si) = \frac{5.10\times10^{18} + 92N_D^{0.91}}{3.75\times10^{15} + N_D^{0.91}} \tag{2.1.25}$$

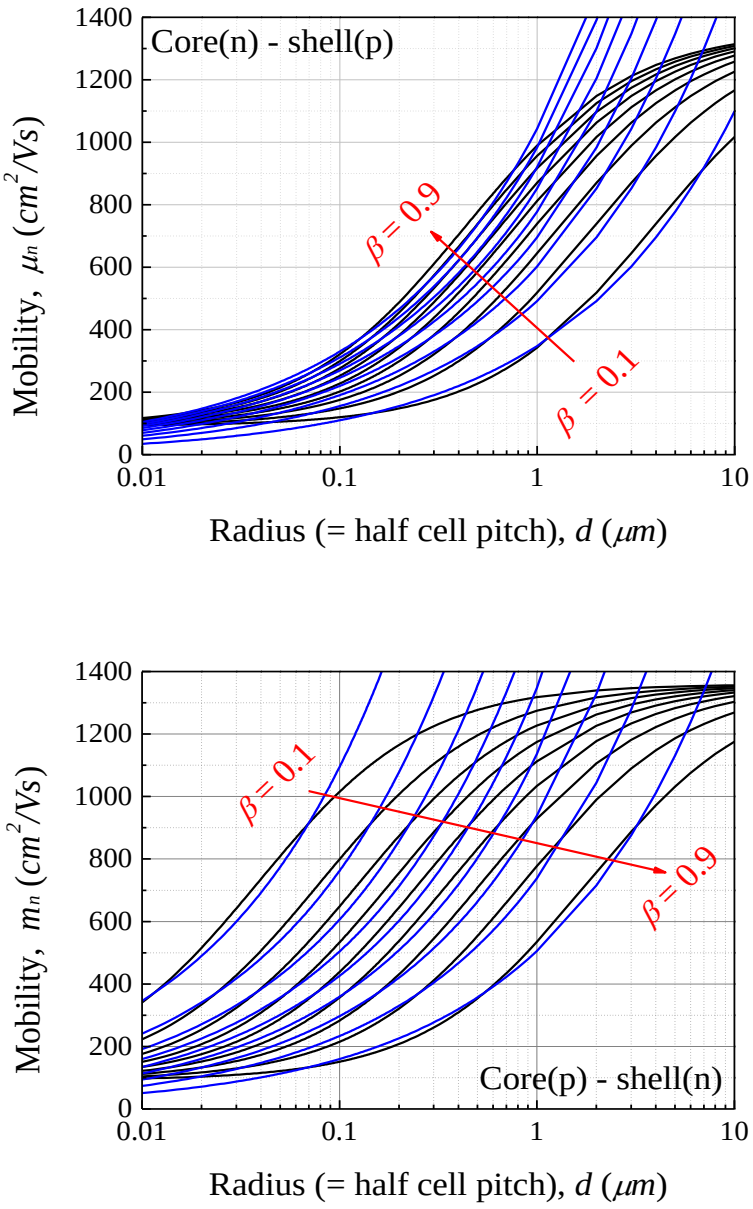

Figure 3.8 Black lines: mobility of 3-D superjunctions as a function of cell pitch, blue lines, approximated mobility at low cell pitches.

Figure 3.8 shows the doping concentration dependent mobility at given cell pitches (black lines). The mobility at low cell pitches can be approximated as exponential functions (blue lines),

$$\mu_{n.core} \approx 1100 \times (\beta d)^{1/2}, \tag{3.3.3}$$

$$\mu_{n.shell} \approx 1100 \times \left(\frac{1-\beta^2}{\beta} d \right)^{1/2} \tag{3.3.4}$$

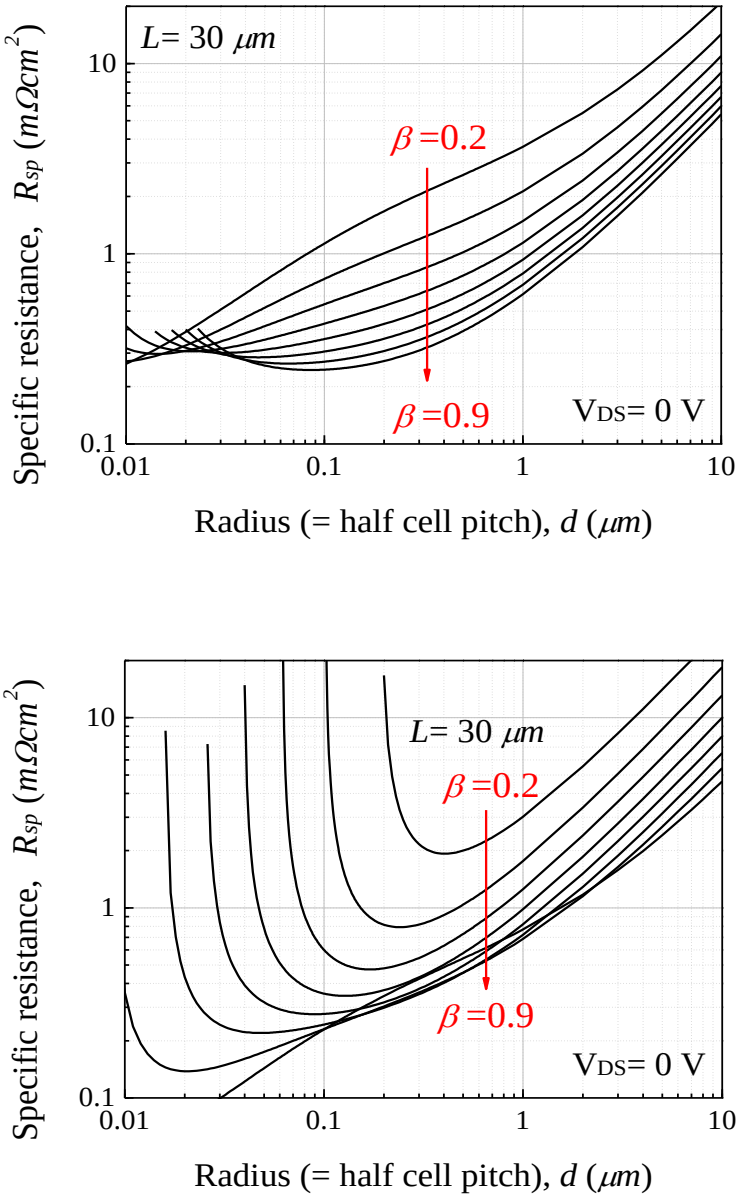

Figure 3.9 Specific resistance of 3-D superjunctions as a function of cell pitch. Length of pillar L= 30 μm.

Finally, the minimum specific resistance of both 3-D superfunctions, with respect to the given cell pitch are shown in figure 3.9. From 10 μm to 1 μm of cell pitch, both superjunctions show very similar R_{sp} and a higher β a lower R_{sp}. For a scaling down to sub-micro cell pitch, core (n-type) -shell (p-type) is desirable because the minimum cell pitch of core (p-type) -shell (n-type) superjunction is located at higher cell pitches than that of core (n-type) -shell (p-type).

Figure 3.10 shows the analytical models and the simulation data in the range of 10 μm to 2 μm cell pitches. The analytical model shows a very good agreement with the simulation. Owing to the high diffusion (compensation) rate of impurities in silicon, it is not easy to make a sub-micro cell pitch device. However, compared to the conventional 2D superjunction, a higher β ($\beta > 0.7$) 3D superjunction device will present a significantly lowered specific resistance even with the similar technological barrier.

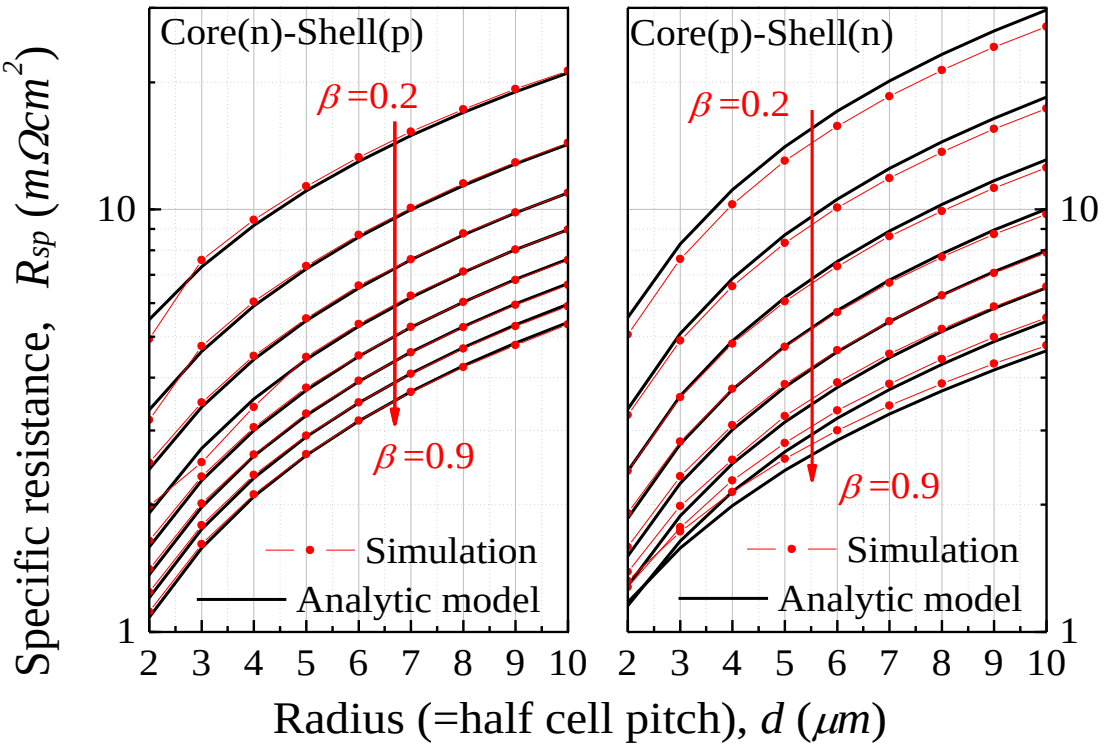

Figure 3.10 Specific resistance of 3-D superjunctions, analytic model (black lines) and simulation (red dotted lines). Length of pillar L= 30 μm.

To find an improvement of 3-D superjunctions compared to the conventional 2-D superjunction, the R_{sp} ratios with respect to the cell pitch are shown in figure 3.11. Above β= 0.7 (blue lines), the specific resistance can be decreases at least 20 % for both 3-D superjunctions compared to the 2-D conventional superjunction. Therefore, when designing 3-D superjunction devices, higher β is desirable for a low R_{sp}.

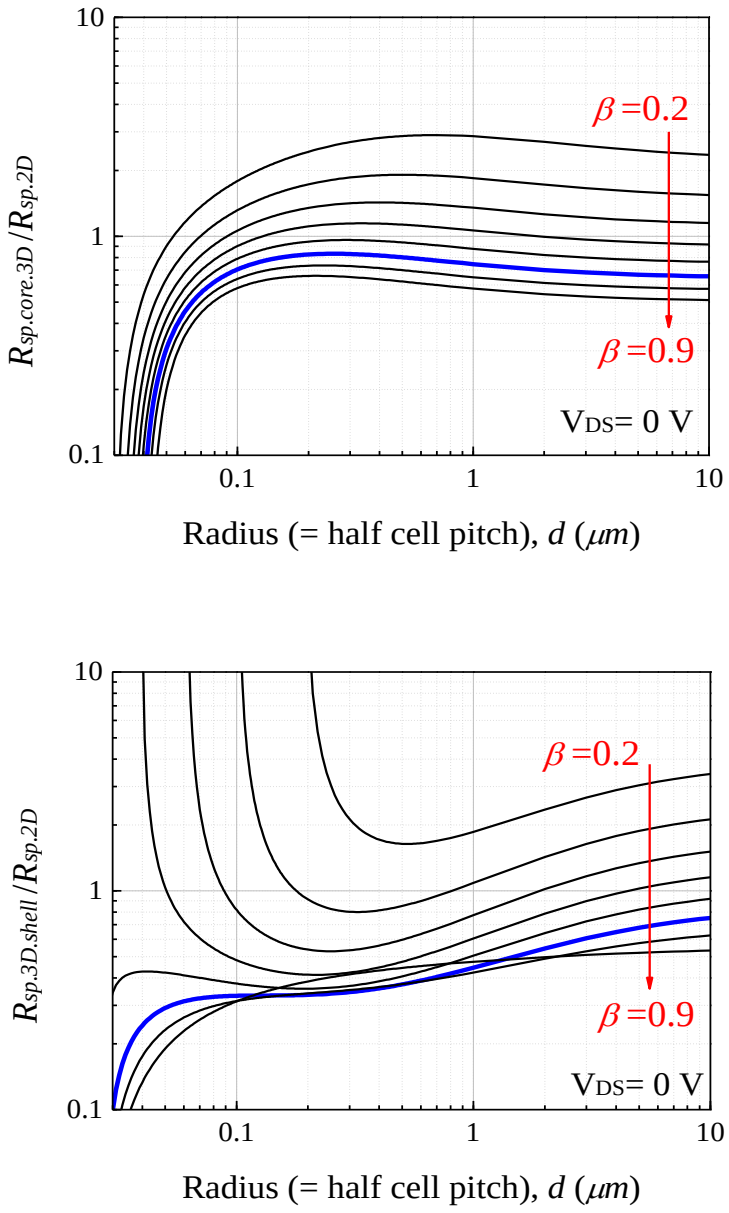

Figure 3.11 Ratio of 3-D superjunctions to the 2-D conventional superjunction. Blue line: β= 0.7.

The figure of merit for 3-D superjunction MOSFET can be established by using the same calculation sequence shown in section 2. The investigation was compared with 2D SJ and the

calculation was carried out for the 3D core (n-type) – shell (p-type) superjunction. The specific resistance is

$$R_{sp.core} = \frac{L}{q\mu_n N_D}\frac{1}{\beta^2}\left(\frac{\beta d}{\beta d - W_{Ds}}\right)^2 \tag{3.1.22}$$

The doping concentration around the minimum cell pitch, *d*, is very high as shown in figures 3.7 and 3.9. and, therefore, the built-in depletion width can be approximated in terms of the material's energy bandgap

$$W_{Ds} = \beta\sqrt{\frac{4\varepsilon_S}{3qN_D}\psi_{bi}} \approx \beta\sqrt{\frac{4\varepsilon_S}{3qN_D}\frac{E_g}{q}} \tag{3.3.5}$$

The doping concentration at a given cell pitch can be derived from equations (3.3.1) and (2.1.20)

$$N_{D.core} = \frac{\sqrt{2}\varepsilon_{Si}E_{C.Si}}{q\beta d} = 1.17\times10^{12}\cdot(\beta d)^{-8/7} \tag{3.3.6}$$

By inserting equations (3.3.5), (3.3.6) and the mobility given by equation (3.3.2) into (3.1.22), the condition of minimum R_{sp} can be calculated

$$\frac{\partial R_{sp}}{\partial d} = 0 \text{ , when } \frac{W_{Ds}}{\beta d} = \frac{3}{7} \tag{3.3.7}$$

By inserting equation (3.3.5) into (3.3.7), the minimum cell pitch of 3-D superjunction is

$$d_{op} = \frac{98\sqrt{2}E_g\beta}{27qE_C} \tag{3.3.8}$$

Finally, by inserting equations (3.3.7) and (3.3.8) into (3.1.22) the minimum R_{sp} at the minimum cell pitch can be written as

$$R_{sp.3D} = 16\frac{E_g V_B}{q\mu_n \varepsilon_S E_C{}^3} \tag{3.3.9}$$

By applying Hudgin's relationship [51], $E_C \propto E_g{}^2$, into equation (3.3.9), the figure of merit for 3-D superjunction can be established as

$$FOM_{3D} = \left(\frac{V_B}{R_{sp.3D}}\right) = \mu_n \varepsilon_S E_C{}^{2.5} \text{ or } \mu_n \varepsilon_S E_g{}^5 \tag{3.3.9}$$

Table 3.1 summarises static figure of merits which have reported up to date.

Table 3.1 Expression of specific resistance and the static figure of merits of power MOSFETs

	Baliga	***Fujihira*** (2D)	***Kang and Udrea*** (2D)	***Kang and Udrea*** (3D)
	standard	Superjunction		
Specific Resistance as a function of cellpitch	N/A	$\frac{4V_B}{\mu_n \varepsilon_S E_C^2} d$	$\frac{2V_B}{\mu_n \varepsilon_S E_C{}^2} d\left(\frac{\beta d}{\beta d - W_{Ds}}\right)$	$\frac{V_B}{\mu_n \varepsilon_S E_C{}^2} \frac{d}{\beta}\left(\frac{\beta d}{\beta d - W_{Ds}}\right)^2$
Minimum Specific Resistance	$\frac{4V_B{}^2}{\mu_n \varepsilon_S E_C^3}$	N/A	$20\frac{E_g V_B}{q\mu_n \varepsilon_S E_C{}^3}$	$16\frac{E_g V_B}{q\mu_n \varepsilon_S E_C{}^3}$
FOM	$\mu_n \cdot \varepsilon_S \cdot E_C^3$	$\mu_n \cdot \varepsilon_S \cdot E_C^2$	$\mu_n \cdot \varepsilon_S \cdot E_C^{2.5}$	$\mu_n \cdot \varepsilon_S \cdot E_C^{2.5}$

Table 3.2 summarises the minimum specific resistance at a given β with respect to breakdown voltage. The specific resistance is measured at each minimum cell pitch as shown in figure 3.9.

Table 3.2 Specific resistance with respect to breakdown voltage for Silicon 3-D superjunction

	Core (n-type) – shell (p-type)	Core (p-type) – shell (n-type)
β= 0.2	$R_{sp} = 0.82\times10^{-4}\cdot V_B$	$R_{sp} = 20.1\times10^{-4}\cdot V_B$
β= 0.3	$R_{sp} = 1.14\times10^{-4}\cdot V_B$	$R_{sp} = 7.39\times10^{-4}\cdot V_B$
β= 0.4	$R_{sp} = 1.39\times10^{-4}\cdot V_B$	$R_{sp} = 4.00\times10^{-4}\cdot V_B$
β= 0.5	$R_{sp} = 1.56\times10^{-4}\cdot V_B$	$R_{sp} = 2.65\times10^{-4}\cdot V_B$
β= 0.6	$R_{sp} = 1.67\times10^{-4}\cdot V_B$	$R_{sp} = 1.93\times10^{-4}\cdot V_B$
β= 0.7	$R_{sp} = 1.71\times10^{-4}\cdot V_B$	$R_{sp} = 1.33\times10^{-4}\cdot V_B$
β= 0.8	$R_{sp} = 1.69\times10^{-4}\cdot V_B$	$R_{sp} = 0.69\times10^{-4}\cdot V_B$
β= 0.9	$R_{sp} = 1.65\times10^{-4}\cdot V_B$	$R_{sp} = 0.18\times10^{-4}\cdot V_B$

4. 2-D Dynamic Superjunction MOSFET

Summary

From previous sections, the static model for 2-D and 3-D superjunction MOSFETs are established. Specifically, a newly developed JFET model was able to predict the theoretical limit of the specific resistance and the cell pitch at a given breakdown voltage. The static characteristics, especially the low specific resistance, will contribute to the low conduction loss during the on-state operation. However, since power MOSFETs are switching devices, the switching losses need to be considered. The switching loss of power MOSFETs is originated from its parasitic capacitance and Joule heating. Superjunction's depletion behaviour during the turn-off transition is very non-linear and hard to model. This section will cover background knowledge of power losses in power MOSFETs with recent references. After investigating the depletion phenomenon in a superjunction system, inner circuit models will be provided and the capacitance model with respect to the applied drain voltage will be established. Finally, from the model, new dynamic figure of merits for superjunction MOSFET will be defined in terms of the material parameters.

4.1. Background and Issue

Owing to the fast switching speed featured by the unipolar conduction, Power MOFETs have been widely applied to both hard and soft switching (especially zero voltage switching) applications [58]. There must be several power loss factors by the power MOSFETs as shown in figure 4.1.

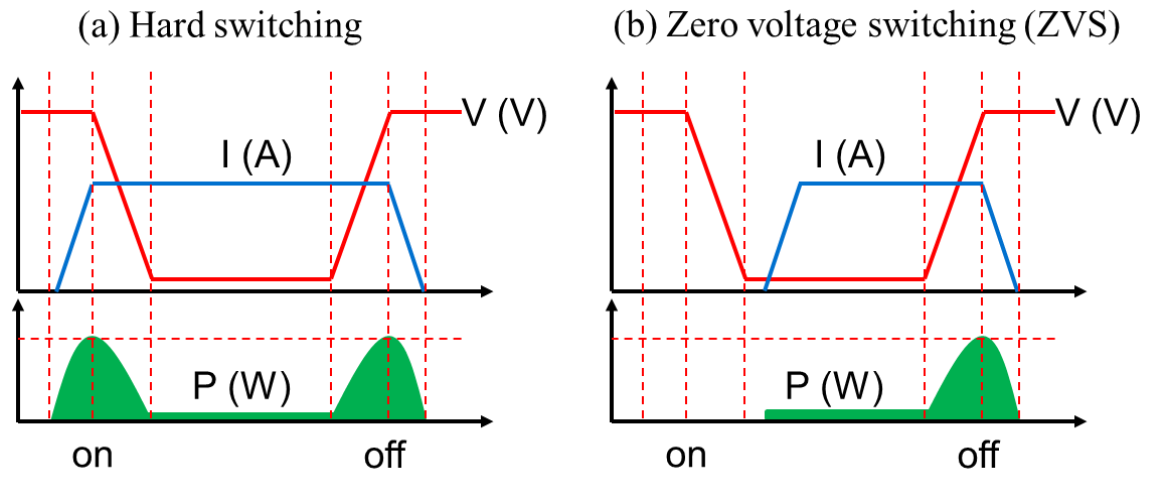

Figure 4.1 Schematic illustrations of (a) hard switching (b) soft (zero voltage) switching) of a power MOSFET.

To turn on or turn off the device, the parasitic input capacitance, C_{iss}, and the output capacitance, C_{oss}, must be charged or discharged during the switching transition,

$$C_{iss} = C_{GS} + C_{GD}, \tag{4.1.1}$$

$$C_{oss} = C_{GD} + C_{DS} \tag{4.1.2}$$

Where C_{GS}, C_{GD}, and C_{DS} are gate-to-source, gate-to-drain and drain-to-source capacitances, respectively, Figure 4.2 shows a schematic illustration of parasitic capacitance components in a superjunction MOSFET. As shown in figure 4.3, during the turn-on process, the C_{GS} and C_{GD} should be charged by the applied gate bias and the required charges are, Q_{GS} and Q_{GD}. The turn-off process is the inverse of turn-on (t_4 -> t_0).

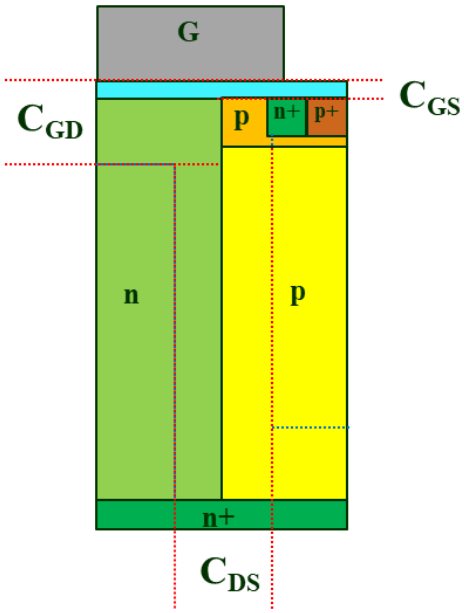

Figure 4.2 A schematic illustration of parasitic capacitances in a superjunction MOSFET.

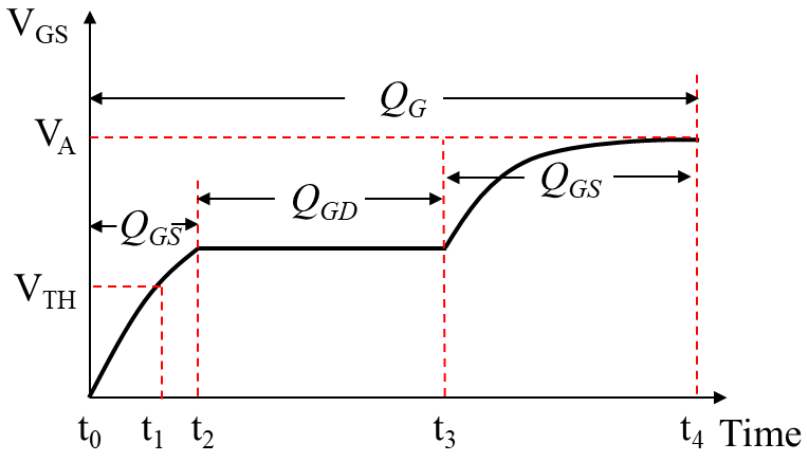

Figure 4.3 A schematic illustration of turn-on process of a power MOSFET.

During the initial period of the turn-on (t_0~ t_2), since the source contact is grounded and the drain contact is sustained by a high voltage, due to the potential difference of the capacitances with the applied gate voltage, only C_{GS} is charged first until the MOSFET's channel can sustain enough drain current. Once the MOSFET channel turned on, the drain current (t_2) flows and the gate current only charges C_{GD} while the drain voltage decreases accordingly until t_3.

Therefore, during both hard and soft switching, both C_{GS} and C_{GD} participate in the charging and discharging process. It should be noted that the C_{DS} is charged and discharged during the period of $t_2 \sim t_3$ when the drain voltage decreases (increases) [59]. Specifically, the depletion width between the p-well (source contact) and the n-type drift is the C_{DS} and is determined by the applied drain voltage.

As introduced in section 1, the power loss of a power device consists of on-state conduction loss, DP_{ON}, off-state leakage, $(1\text{-}D)P_{OFF}$, gate driving loss, P_{GS}, and switching loss, P_{SW} [44].

$$P_T = DP_{ON} + (1-D)P_{OFF} + P_{GS} + P_{SW} . \tag{1.45}$$

However, there has not been an exact figure of merit for describing the total power loss because it requires understanding of both circuits and devices' behaviours in the circuits. Meanwhile, several dynamic figures of merits have been proposed by Baliga (*BHFFOM*), Kim (*NHFFOM*), and Huang (*HDFOM*):

$$BHFFOM = \frac{1}{R_{sp} \times C_{iss.sp}} \text{ [43]}, \tag{1.46}$$

$$NHFFOM = \frac{1}{R_{sp} \times C_{oss.sp}} \text{ [45]}, \tag{1.47}$$

$$HDFOM = \frac{1}{R_{sp} \times C_{rss.sp}} \text{ [46]}. \tag{1.48}$$

Even though the above figures of merit partially indicate either input switching loss or output switching loss including on-state conduction loss, these figures of merit have been widely accepted by industry. The specific resistance of a superjunction MOSFET has been well defined by Fujihira [8] and this study [18], [19], but the specific capacitance of a superjunction device has not been clearly expressed by material parameters yet [60]–[62].

4.2. Modelling of Dynamic Figure of Merit

Until now, there has not been an exact model for the capacitor components in a superjunction MOSFET because the depletion behaviour in the superjunction is highly non-linear [35], [36], [63]. Since the depletion process of a superjunction device during the blocking mode have been well known, by visualising the depletion region in a superjunction at a given bias, this section will develop the gate-to-drain capacitance model.

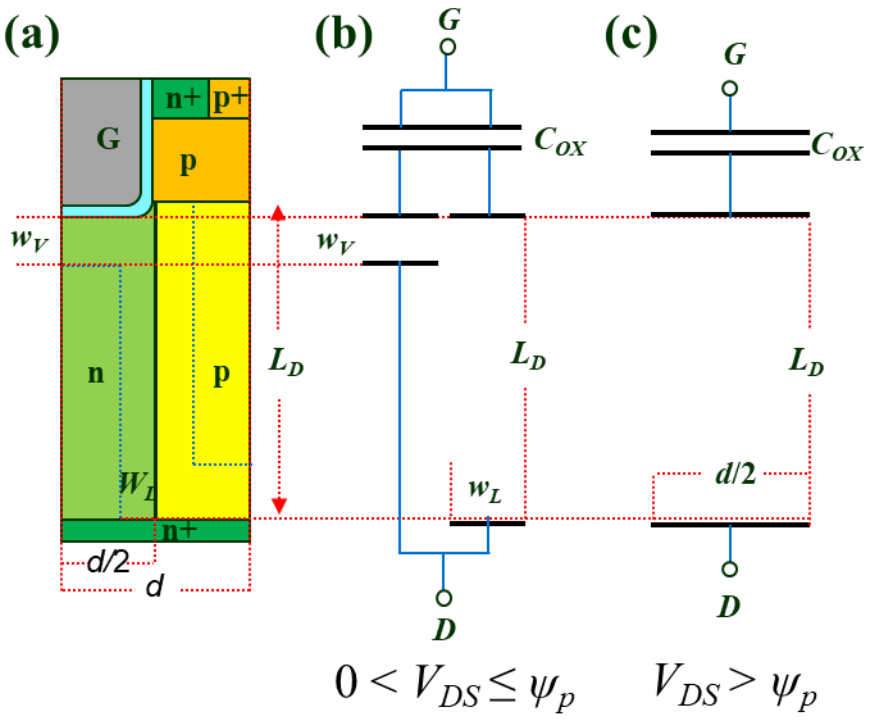

Figure 4.4 Schematic illustrations of gate-to-drain capacitance and the inner circuit model.

4.2.1. Gate-to-Drain Capacitance

The superjunction structure used in this chapter is balance with the same doping concentration and the width for both the n-pillar and the p-pillar. The gate-to-drain capacitance, C_{GD}, is the capacitance between the gate contact and the drain contact. C_{GD} includes both the gate oxide and the depletion region under the gate oxide as shown in figure 4.4. Where ψ_p is the pinch-off potential of the pillars which is the required voltage to fully deplete the pillars laterally,

$$\frac{d^2V}{dx^2} = -\frac{dE}{dx} = -\frac{qN_D}{\varepsilon_S} \tag{1.30}$$

From one-dimensional Poisson equation given by equation (1.30), the pinch-off potential can be obtained,

$$\psi_p = \frac{qN_D d^2}{4\varepsilon_S} \tag{4.2.1}$$

As shown in figure 4.4 (b), when the V_{DS} is lower than the pinch-off potential, the C_{GD} can be divided into two individual capacitances: one is the oxide-accumulation capacitance, $C_{ox\text{-}ac}$, and another is the oxide-pillar capacitance, $C_{ox\text{-}pi}$. Specifically, the components of $C_{ox\text{-}ac}$, the oxide capacitance and the accumulation capacitance, are connected in series and, the components of $C_{ox\text{-}pi}$, the oxide capacitance and the pillar capacitance, are connected in series. Therefore, each capacitance can be expressed as

$$C_{ox-ac} = \frac{\frac{\varepsilon_{ox}}{t_{ox}}\frac{\varepsilon_S}{w_V}\left(\frac{d}{2}-w_L\right)^2 Z^2}{\frac{\varepsilon_{ox}}{t_{ox}}\left(\frac{d}{2}-w_L\right)Z + \frac{\varepsilon_S}{w_V}\left(\frac{d}{2}-w_L\right)Z}, \tag{4.2.2}$$

$$C_{ox-pi} = \frac{\frac{\varepsilon_{ox}}{t_{ox}}\frac{\varepsilon_S}{L} w_L{}^2 Z^2}{\frac{\varepsilon_{ox}}{t_{ox}} w_L Z + \frac{\varepsilon_S}{L} w_L Z} \approx \frac{\varepsilon_S}{L} w_L Z \,, \tag{4.2.3}$$

$$C_{GD} = C_{ox-ac} + C_{ox-pi} \,, \left(0 < V_{DS} < \psi_p\right) \tag{4.2.4}$$

Where the depletion widths W_V and W_L are

$$w_V = \sqrt{\frac{2\varepsilon_S V_{DS}}{qN_D}} \,, \tag{4.2.5}$$

$$w_L = \sqrt{\frac{\varepsilon_S V_{DS}}{qN_D}} \tag{4.2.6}$$

Since the n-pillar region below the oxide is depleted in unidirectionally, the depletion width is multiplied by factor 2 as given by equation (4.2.5). When the pillars are fully depleted in the lateral direction (pinch-off potential), the C_{GD} capacitance can be simply presented as figure 4.4(c) and the capacitance can be written as

$$C_{GD} \approx \frac{\varepsilon_S}{L}\frac{dZ}{2} \,, \left(\psi_p < V_{DS}\right) \tag{4.2.7}$$

Figure 4.5 shows the analytic models given by equations (4.2.4), and (4.2.7) and the simulation data for both silicon and 4H-SiC. The analytic models show a good agreement with the simulation results.

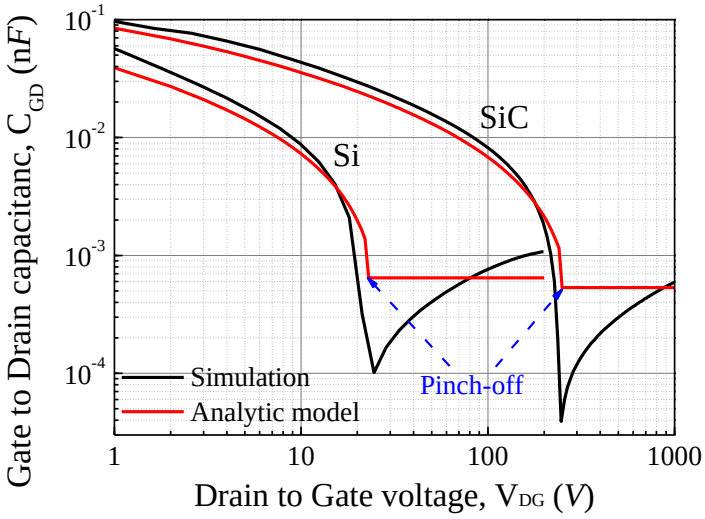

Figure 4.5 Analytic models of gate-to-drain capacitance (black lines) and the simulation data for both Si and SiC (red lines). The cellpitch, d= 5 μm, the depth of pillar Z= 1.0 μm, the length of the pillar, L= 40 μm, the number of cells=2×10^5, the doping concentration in the pillars= 2.31×10^{15} cm^{-3} for Si, and 2.09×10^{16} cm^{-3} for SiC.

The gate-to-drain capacitance rapidly decreases near the pinch-off potential where the depletion profile changes from figure 4.4 (b) to (c). The area under the C_{GD} is the required amounts of charges, $Q_{GD.sp}$ for charging the C_{GD},

$$Q_{GD.sp} = \left(\int_0^{\psi_p} C_{GD} dV_{DS} + \int_{\psi_p}^{V_{DS}} C_{GD} dV_{DS} \right) / dZ \tag{4.2.8}$$

$$Q_{GD.sp} \approx qN_D d \frac{\sqrt{2}}{8} \frac{d\varepsilon_{ox}}{t_{ox}\varepsilon_S} + \frac{\varepsilon_S}{2L} V_{DS} \tag{4.2.9}$$

Since most of the charge is consumed until V_{DS} reaches the pinch-off potential, (the area under the C_{GD} before pinch-off is very high compared to after pinch-off), ψ_p can be inserted into V_{DS} in equation (4.2.9),

$$Q_{GD.sp} = \left(\frac{\sqrt{2}}{2} \frac{\varepsilon_{ox}}{t_{ox}} + \frac{\varepsilon_S}{2L} \right) \psi_p \approx \left(\frac{\sqrt{2}}{2} \frac{\varepsilon_{ox}}{t_{ox}} \right) \frac{qN_D}{4\varepsilon_s} d^2 = \frac{\sqrt{2}}{8} \frac{\varepsilon_{ox}}{t_{ox}} \frac{qN_D}{\varepsilon_s} d^2 \tag{4.2.10}$$

4.2.2. Drain-to-Source Capacitance

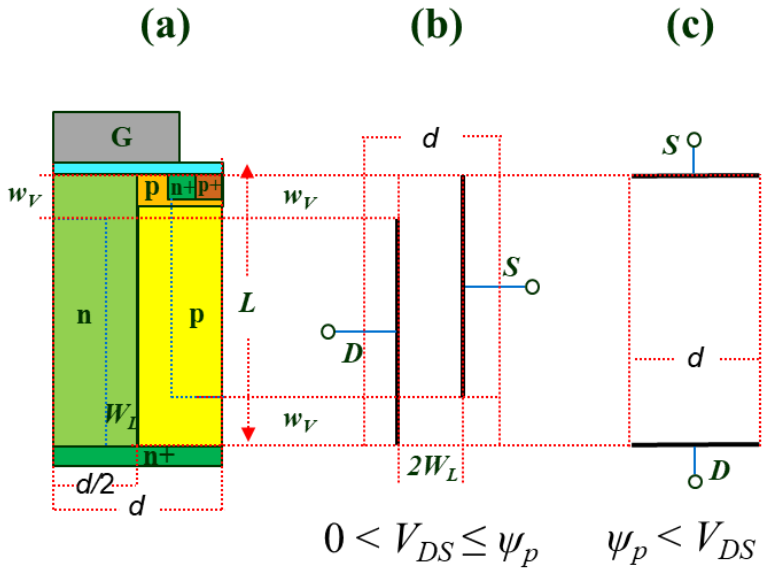

Figure 4.6 Schematic illustrations of drain-to-source capacitance and the inner circuit model.

The drain-to-source capacitance, C_{DS}, in a superjunction MOSFET is the depletion region between the drain and source contacts. Mostly, the drain-to-source capacitance is formed by the junction between the p-pillar and the n-pillar and, as the length of the pillar increases, the C_{DS} should be linearly proportional to the length as shown in figure 4.6. In a superjunction system, owing to the long enough pillar length, the total output capacitance, C_{oss} can be assumed to be C_{DS}. The C_{GD} is normally 100 ~ 1000 times lower than C_{DS}. From figure 4.6, the C_{DS} can be expressed as

$$C_{DS} = \frac{\varepsilon_S}{2w_L}\left(L - 2w_V\right)Z \ , \ \left(0 < V_{DS} < \psi_p\right), \tag{4.2.11}$$

$$C_{DS} = \frac{\varepsilon_S}{L} dZ \ , \ \left(\psi_p < V_{DS}\right) \tag{4.2.12}$$

Figure 4.7 shows the analytic model of C_{DS} and the simulation data for both Si and 4H-SiC. As mentioned in the previous section, the C_{DS} also experiences a rapid decrease in the values near the pinch-off potential due to the change of the depletion profile.

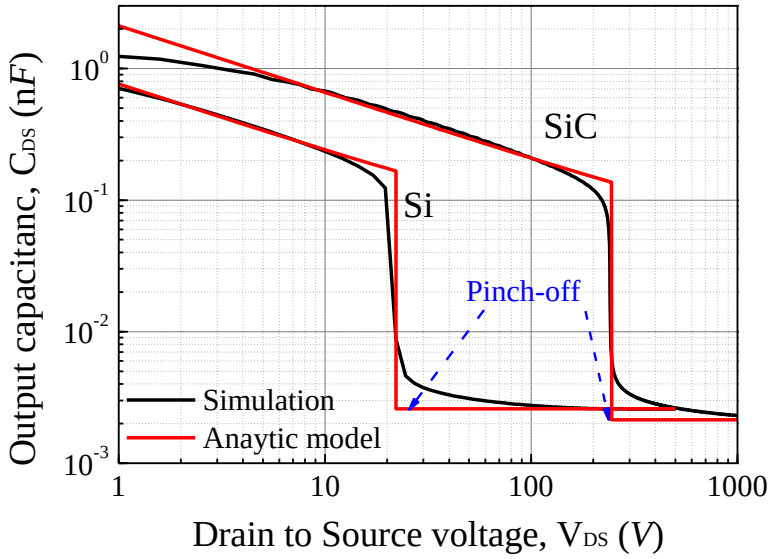

Figure 4.7 Analytic models of Drain-to-Source capacitance (black lines) and the simulation data for both Si and 4H-SiC (red lines). The cellpitch, d= 5 μm, the depth of pillar Z= 1.0 μm, the length of the pillar, L = 40 μm, the number of cells=2×10^{5}, the doping concentration in the pillars= 2.31×10^{15} cm^{-3} for Si, and 2.09×10^{16} cm^{-3} for SiC.

As mentioned above, the area under the capacitance curve is the required charge amount, and the integral can be written as

$$Q_{DS.sp} = \left(\int_0^{\psi_p} C_{Oss} dV_{DS} + \int_{\psi_p}^{V_{DS}} C_{Oss} dV_{DS} \right) / dZ \tag{4.2.13}$$

The integral given by equation (4.2.13) leads to

$$Q_{DS.sp} = \frac{\varepsilon_S}{L} V_{DS} - \frac{qN_D}{4L} d^2 + \frac{qN_D}{2} L \approx \frac{qN_D}{2} L \tag{4.2.14}$$

The first and the second terms given by equation (4.2.14) is relatively small compared to the third term and, therefore, $Q_{DS.sp}$ can be approximated as $qN_DL/2$. As mentioned above, since

the C_{DS} is, at least, one hundred times higher than C_{GD}, the output charge can be assumed to be $Q_{DS.sp}$

$$Q_{oss.sp} = Q_{GD.sp} + Q_{DS.sp} \approx Q_{DS.sp} = \frac{qN_D}{2} L \tag{4.2.15}$$

It should be noted that the analytic capacitance models for C_{GD} and C_{DS} given by chapters 4.2.1 and chapter 4.2.2 are valid for large cell pitches ($d > 1\ \mu m$). Below sub-micro cell pitches, owing to the relatively wider built-in depletion width on the pillars, the models become inaccurate.

4.2.3. Dynamic Figure of Merits

In this section, several dynamic figure of merits for a 2-D superjunction will be defined based on the equations established in the previous sections. The ideal specific resistance of a superjunction is

$$R_{sp} = \frac{2L}{qN_D\mu_n} \tag{2.1.5}$$

The $Q_{GD.sp}$ and $Q_{DS.sp}$ are

$$Q_{GD.sp} = \frac{\sqrt{2}}{8}\frac{\varepsilon_{ox}}{t_{ox}}\frac{qN_D}{\varepsilon_s}d^2, \tag{4.2.10}$$

$$Q_{oss.sp} \approx Q_{DS.sp} = \frac{qN_D}{2}L \tag{4.2.15}$$

The multiplications of equation (2.15) with (4.2.10) and (4.2.15) lead to

$$R_{sp}Q_{GD.sp} = \frac{\sqrt{2}}{4}\frac{\varepsilon_{ox}}{t_{ox}}\frac{L}{\varepsilon_s\mu_n}d^2, \tag{4.2.16}$$

$$R_{sp}Q_{oss.sp} \approx R_{sp}Q_{DS.sp} = \frac{L^2}{\mu_n} \tag{4.2.17}$$

From equation (2.1.4), the breakdown voltage and the electric field in a superjunction have the following relationship,

$$\sqrt{2}\frac{V_B}{E_C} = L \tag{4.2.18}$$

By inserting equation (4.2.18) into (4.2.16) and (4.2.17), the equations become

$$R_{sp}Q_{GD.sp} = \frac{1}{2}\frac{\varepsilon_{ox}}{t_{ox}}\frac{V_B}{\mu_n \varepsilon_S E_C} d^2, \tag{4.2.19}$$

$$R_{sp}Q_{oss.sp} \approx R_{sp}Q_{DS.sp} = 2\frac{V_B{}^2}{\mu_n E_C{}^2} \tag{4.2.20}$$

The $R_{sp}Q_{GD.sp}$ given by equation (4.2.19) consists of two components: the technology dependent figure of merit, $FOM(GD_Q)_T$,

$$FOM\left(GD_Q\right)_T = \frac{t_{ox}}{\varepsilon_{ox} d^2} \tag{4.2.21}$$

and the material dependent figure of merit, $FOM(GD_Q)_M$,

$$FOM\left(GD_Q\right)_M = \mu_n \varepsilon_S E_C \tag{4.2.22}$$

The technology dependent figure of merit can be improved by the cell pitch (scaling down) and the oxide thickness. In the case of $R_{sp}Q_{oss.sp}$ given by equation (4.2.20), the figure of merit should be compared to the Fujihira's figure of merit [64],

$$R_{SP}Q_{oss.sp.Fujihira} = \frac{81}{64}\frac{V_B{}^2}{\mu_n E_C{}^2} \tag{4.2.23}$$

Although the detailed modelling process is not described in Fujihira's report, the material figure of merit for both $R_{sp}.Q_{oss.sp}$ is the same,

$$FOM\left(DS_Q\right) = \mu_n E_C{}^2 \tag{4.2.24}$$

Equation (4.2.24) gives us a meaningful insight. i.e. as shown in figure 4.7, the pinch-off potential of the 4H-SiC superjunction is much higher than that of silicon owing to the 9 times higher doping concentration. Therefore, the decreased specific resistance in 4H-SiC

superjunction is cancelled by the increased capacitance charging loss as the R_{sp} and Q_{oss} are multiplied. Despite this, since the critical electric field of 4H-SiC is 9 times higher than Si, the figure of merit for 4H-SiC is highly advantageous compared to the silicon.

Even though equation (4.2.24) indirectly represents a trade-off between the on-state conduction loss (R_{sp}) and the turn-off switching loss ($Q_{oss.sp}$), more direct expression should be $R_{sp}E_{oss.sp}$ (more generally used in the industries). Also, in a soft switching circuit, generally zero voltage switching applications, only turn-off switching loss should be considered because the turn-on switching loss is ideally zero. For this reason, $R_{sp}E_{oss.sp}$ represents the device's performance. The turn-off switching energy loss, $E_{oss.sp}$ can be obtained by solving equation (4.2.25),

$$E_{oss.sp} \approx E_{DS.sp} = \left(\int_0^{\psi_p} C_{DS} V_{DS} \, dV_{DS} + \int_{\psi_p}^{V_{DS}} C_{DS} V_{DS} \, dV_{DS} \right) / \, dZ \tag{4.2.25}$$

As mentioned above, since the capacitance value of C_{DS} is significantly higher than C_{GD} in a superjunction MOSFET, C_{DS} can be assumed to be the only the factor for E_{OSS}. Developing equation (3.2.25) leads to

$$E_{oss.sp} \approx \frac{1}{2} \frac{q^2 {N_D}^2}{\varepsilon_S} d^3 + \frac{q^2 {N_D}^2}{24 \varepsilon_S} L d^2 \tag{4.2.26}$$

By multiplying the ideal R_{sp}, the $R_{sp}E_{oss.sp}$ becomes

$$R_{sp} E_{oss.sp} = \left(\frac{1}{2} \frac{q^2 {N_D}^2}{\varepsilon_S} d^3 + \frac{q^2 {N_D}^2}{24 \varepsilon_S} L d^2 \right) \frac{2L}{q N_D \mu_n} = \frac{q N_D}{\mu_n \varepsilon_S} d^2 \left(\frac{d}{L} + \frac{1}{12} \right) L^2 \tag{4.2.27}$$

By inserting equation (2.1.2) into (4.2.27), the equation leads to

$$\alpha E_C = \frac{q N_D}{2 \varepsilon_S} d \, , \left(0 < \alpha \le \frac{1}{\sqrt{2}} \right), \tag{2.1.2}$$

$$R_{sp}E_{oss.sp} = 2\alpha\left(\frac{d}{L}+\frac{1}{12}\right)\frac{E_C}{\mu_n}dL^2 \tag{4.2.28}$$

It should be noted that α should not exceed $1/\sqrt{2}$ the optimum condition. Inserting equation (4.2.18) into (4.2.17) leads to

$$R_{sp}E_{oss.sp} = 4\alpha\left(\frac{d}{L}+\frac{1}{12}\right)\frac{V_B{}^2}{\mu_n E_C}d \tag{4.2.29}$$

The coefficient of equation (4.2.29) can be varied by the selected cell pitch and the length of the pillar. However, the coefficient will be normally less than 1. By taking the material parameters, the figure of merit becomes

$$FOM(DS_E) = \mu_n E_C \tag{4.2.30}$$

Table 4.1 summarizes the figure of merits derived in this chapter.

Table 4.1 – Summary of dynamic figure of merits for power MOSFETs with different materials.

	μ_n	ε	E_C	***FOM(GD$_Q$)***	***FOM(DS$_Q$)***	***FOM(DS$_E$)***
Material	$\left(cm^2/V\cdot s\right)$		$\left(MV/cm\right)$	$\mu_n \cdot \varepsilon_S \cdot E_C$	$\mu_n E_C{}^2$	$\mu_n E_C$
Si	1350	11.8	0.3	1	1	1
4H-SiC	720	10	2	3	24	4
h-GaN	900	9	3.3	6	81	7
β-Ga_2O_3	300	10	8	5	159	6
AlN	1100	8.7	11.7	23	1239	33
Diamond	1900	5.5	5.6	12	490	26

5. Conclusions

In this dissertation, various static and dynamic models of superjunction MOSFETs were established. By employing the classical JFET theory into the superjunction system, the specific resistance models for 2-D and 3-D superjunction MOSFETs were derived. These models can predict the theoretical limit of specific resistance. The analytical results are in very good agreement with the simulation data. Following this, the static and dynamic figures of merit for superjunction MOSFETs were derived in terms of the material parameters.

1. By using the classical JFET theory, an analytical model for a conventional 2-D stripe pillar superjunction was developed. The p-pillar of the superjunction was considered as the p-type gate of the JFET and the n-pillar was regarded as the n-type channel of the JFET. Through the analytical calculations, the true limit of the on-state resistance for the superjunction MOSFET was found and a new figure of merit was established. The figure of merit for 2-D superjunction MOSFETs found in this study is placed between those derived by Baliga (which overestimates the inverse dependence of the on-state resistance with the electric field) and Fujihira (which underestimates the inverse dependence of the on-state resistance with the electric field)

2. From the way of implementing the classical JFET theory into superjunction systems, an analytical model for a compensated pillar superjunction was derived. The compensated pillar region between the p-pillar and the n-pillar was able to sustain a higher lateral electric field than that of conventional superjunctions. With the help of the increased lateral electric field, the doping concentration of the compensated pillar superjunction could be increased significantly which yielded an on-state resistance reduction in excess of 30 %.

3. An oxide pillar superjunction was introduced to reduce the on-state resistance of the superjunction MOSFETs. The oxide pillar was inserted between the p-pillar and the n-pillar. From Gauss law, the electric field sustained across the oxide is around 3 times higher than that at the interface within the semiconductor (Silicon). Therefore, a higher lateral electric field was able to be sustained in an oxide pillar superjunction than that in conventional superjunctions.

The higher electric field facilitates a higher pillar doping concentration. From the analytical model for an oxide superjunction, the specific resistance was decreased by more than 50 %.

4. The conventional 2-D superjunction system is based on a two-dimensional electric field (i.e. lateral and vertical). In this thesis we propose a 3-D superjunction system which is able to utilise the electric field from the third dimension. Based on the radial Poisson equation, the electric field distribution in 3D core-shell superjunction was derived. The lateral electric field is softer than that of 2-D and the maximum electric field, with the peak concentration being half of that in an optimised 2-D superjunction system. Therefore, the doping concentration in the pillar was doubled compared to that hat of 2-D and this yielded a reduction in the on-state resistance of 50%..

5. A dynamic figure of merit for 2-D superjunction MOSFETs was derived. There have been several dynamic figures of merit, but they have not been expressed in terms of material parameters. One of the main reasons is that the parasitic capacitances in superjunction MOSFETs are highly non-linear and hence difficult to model. From the capacitance dependence with the applied drain voltage, the consumed charge, and the energy were derived, and finally a dynamic figure of merit in terms of the material parameters was derived.

Future work

The purpose of this study was to establish the basic models for superjunctions in terms of material parameters. From the figures of merit introduced in this research, the trade-off between the on-state resistance and the breakdown voltage can be easily recognised. The fundamental purpose of improving the performance of superjunction devices is to increase the efficiency of the application circuits, when the switching devices are used in a power electronic system. Therefore, understanding the operational mechanisms of each topology in power electronics is very important. By extension, the influences of the power devices during the switching in each topology need to be investigated.

Until now, device engineers have been primarily focusing on the static characteristics of power devices. Also, circuit engineers have been investigating the circuitry operation with simplified device models. For this reason, there has always been a huge gap between the power devices and power circuits. One very important way to continue this research is to extend the models here and import them into device/circuit mixed mode simulation (i.e. the simulation tool that can run both device and circuit simulations in real time). From the investigation of the impact of the device performance in the circuits, device engineers need to study what design of devices is preferable for high efficiency and high robustness applications.

List of Publications

Journals

- H. Kang and F. Udrea, “On the Quasi-Saturation in State-of-the-Art Power MOSFETs,” IEEE Electron Device Letters, vol. 40, no. 5, pp. 754-756, May. 2019.

- H. Kang and F. Udrea, “Analytic Model of Specific ON-State Resistance for Superjunction MOSFETs With an Oxide Pillar,” IEEE Electron Device Letters, vol. 40, no. 5, pp. 761-764, Mar. 2019.

- H. Kang and F. Udrea, “On the specific on-state resistance of superjunction MOSFETs with a compensated pillar,” IEEE Electron Device Letters, vol. 39, no. 12, pp. 1901-1907, Dec. 2018.

- H. Kang and F. Udrea, “Material limit of power devices—Applied to asymmetric 2-D superjunction MOSFET,” IEEE Transactions on Electron Devices, vol. 68, no. 8, pp. 1-7, May. 2018.

- H. Kang and F. Udrea, “True material limit of power devices—Applied to 2-D superjunction MOSFET,” IEEE Transactions on Electron Devices, vol. 65, no. 4, pp. 1432-1439, Mar. 2018.

Conferences

- H. Kang and F. Udrea, “High Pillar Doping Concentration for SiC Superjunction IGBTs,” International Semiconductor Conference (CAS), pp. 151-154, Oct. 2018.

- H. Kang and F. Udrea, “Static and Dynamic Figures of Merits (FOM) for Superjunction MOSFETs,” International Symposium on Power Semiconductor Devices & ICs. Proceedings (ISPSD), May. 2019.

References

[1] S. Shirota and S. Kaneda, “New type of varactor diode consisting of multilayer p-n junctions,” *J. Appl. Phys.*, vol. 49, no. 12, pp. 6012–6019, Aug. 1978.

[2] S. Shirota and S. Kaneda, “New type of varactor diode consisting of multilayer *p* ? *n* junctions,” *J. Appl. Phys.*, vol. 49, no. 12, pp. 6012–6019, 1978.

[3] F. Udrea, G. Deboy and T. Fujihira, “Superjunction Power Devices, History, Development, and Future Prospects,” *IEEE Trans. Electron Devices*, vol. 64, no. 3, pp. 713–727, Jan. 2017.

[4] D. J. Coe, “High voltage semiconductor device,” European Patent, EP0053854, Jun-1982.

[5] D. J. Coe, “High voltage semiconductor device,” U.S. Patent 4 754 310, Aug-1988.

[6] J. A. Appels and H. M. J. Vaes, “High voltage thin layer devices (RESURF devices),” in *1979 International Electron Devices Meeting*, 1979, pp. 238–241.

[7] A. W. Ludikhuize, “A review of RESURF technology,” in *12th International Symposium on Power Semiconductor Devices & ICs. Proceedings (Cat. No.00CH37094)*, 2000, pp. 11–18.

[8] T. Fujihira, “Theory of semiconductor superjunction devices,” *Japanese J. Appl. Physics, Part 1 Regul. Pap. Short Notes Rev. Pap.*, vol. 36, no. 10, pp. 6254–6262, Oct. 1997.

[9] F. Udrea, A. Popescu and W. I. Milne, “3D RESURF double-gate MOSFET: A revolutionary power device concept,” *Electron. Lett.*, vol. 34, no. 8, p. 808, 1998.

[10] F. Udrea, A. Popescu and W. I. Milne, “The 3D RESURF junction,” *Semicond. Conf. Proceedings. Int.*, pp. 141–144, Mar. 1998.

[11] G. Deboy, N. Marz, J.-P. Stengl, H. Strack, J. Tihanyi and H. Weber, “A new generation of high voltage MOSFETs breaks the limit line of silicon,” *Int. Electron Devices Meet. 1998. Tech. Dig.*, pp. 683–685, Dec. 1998.

[12] A. G. M. Strollo and E. Napoli, “Power superjunction devices: An analytic model for breakdown voltage,” *Microelectronics J.*, vol. 32, no. 5–6, pp. 491–496, 2001.

[13] A. G. M. Strollo and E. Napoli, “Optimal ON-resistance versus breakdown voltage tradeoff in superjunction power devices: a novel analytical model,” *IEEE Transactions on Electron Devices*, vol. 48, no. 9. Ieee, pp. 2161–2167, Sep-2001.

[14] E. Napoli, H. Wang and F. Udrea, “The effect of charge imbalance on superjunction power devices: An exact analytical solution,” *IEEE Electron Device Lett.*, vol. 29, no. 3, pp. 249–251, Feb. 2008.

[15] H. Wang, E. Napoli and F. Udrea, “Breakdown voltage for superjunction power devices with charge imbalance: An analytical model valid for both punch through and non punch through devices,” *IEEE Trans. Electron Devices*, vol. 56, no. 12, pp. 3175–3183, Oct. 2009.

[16] W. Saito, “Comparison of Theoretical Limits between Superjunction and Field Plate Structures,” *Proc. Int. Symp. Power Semicond. Devices ICs*, pp. 241–244, May 2013.

[17] D. Disney and G. Dolny, “JFET depletion in superjunction devices,” *Proc. Int. Symp. Power Semicond. Devices ICs*, no. 2, pp. 157–160, May 2008.

[18] H. Kang and F. Udrea, “True Material Limit of Power Devices -Applied to 2-D Superjunction MOSFET,” *IEEE Trans. Electron Devices*, vol. 65, no. 4, pp. 1432–1439, Mar. 2018.

[19] H. Kang and F. Udrea, “Material Limit of Power Devices-Applied to Asymmetric 2-D Superjunction MOSFET,” *IEEE Trans. Electron Devices*, vol. 68, no. 8, pp. 1–7, May 2018.

[20] F. D. Bauer, “The super junction bipolar transistor: a new silicon power device concept for ultra low loss switching applications at medium to high voltages,” *Solid. State. Electron.*, vol. 48, no. 5, pp. 705–714, May 2004.

[21] M. Antoniou, F. Udrea and F. Bauer, “The 3.3kV semi-SuperJunction IGBT for increased cosmic ray induced breakdown immunity,” *Proc. Int. Symp. Power Semicond. Devices ICs*, pp. 168–171, Jun. 2009.

[22] M. Antoniou, F. Udrea, F. Bauer and I. Nistor, “The Semi-Superjunction IGBT,” vol. 31, no. 6, pp. 591–593, Apr. 2010.

[23] M. Antoniou, F. Udrea and F. Bauer, “The superjunction insulated gate bipolar transistor optimization and modeling,” *IEEE Trans. Electron Devices*, vol. 57, no. 3, pp. 594–600, Feb. 2010.

[24] F. Bauer, I. Nistor, A. Mihaila, M. Antoniou and F. Udrea, “Superjunction IGBT filling the gap between SJ MOSFET and ultrafast IGBT,” *IEEE Electron Device Lett.*, vol. 33, no. 9, pp. 1288–1290, Jul. 2012.

[25] E. Kho, C. Tee, M. Antoniou, F. Udrea, A. Hölke, S. J. Pilkington, D. K. Pal, N. L. Yew, W. Azlan, B. Wan and Z. Abidin, “200 V Superjunction N-Type Lateral Insulated-Gate Bipolar Transistor With Improved Latch-Up Characteristics,” *IEEE Trans. Electron Devices*, vol. 60, no. 4, pp. 1412–1415, 2013.

[26] K. H. Oh, J. Kim, H. Seo, J. Jung, E. Kim, S. S. Kim and C. Yun, “Experimental investigation of 650V superjunction IGBTs,” in *28th International Symposium on Power Semiconductor Devices and ICs (ISPSD)*, pp. 299–302, 2016.

[27] H. Kang and F. Udrea, “High Pillar Doping Concentration for SiC Superjunction IGBTs,” in *2018 International Semiconductor Conference (CAS)*, pp. 151–154, 2018.

[28] H. Kang, J. Lee, K. Lee and Y. Choi, “Trench angle: a key design factor for a deep trench superjunction MOSFET,” *Semicond. Sci. Technol.*, vol. 30, no. 12, p. 125008, Oct. 2015.

[29] J. Millan, P. Godignon, X. Perpina, A. Perez-Tomas and J. Rebollo, “A Survey of Wide Bandgap Power Semiconductor Devices,” *IEEE Trans. Power Electron.*, vol. 29, no. 5, pp. 2155–2163, 2014.

[30] X. She, A. Q. Huang, Ó. Lucía and B. Ozpineci, “Review of Silicon Carbide Power Devices and Their Applications,” *IEEE Trans. Ind. Electron.*, vol. 64, no. 10, pp. 8193–8205, Jan. 2017.

[31] X. Zhong, B. Wang and K. Sheng, “Design and experimental demonstration of 1.35 kV SiC super junction Schottky diode,” in *2016 28th International Symposium on Power Semiconductor Devices and ICs (ISPSD)*, 2016, pp. 231–234.

[32] T. Masuda, Y. Saito, T. Kumazawa, T. Hatayama and S. Harada, “0.63 mohmcm2 / 1170 V 4H-SiC Super Junction V-Groove Trench MOSFET,” in *2018 IEEE International Electron Devices Meeting (IEDM)*, 2018, pp. 8.1.1-8.1.4.

[33] S. Harada, Y. Kobayashi, S. Kyogoku, T. Morimoto, T. Tanaka, M. Takei and H. Okumura, “First Demonstration of Dynamic Characteristics for SiC Superjunction MOSFET Realized using Multi-epitaxial Growth Method,” in *2018 IEEE International Electron Devices Meeting (IEDM)*, 2018, pp. 8.2.1-8.2.4.

[34] Infineon Technologies, “CoolMOS^{TM} C7 : Mastering the Art of Quickness - Application note,” Apr. 2013.

[35] K. S. F.Stückler, S. Abdel-Rahman, “600 V CoolMOSTM C7 Design Guide - Application note, Infineon Technology,” 2015.

[36] G. Deboy, “Advanced silicon devices: Applications & Trends,” 2016.

[37] S. M. Sze and K. K. Ng, *Physics of Semiconductor Devices*. John Wiley & Sons, Inc., 2006.

[38] J. J. A. B. William H. Hayt, *Engineering Electromagnetics, 8th Ed.*, 8th ed. McGraw-Hill, 2012.

[39] S. M. Sze and G. Gibbons, “Avalanche breakdown voltages of abrupt and linearly graded p-n junctions in Ge, Si, GaAs, and Gap,” *Appl. Phys. Lett.*, vol. 8, no. 5, pp. 111–113, 1966.

[40] W. Fulop, “Calculation of avalanche breakdown voltages of silicon p-n junctions,” *Solid. State. Electron.*, vol. 10, no. 1, pp. 39–43, Jan. 1967.

[41] B. J. Baliga, *Fundamentals of Power Semiconductor Devices*. Springer Science, LLC, 233 Spring Street, New York, NY 10013, USA, 2010.

[42] B. J. Baliga, “Evolution of MOS-Bipolar Power Semiconductor Technology,” *Proc. IEEE*, vol. 76, no. 4, pp. 409–418, 1988.

[43] B. J. Baliga, “Power Semiconductor Device Figure of Merit for High-Frequency Applications,” *IEEE Electron Device Lett.*, vol. 10, no. 10, pp. 455–457, Oct. 1989.

[44] K. Shenai, “The Figure of Merit of a Semiconductor Power Electronics Switch,” *IEEE Trans. Electron Devices*, vol. 65, no. 10, pp. 4216–4224, Oct. 2018.

[45] I.-J. Kim, S. Matsumoto, T. Sakai and T. Yachi, “New power device figure of merit for high-frequency applications,” in *Proceedings of International Symposium on Power Semiconductor Devices and IC’s: ISPSD ’95*, 1995, pp. 309–314.

[46] A. Q. Huang and S. Member, “New Unipolar Switching Power Device Figures of Merit,” *IEEE Electron Device Lett.*, vol. 25, no. 5, pp. 298–301, Jun. 2004.

[47] A. A. E. Taylor, “L’Hospital’s Rule,” *Math. Assoc. Am.*, vol. 59, no. 1, pp. 20–24, 1952.

[48] A. W. Ludikhuize, “Kirk effect limitations in High Voltage IC ’s,” *Proc. 6th Internat. Symp. Power Semicond. Devices IC’s*, no. 94, pp. 3–6, Jun. 1994.

[49] H. P. D. Lanyon and R. A. Tuft, “Bandgap narrowing in heavily doped silicon,” in *1978 International Electron Devices Meeting*, 1978, pp. 316–319.

[50] H. P. D. Lanyon and R. A. Tuft, “Bandgap narrowing in moderately to heavily doped silicon,” *IEEE Trans. Electron Devices*, vol. 26, no. 7, pp. 1014–1018, Jul. 1979.

[51] J. L. Hudgins, S. Member, G. S. Simin, E. Santi, S. Member and M. A. Khan, “An Assessment of Wide Bandgap Semiconductors for Power Devices,” *IEEE Trans. Electron Devices*, vol. 18, no. 3, pp. 907–914, May 2003.

[52] W. Saito, “Theoretical limits of superjunction considering with charge imbalance margin,” *Proc. Int. Symp. Power Semicond. Devices ICs*, pp. 125–128, May 2015.

[53] H. Kang and F. Udrea, “On the Specific On-state Resistance of Superjunction MOSFETs with a Compensated Pillar,” *IEEE Electron Device Lett.*, vol. 39, no. 12, p. 1904, Dec. 2018.

[54] J. Evans and G. Amaratunga, “The behavior of very high current density power MOSFETs,” *Electron Devices, IEEE Trans.*, vol. 44, no. 7, pp. 1148–1153, Jul. 1997.

[55] H. Kang and F. Udrea, “On the Quasi-Saturation in State-of-the-Art Power MOSFETs,” *IEEE Electron Device Lett.*, vol. 40, no. 5, pp. 754–756, Feb. 2019.

[56] H. Kang and F. Udrea, “Analytic Model of Specific ON-State Resistance for Superjunction MOSFETs With an Oxide Pillar,” *IEEE Electron Device Lett.*, vol. 40, no. 5, pp. 761–764, Mar. 2019.

[57] E. Kreyszig, *Advanced Engineering Mathematics 10th Edition*, 10th ed. JOHN WILEY & SONS, INC., 2010.

[58] D. W. Hart, *Power Electronics*. Mc Graw-Hill, 2010.

[59] D. A. G. and J. Gowar, *Power MOSFET Theory and Applications*. New York: Wiley, 1989.

[60] Y. Ren, M. Xu, J. Zhou and F. C. Lee, “Analytical loss model of power MOSFET,” *IEEE Trans. Power Electron.*, vol. 21, no. 2, pp. 310–319, Mar. 2006.

[61] M. Rodríguez, A. Rodríguez, P. F. Miaja, D. G. Lamar and J. S. Zúniga, “An Insight into the Switching Process of Power MOSFETs: An Improved Analytical Losses Model,” *IEEE Trans. Power Electron.*, vol. 25, no. 6, pp. 1626–1640, Jan. 2010.

[62] I. Castro, J. Roig, R. Gelagaev, B. Vlachakis, F. Bauwens, D. G. Lamar and J. Driesen, “Analytical Switching Loss Model for Superjunction MOSFET With Capacitive Nonlinearities and Displacement Currents for DC–DC Power Converters,” *IEEE Trans. Power Electron.*, vol. 31, no. 3, pp. 2485–2495, May 2016.

[63] F. Stückler, S. Abdel-Rahman and K. Siu, “600 V CoolMOSTM C7 Design Guide (Tuning the limits of Silicon) - Application note,” 2015.

[64] T. Fujihira and Y. Miyasaka, “Simulated superior performances of semiconductor superjunction devices,” *Proc. 10th Int. Symp. Power Semicond. Devices ICs.*, no. V, pp. 423–426, Jul. 1998.